

**Politecnico
di Torino**

POLITECNICO DI TORINO

Master degree in
Nanotechnologies for ICTs

Master Degree Thesis

Current driven motion of magnetic domains and
skyrmions: a study on ultrathin CoFeB films

Supervisors

prof. Mariagrazia Graziano
prof. Marco Vacca

Candidate

Domenico Giuliano 265144

Anno Accademico 2021-2022

Contents

List of Tables	IV
List of Figures	V
1 Introduction	1
1.1 Beyond Moore's law	1
1.2 Ferromagnetism and Micromagnetism	1
1.2.1 Magnetic interactions	2
1.2.2 Magnetic domains	6
1.2.3 Micromagnetism	7
1.2.4 Field-driven magnetic dynamics	9
1.2.5 Current-driven magnetic dynamics	10
1.3 Novel magnetic materials	12
1.4 Current-driven motion applications: Racetrack Memory	13
2 Domain wall motion	17
2.1 Basic Principles	17
2.1.1 Classification of domain walls	18
2.1.2 Domain wall motion theory	20
2.2 Domain motion simulations	21
2.2.1 Ideal case	22
2.2.2 Temperature case	26
2.2.3 Material disorder	26
2.3 Domain wall motion in microwires	29
2.3.1 Microwire fabrication	29
2.3.2 Nucleation mechanisms	31
2.3.3 Improving nucleation efficiency	33
2.4 Artificial Nucleation Centers	33
2.4.1 Background irradiation	35
2.4.2 ANC irradiation	37
2.4.3 Irradiation on wire	39
2.5 Velocity	40
2.6 Barriers	44
2.6.1 Barrier Demonstration	45
2.6.2 Barrier simulations	48
2.6.3 Current-induced domain wall motion through barriers	51
2.6.4 Domain shifting	53
2.7 Conclusions and future prospects	55

3	Influence of Ga-ion irradiation on skyrmion size and dynamics	59
3.1	Basic Principles	59
3.1.1	Topology of magnetic textures	60
3.1.2	Dynamics of magnetic skyrmions	62
3.2	Tailoring the skyrmion size by FIB irradiation	64
3.2.1	Magnetic states in W/CoFeB/MgO/Ta	65
3.2.2	Skyrmion stack fabrication	68
3.2.3	Skyrmion dimension experiment	70
3.3	Skyrmion Velocity	72
3.3.1	Skyrmion velocity simulations	72
3.3.2	Skyrmion velocity experiment	75
3.4	Conclusions	78
4	Conclusions	81

List of Tables

2.1	Ta ₂ /CoFeB _{1.1} /MgO ₂ /Ta ₃ material parameters from [19].	22
2.2	Ta ₂ /CoFeB _{1.1} /MgO ₂ /Ta ₃ sputtering parameters.	30
2.3	Ga ⁺ ion doses used for the background irradiation study, whose results are shown in 2.19.	36
2.4	Ga ⁺ irradiation doses for the background irradiation and for the artificial nucleation center, respectively. The ANC irradiation dose is the sum of the background irradiation, done before, and the new irradiation to reach the desired value.	38
3.1	W ₃ /CoFeB _{1.1} /MgO ₂ /Ta ₄ sputtering parameters.	68

List of Figures

1.1	Schematic representation of the Dzyaloshinskii-Moriya interaction generated by the interaction between a large spin orbit coupling atom with two atomic spins, on the left, and the DMI generated at the interface of the ferromagnet with a high spin orbit coupling metal (heavy metal)[5].	5
1.2	Widefield-magneto optic Kerr effect images of the two magnetic thin-film stacks used in this work. The image on the left shows the Ta/CoFeB/MgO/Ta stack, which has larger average domain size; on the right the image of W/CoFeB/MgO/Ta stack, with smaller average domain size can be found.	6
1.3	Schematic representation of a ferromagnetic hysteresis.	7
1.4	Scheme of the spin transfer torque (on the left) and spin Hall effect (on the right) type of currents along a ferromagnetic track[7].	10
1.5	Spherical coordinate system (e_r, e_θ, e_φ) used to derivate the different torque terms. θ corresponds to the out-of-plane angle and φ to the in-plane angle[10].	11
1.6	Examples of Racetrack Memory proposed by Parkin, M. Hayashi, and L. Thomas [15]. The vertical-configuration (A) is the one that allows the highest storage density, taking advantage of the direction perpendicular to the silicon wafer. An example of the U-shaped racetracks is shown in (E). (B) shows the horizontal-configuration, which is the easiest one o be fabricated. In (C) and in (D) examples of, respectively, reading and writing are shown.	14
2.1	Representation in scale of the magnetic thin-film stack used for DW Motion. The CoFeB/MgO bilayer, which gives raise to PMA after thermal annealing, is sandwiched between two Ta thin-films, the latter used as seed/adhesion and as capping layer.	18

2.2	Type of domain walls. In the Bloch domain wall (a) the magnetization rotates around the line linking the two domain magnetic moments. The angle between each magnetic moment is constant. In Néel domain walls (b), the magnetization rotates along the line linking the two domain magnetic moments. The angle between the magnetic moments along the line is not constant [4].	19
2.3	Schematic representation of the torques generated by the presence of an applied magnetic field in case of a Néel domain wall.	20
2.4	Domain wall velocity profiles after depinning (a) and in the creep regime and depinning regimes (b)	21
2.5	Simulation image of a domain moving in a $2048 \times 1024 \mu\text{m}^2$ wire by means of a spin Hall effect current for low DMI strength ($D = 0.03 \text{ mJ/m}^{-2}$).	22
2.6	Domain velocity in the ideal case for $D = 0.03 \text{ mJ/m}^2$	23
2.7	Evolution of the domain longitudinal position and domain width in the ideal case, for $D = 0.03 \text{ mJ/m}^2$, for different current density steps of 50 ns. After each step the domain is reset to its initial configuration, in which it has a width of 300 nm, while the initial position is 150 nm. The value of the current density of each step is depicted by the red curve.	24
2.8	Domain position (a) and width (b) in the ideal case for low DMI strength (for $D = 0.03 \text{ mJ/m}^2$). The three current values correspond to the range before the first increase of the velocity, before the second one and in the saturated range.	25
2.9	Simulation image of a domain moving in a $2048 \times 1024 \mu\text{m}^2$ wire by means of a spin Hall effect current for high DMI strength ($D = 3 \text{ mJ/m}^{-2}$).	25
2.10	Domain velocity in the ideal case for different values of DMI coefficient.	26
2.11	Evolution of the domain longitudinal position and domain width in the ideal case, for $D = 3 \text{ mJ/m}^2$, for different current density steps of 50 ns. After each step the domain is reset to its initial configuration, in which it has a width of 300 nm, while the initial position is 150 nm. The value of the current density of each step is depicted by the red curve.	27
2.12	Domain velocity at a temperature of 300K for low and high DMI strengths.	28
2.13	Example of grain distribution with a K_u variation of 5% with respect to the value of the ideal case.	28
2.14	Domain Wall velocity in presence of grains with $D=0.1\text{mJ/m}^2$	29
2.15	Hysteresis loops of $\text{Ta}_2/\text{CoFeB}_{1.1}/\text{MgO}_2/\text{Ta}_3$ before and after thermal annealing.	30

2.16	Domain Nucleation on a $50 \times 5 \mu\text{m}^2$ wire. The gap between the contacts is $25 \mu\text{m}$, which is the region in which the current flows. The nucleation current pulse is of $J \approx 7.2 \times 10^{11} \text{ A m}^{-2}$ for 150 ns and with a field offset of 1.5 mT.	32
2.17	Domain nucleation scheme with a current pulse together with a field offset. Figures (A)-(C) show the formation of a domain starting from two defects. The nucleation is due to the superposition of current and field torques (A), then the domains expand due to the field offset (B), whose expansion stops when two domains are faced, leading to the creation of a domain with opposite magnetization with respect to the ones nucleated by current pulse(C). The field offset has to be chosen low enough to not overcome the repulsion force between the domain walls of the nucleated domain. Figures (D)-(F) show the same nucleation process, but starting from the nucleation, due to a current pulse, of one domain, whose expansion stops due to repulsion forces of the edges.	34
2.18	In (a) the measured values of M_S and K_{eff} for different ion doses are shown. K_u is derived considering $K_u = K_{\text{eff}} + \frac{1}{2}\mu_0 M_S$. In (b) it is shown the coercivity evolution with respect to the Ga^+ ion dose.	36
2.19	Background irradiation study. The Ta/CoFeB/MgO/Ta thin-film stack has been irradiated in different $19 \times 19 \mu\text{m}^2$ squares with increasing Ga^2 ion doses. In figure the some squares are reported, whose ion doses are listed in Table 2.3.	37
2.20	Widefield magneto-optic Kerr effect image of the ferromagnetic dots used for the ANC study.	37
2.21	Evolution of the switching field with respect to the Ga^+ irradiation dose. The ion dose values include the background irradiation.	38
2.22	WMOKE images before and after the nucleation of a domain. The two images are taken on different wires which are both $5 \mu\text{m}$ wide, but with a different contact distance. The nucleation process is for both equal. Before the nucleation (a), the offset switches only the ANC (white dot), which it has lower switching field; after the nucleation (b) the domain expands until it reaches the background irradiation region edges, meaning that this region is energetically a trap.	40
2.23	Setup used for domain velocity experiment. It consists of a ferromagnetic wire with dimensions of $50 \times 15 \mu\text{m}^2$. The gap between the contacts is $25 \mu\text{m}$, which is the region of the wire in which the current flows.	41
2.24	Example of domain motion images at different time stamps, in the microwire used for the domain velocity experiment. The images are taken after each current pulse of $J \approx 7 \times 10^{11} \text{ A m}^{-2}$	42

2.25	Evolution of the measured mean velocity with respect to the current density. The average is calculated over 100 pulses with a pulsewidth of 100 ns.	43
2.26	Evolution of the measured mean velocity with respect to the current density. The average is calculated over 150 pulses with a pulsewidth of 100 ns.	44
2.27	Schematic representation of domain nucleation and domain shifting from one memory cell to another one. The latter are regions confined by Ga ⁺ ion irradiated barriers.	45
2.28	Irradiation scheme in scale of a long stripe to tune the barrier strength. The nucleation of the domain wall occurs on the left-hand side of the stripe due to background and ANC irradiation. The ion dose, as well as the barrier strength, increases from left to right over the different barriers.	46
2.29	Widefield magneto-optic Kerr effect image of a portion of a 500x8 μm stripe. It is a frame of the measurement of the field-driven domain wall motion through the different barriers.	46
2.30	Measured magnetic fields at which a crossing of the different Ga ⁺ irradiated barriers is recorded.	47
2.31	Simulation image of a domain wall moving in a 2048x1024 μm ² wire by means of a spin Hall effect current for high DMI strength ($D = 1 \text{ mJ/m}^{-2}$). The dashed line divides the variation region, which is the region in which M_S and K_u are varied, and the pristine region, in which the material parameters are the ones listed in 2.1.	48
2.32	Phase diagram showing the K_u and M_S values for which the domain wall escapes from the variation region. K_u^{VR} and M_S^{VR} are the uniaxial anisotropy coefficient and the saturation magnetization in the variation region. The axes show the ratios between the variation region parameters and the ones in the pristine region, which are the ones listed in Table 2.1 with $D = 1 \text{ mJ/m}^2$. The yellow dots correspond to simulations in which the domain wall did not move; the green ones are related to the simulations in which the domain escaped from the variation region; simulations with the parameters of red dots showed a domain reaching the transition between the variation and the pristine regions, but it was not able to overcome it. The background color corresponds to values of K_{eff} calculated with the K_u^{VR} and M_S^{VR} parameters.	49
2.33	Variation of the energy and of K_{eff} for different values of K_u^{VR} and M_S^{VR} . The energy increases when K_u^{VR} decreases or M_S^{VR} increases, while K_{eff} shows the opposite trend.	50
2.34	Irradiation scheme (a) and WMOKE image (b) of a 5 μm wide wire used for measuring the domain wall motion through an irradiation barrier.	51

2.35	Probability curves of the domain wall crossing the irradiation barriers with different doses.	53
2.36	Experimental demonstration of the shifting of a domain between the one confinement region to another. It is a widefield magneto-optic Kerr effect differential image, which means that the white region represents the domain after the last current pulse, while the black region represents the position of the domain before the first current pulse. The latter corresponds to the initial configuration, showing that the domain is correctly shifted.	54
2.37	Schematic representation of the nucleation of a domain in a ferromagnetic wire with two bit cells. The latter are regions confined by two Ga ⁺ ion irradiated barriers. (A) shows the initial configuration, in which a domain is confined in a memory cell. In this configuration a current pulse, together with a magnetic field offset, nucleates a domain wall (B) in the left-hand side of the wire thanks to an artificial nucleation center. The domain wall is then moved towards the first barrier due to the magnetic field offset (C).	54
3.1	Magnetic stack used for skyrmion study. The CoFeB/MgO bilayer, which gives raise to PMA, is sandwiched between W and Ta thin-films, used as seed/adhesion and as capping layer, respectively.	60
3.2	Illustration of two types of magnetic skyrmions[7].	61
3.3	2D illustrations of magnetic skyrmions with different topological numbers [27].	62
3.4	Trajectory of a skyrmion driven by a vertical spin-polarized current in a nanotrack [7].	63
3.5	Evolution of the magnetization texture at $K_u=0.75$ MA/m for different uniaxial anisotropy values. In all the simulations, the simulation domain is 2048×1024 nm ²	65
3.6	K_u - M_S diagram for $D = 1.5$ mJ/m ² . In the background, the colormap shows the evolution of $K_{\text{eff}} = K_u - \frac{1}{2}\mu_0 M_S^2$. The colors of the points of the scatter plot indicates the type of magnetic textures at equilibrium, which are also shown in Figure 3.5.	66
3.7	Simulation results of the evolution of the skyrmion diameter for different M_S and K_u values.	67

3.8	Hysteresis loops as a function of the thermal annealing time, measured with the laser magneto-optic Kerr effect technique. The annealing temperature is kept at 275 °C in controlled N ₂ atmosphere in all the different steps. The image shows decreasing of the switching field after each thermal annealing. After the first step, which is the one to give raise to the PMA, the coercivity is around 3 mT, after 10 minutes it is around 1.5 mT, to then reaching the zero-remanence state, where the sample gets demagnetized at 0 mT. From the latter case, a slight increasing of magnetic field makes the skyrmions appearing. The evolution of the sample magnetic texture is shown in the widefield magneto-optic Kerr effect images.	69
3.9	Widefield magneto-optic Kerr effect images of the evolution of the magnetization in the W/CoFeB/MgO/Ta stack sample for different irradiation doses at zero magnetic field.	70
3.10	Widefield magneto-optic Kerr effect images of the evolution of the magnetization in the W/CoFeB/MgO/Ta stack sample for different irradiation doses at magnetic field a magnetic field of 0.64 mT.	70
3.11	Evolution of the measured skyrmion diameter with respect to the applied magnetic field at different Ga ⁺ ion doses (ID in short). For the ID=1.14 × 10 ¹² ions/cm ² case, two values of the estimated diameter are shown. They belong to different measurements and are reported for completeness.	71
3.12	Evolution of the measured skyrmion diameter respect to the Ga ⁺ ion doses at different applied magnetic field values.	71
3.13	Example of skyrmion motion at different time stamps of the simulation. The skyrmion is initialized in the center of the microwire and, after relaxation, a current flows. This image has been realized considering M _S = 0.404 MA/m, K _u = 0.18 MJ/m ³ , D = 1.5mJ/m ² and J=1.5 × 10 ¹⁰ A/2.	73
3.14	Evolution of the skyrmion velocity and skyrmion angle for different current density and Ms values. The simulations have been performed considering K _u = 0.18 MJ/m ³ , D = 1.5mJ/m ² α = 0.015 and θ _{SH} = 0.15.	74
3.15	Evolution of the skyrmion velocity and skyrmion angle for different current density and Ku values. The simulations have been performed considering M _S = 0.375 MA/m, D = 1.5mJ/m ² α = 0.015 and θ _{SH} = 0.15.	74

3.16	Dependence of the skyrmion velocity with respect to the current density, for different irradiation doses. The measurements have been performed by injecting 100 times a train of 4 current pulses with pulsewidth of 50 ns into the ferromagnetic wires. Between each train of current pulses, a widefield magneto-optic Kerr effect images are recorded. Analyzing the images, the displacement of the skyrmions is measured, from which the skyrmion velocity is derived.	76
3.17	Widefield magneto-optical Kerr effect image of a 35 μm wide wire during after skyrmion motion measurement. The white dashed line separates the pristine region from the irradiated one. The colored lines indicate detected skyrmion motion trajectories, which are used for the calculation of the depicted skyrmion angle θ_{Sk}	77

Summary

The improvement of applications concerning CMOS technology is becoming a difficult task, due to physical and technology constraints, such as quantum effects or miniaturization below few nanometers. In order to overcome the related increasing of the power dissipation and rising of the costs, beyond-CMOS technologies have been attracted the attention of recent researches. This thesis explores the basics of one promising beyond-CMOS technology: Racetrack Logic. It is a spintronic technology that can be used for efficient data storage, thanks to important properties like non-volatility and low-power operation, allowing at the same time logic-in-memory. The building block of Racetrack Memories is the motion of magnetic textures into a sub-micron ferromagnetic tracks, thanks to a current directly injected into the track. This work is a study of the current-driven motion of two magnetic textures that can be used to implement a Racetrack Memory: *domain walls* and *skyrmions*. The former ones are interfaces between two magnetic domains having opposite magnetizations, while skyrmions are stable particle-like spin configurations which are topologically protected.

In first place, the domain wall motion is analyzed. The first task to address is the nucleation of a domain into a ferromagnetic microwire, which should be characterized by low current densities and which should occur in a well-defined region of the sample. Once the domain is created, it can be moved by injecting a current into the microwire. The results of the study show how to have a control over the nucleation of a domain and its position, by exploiting Focus Ion Beam irradiation to create artificial nucleation centers. They are localized areas where the material parameters, such as the saturation magnetization and the uniaxial anisotropy constant, are degraded leading to a reduced switching field. The study continues by analyzing the evolution of the domain velocity with respect to the current density injected into the wire, supported by micromagnetic simulations, to understand its dependency from the material parameters. The study ends with a demonstration of a systematic confinement and shifting of a domain between barriers, which constitutes the building block of the Racetrack Memory, in which information are encoded into magnetic domains.

In second place, a study of the dimension and the motion of magnetic skyrmions,

with respect to irradiation dose, is presented. Skyrmion diameter is a fundamental parameter that depends on material parameters, such as exchange energy, magnetic anisotropy and Dzyaloshinskii–Moriya interaction. These parameters can be locally varied using the Focus Ion Beam irradiation technology. The study is complemented with micromagnetic simulations. The experiment work is then extended to the characterization of the current-induced skyrmion motion, under different FIB irradiation conditions. The study shows that both the skyrmion velocity and the skyrmion angle are influenced from the ion dose.

The magnetic structures used for this work are based on CoFeB/MgO thin film stacks. CoFeB, together with MgO oxide, exhibits perpendicular magnetic anisotropy (PMA) and low damping, making these thin-film stacks the most promising materials for spintronic applications. The two mentioned thin-films are sandwiched between a seed and a capping layer. For domain wall motion the tantalum (Ta) is used as seed and capping layer, while in the magnetic stack hosting skyrmions the seed layer is made of tungsten (W), due to its higher spin-orbit coupling, leading to a stronger Dzyaloshinskii-Moriya interaction, which stabilizes skyrmions in the ferromagnetic material. To vary the material parameters, the Focus Ion Beam technology has been used, in which Ga⁺ ions are accelerated by means of an electrostatic field in the direction of the ferromagnetic sample. Micromagnetic simulation results are derived from Mumax3, a GPU-accelerated micromagnetic simulation program.

Acknowledgements

This thesis is based on experimental research conducted at the Technical University of Munich, thanks to the support of the Central Electronics and Information Technology Laboratory - ZEIT^{lab}.

I would like to thank professor M. Graziano and professor M. Vacca for introducing me to this project.

I would like to acknowledge Prof.Dr.Ing. M. Becherer for the opportunity to develop this work at the Technical University of Munich and for the fruitful discussions.

I would like to thank my tutors V. Ahrens, for the valuable support on the experimental activities, and L. Gnoli, for the precious guidance and perseverance throughout the elaboration of the thesis.

In addition, I would like to thank F. Riente and G. Turvani for the management of the studies.

1 Introduction

1.1 Beyond Moore's law

According to Moore's law, during the last decades, steps towards high performance integrated circuits technology were based on the scaling of the CMOS technology. However, the miniaturization of such devices led to the increasing of the power dissipation due to quantum effects. This pushed recent studies towards the exploration of spintronics, in which the properties of the electron spin, rather than its electrical charge, are exploited to store and process information. The resulting technologies are characterized by non-volatility and low-power consumption, which can improve the paradigms of data storage and, in particular, it can set the basics of logic-in-memory, thanks to the possibility to exploit the interaction of injected currents or magnetic fields with the magnetic textures, such as domain walls or skyrmions.

A fundamental role is played by the magnetic material involved. Tailoring the material parameters used for the application means tailoring the magnetic properties, which affects strongly the way an external magnetic field or with an injected current interact with the magnetic texture [1][2].

1.2 Ferromagnetism and Micromagnetism

Ferromagnetic materials are a class of magnetic materials which are able to remain magnetized without the presence of an external magnetic field. In ferromagnetic materials the atomic spins interact with an external field and, differently from paramagnetic materials, they can also interact between each others. This latter interaction originates from quantum mechanical properties of spins. The result is a force that tends to make all the spins aligned, so-called *exchange interaction*. However, it is not the only one and below the different interactions are discussed[3].

1.2.1 Magnetic interactions

The macroscopic order of the atomic spins which compose the magnetization texture of a ferromagnet is given by a competition between different interactions acting at atomic level, that can be divided in local and non-local interactions. The former ones depend on the local value and orientation of the magnetization, while the latter ones are influenced by the magnetization of the whole sample [4]. The result of these interactions is the development of forces able to arrange atomic spins until a minimum energy configuration is achieved. The energies associated to the type of interactions involved are:

- **Exchange energy.** This interaction is the responsible for the alignment of the spins one respect to the other. As mentioned, it originates from a quantum effect related to the indistinguishability of the electrons. In classical description, and for two consecutive electron spins (\mathbf{S}_i and \mathbf{S}_j), it is given by the energy term

$$E_{\text{ex}}^{\text{pair}} = -2\mathcal{J}\mathbf{S}_i \cdot \mathbf{S}_j \quad (1.1)$$

where \mathcal{J} is called *exchange constant*, which measures the strength of the interaction. The equation is minimized for a completely magnetized crystalline sample, which means that the totality of the spins point in one direction, so they are all parallel one to each other. Considering the energy per unit volume, the exchange energy can be also written as:

$$\frac{E_{\text{ex}}}{V} = A(\nabla\mathbf{m})^2 = -A\mathbf{m} \cdot \Delta\mathbf{m}, \quad A = \frac{n\mathcal{J}S^2}{a} \quad (1.2)$$

The equation reflects the dependence of the exchange energy with respect to the uniformity of the magnetization: when the gradient of the magnetization is zero, which means that all atomic spins are aligned, the exchange energy is zero. In real cases this energy cannot be equal to zero because of the presence of the defects of the material or because of the competition with other interactions [4].

- **Magnetostatic energy.** Called also *stray field energy* or *dipolar energy*, the *magnetostatic energy* originates from the divergence of the magnetization at the surface of the ferromagnet [3][4]. This type of energy is stored into its own magnetic field, which is called *demagnetizing field* \mathbf{H}_D . The latter is non-local by definition, because it involves the magnetization of the whole sample. \mathbf{H}_D can be expressed by:

$$\nabla\mathbf{H}_D = -\nabla\mathbf{M} = -N_D\mathbf{M} \quad (1.3)$$

The N_D term is called *demagnetizing factor*, which accounts for the shape of the sample and the direction of the magnetization. It has to be mentioned that the last expression is valid only for ellipsoidal shapes or for shapes that are limiting cases of it, such as wires and thin-films. If non-ellipsoidal shapes are considered, then one has to consider that the demagnetizing field is not equal through the sample. The magnetostatic energy associated to this type of interaction can be written as:

$$E_{\text{ms}} = \frac{1}{2} \mu_0 \int_V \mathbf{H}_D^2 dV \quad (1.4)$$

The $\frac{1}{2}$ term ensures that the interaction between two points of the samples is taken once [4].

- **Anisotropy energy.** This type of interaction depends on the nature of the material, in particular how the atoms are arranged. Depending on the crystal, shape, stress or atomic segregation, the magnetic material has an axis over which the direction of the magnetization is favoured. The anisotropy energy depends on the orientation of the magnetization with respect to this axes, which is called *easy axes*. Mathematically it is described using direction cosines.

For some systems, especially for thin-films, one can make the approximation that the anisotropy depends only on the angle between the magnetization and a given axis. In this case the the anisotropy interaction can be defined as *uniaxial anisotropy*. The more general approach would be to consider different possible axis corresponding to the crystal axis, each with different contributions depending on the material. In this case the anisotropy interaction can be defined as *cubic anisotropy*. In this work the discussion is limited to the uniaxial anisotropy, since the materials used for this thesis are thin-films and the uniaxial approximation holds.

The uniaxial anisotropy energy per unit volume can be expressed in terms of powers of direction cosines as: [4]

$$\frac{E_A}{V} = K_{u1} \sin^2 \theta + K_{u2} \sin^4 \theta \dots \quad (1.5)$$

where θ is the angle between the magnetization and the easy axis, K_{u1} and K_{u2} are the *uniaxial anisotropy constants*, which give a measure of the anisotropy interaction. The direction of the magnetization is mainly established by the

magnitude and by the sign of K_{u1} :

$$\begin{cases} \text{large } |K_{u1}|, K_{u1} \geq 0 & \text{the material has an } \textit{easy axis} \\ \text{large } |K_{u1}|, K_{u1} \leq 0 & \text{the material has an } \textit{easy plane} \end{cases} \quad (1.6)$$

For completeness, it has to be mentioned also that other two phenomena can contribute to the anisotropy energy term, which are the *Magnetoelastic and Magnetostriction energy*. The first one is related to the stress that can be applied to the magnetic thin film, while the latter is limited to a class of material which can change its dimension when a magnetic field is applied. The description of the energies related to this two interactions is out of the scope of this work.

In case of thin-films, the surface properties become relevant. The surface itself is a break of the symmetry of the system. This gives raise to another anisotropy, called *surface* or *interface anisotropy*. Differently, from the uniaxial anisotropy it is defined per unit surface Σ as

$$\frac{E_s}{\Sigma} = K_S \sin^2 \theta \quad (1.7)$$

where K_S is called the *surface anisotropy constant*. In terms of energy per unit volume the equation written above becomes

$$\frac{E_s}{V} = \frac{1}{d} K_S \sin^2 \theta \quad (1.8)$$

where d is the thickness of the thin film.

It has to be considered that the all the mentioned anisotropy terms belong to a unique physical principle, which allows the definition of an easy axis, or eventually of an easy plane.

- **Zeeman energy.** When an external magnetic field is applied, another energy contribution must be added, called *Zeeman energy*, given by [4]:

$$\frac{E_{\text{ext}}}{V} = -\mu_0 \mathbf{M} \cdot \mathbf{H} \quad (1.9)$$

which related to the external magnetic field \mathbf{H} .

- **Total energy and effective anisotropy constant.** Considering all the mentioned interactions the total energy of the system can be expressed as:

$$E_{\text{tot}} = E_{\text{ex}} + E_A + E_{\text{ms}} + E_{\text{ext}} \quad (1.10)$$

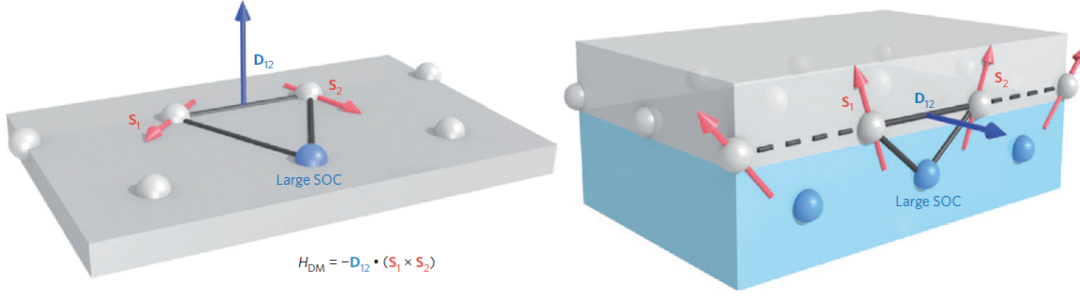


Figure 1.1: Schematic representation of the Dzyaloshinskii-Moriya interaction generated by the interaction between a large spin orbit coupling atom with two atomic spins, on the left, and the DMI generated at the interface of the ferromagnet with a high spin orbit coupling metal (heavy metal)[5].

All the energy contributions produce an effect on the alignment of the magnetic moments present in a ferromagnet material. The competition of the different interactions leads to the formation of an effective easy axis and consequently to the definition of an *effective anisotropy constant*. It can be expressed as [4]

$$K_{\text{eff}} = K_u - \frac{1}{2}\mu_0 M_S^2 + \frac{K_S}{d} \quad (1.11)$$

- **Dzyaloshinskii-Moriya interaction interaction.**

Another important interaction, that plays a fundamental role in defining the magnetic textures like skyrmions, is the *Dzyaloshinskii-Moriya interaction* (DMI in short). It is a chiral interaction that originates from a lack or from a breaking of inversion symmetry. This can happen in lattices (bulk DMI) or at the interface of magnetic thin-films. In the latter case the interfacial DMI originates from the interaction between two atomic spins and an atom with large spin-orbit coupling (SOC in short) [6][3][5]. The bulk DMI between two atomic spins can be expressed as:

$$H_{\text{DM}}^{\text{pair}} = \mathbf{D}_{12} \cdot (\mathbf{S}_1 \times \mathbf{S}_2) \quad (1.12)$$

and in terms of the reduced magnetization[7] as:

$$H_{\text{DM}} = D\mathbf{m}(\mathbf{r}) \cdot [\nabla \times \mathbf{m}(\mathbf{r})] \quad (1.13)$$

In case of interfacial DMI the last equation takes the form[7]

$$H_{\text{DM}} = D[m_z(\mathbf{r})\nabla \cdot \mathbf{m}(\mathbf{r}) - (\mathbf{m}(\mathbf{r}) \cdot \nabla)m_z(\mathbf{r})] \quad (1.14)$$

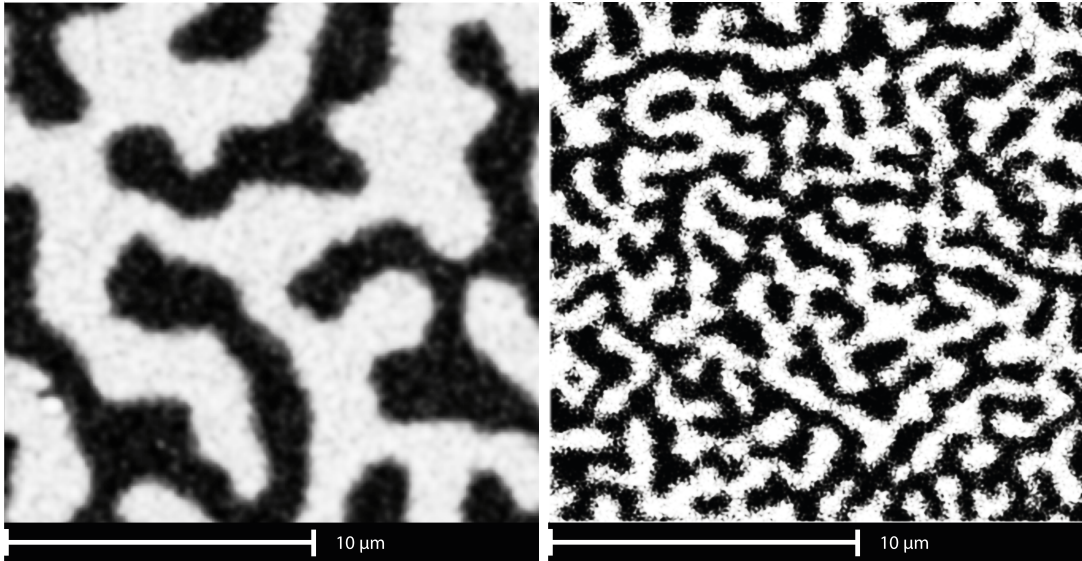


Figure 1.2: Widefield-magneto optic Kerr effect images of the two magnetic thin-film stacks used in this work. The image on the left shows the Ta/CoFeB/MgO/Ta stack, which has larger average domain size; on the right the image of W/CoFeB/MgO/Ta stack, with smaller average domain size can be found.

The parameter D is called *DMI constant* and it is proportional to \mathbf{D}_{12} , called *DM vector*. In Figure 1.1 a schematic representation of the interaction is shown. As can be seen, the DM vector results to be perpendicular to the plane containing the large SOC atom and the two considered atomic spins. One can notice that in case of interfacial DMI, the \mathbf{D}_{12} vector lies on the surface of the ferromagnetic material. In both cases, the effect of the DMI is to induce a tilting of the atomic spins leading to the stabilization of magnetic textures such as magnetic skyrmions [5][7]. It is a mechanism that competes with the exchange interaction and when the DMI constant becomes non-negligible it has to be included into the total energy expression depicted in 1.10.

1.2.2 Magnetic domains

The presence of domains was proposed by Weiss to explain the magnetization process of ferromagnets. They are regions in which the magnetization is uniform, which means that all the magnetic moments are pointing in the same direction. Domains pointing in opposite directions are separated by *domain walls*, which are region of transition of the direction of the magnetization. Discussion about the domain walls is postponed to Section 2.1. Examples of domains of two thin-film stacks used for this work are shown in Figure 1.2.

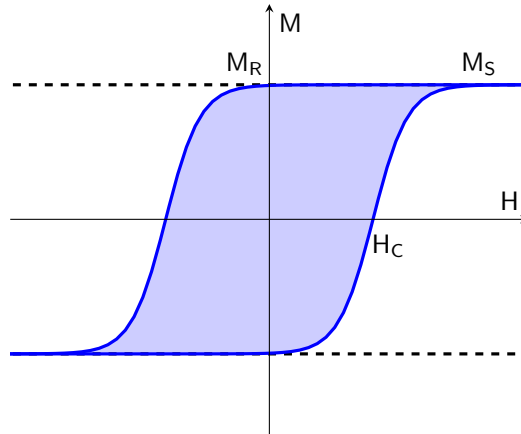


Figure 1.3: Schematic representation of a ferromagnetic hysteresis.

Without the presence of differently magnetized domains, the magnets should remain in the saturated state no matter the conditions over which the magnet is exposed. In real cases, the ferromagnetic materials can be found with zero average magnetization, meaning that the number of opposite magnetized domain is equal. Starting from this configuration, when a magnetic field is applied, the domains pointing in the same direction of the magnetic field expand at the expense of the domains pointing in the opposite direction. In this way, when the opposite magnetized domains disappear the ferromagnet remains in its saturated state, composed by all the magnetic moments pointing in the same direction. The typical behavior of the described magnetization process is shown in Figure 1.3, which is called *magnetic hysteresis*. M_S represents the *saturation magnetization* which corresponds to the maximum value that the magnetization can reach. M_R is called *remanence*, defined as the magnetization value that a ferromagnet retains in absence of an applied magnetic field. H_C is the minimum magnetic field needed to switch the magnetization and it is called *coercivity*.

1.2.3 Micromagnetism

One approach for studying the magnetism at the microscale is related to description of $\mathbf{M}(\mathbf{r})$, that is the magnetization of a volume portion of the sample which is larger than the interaction length between atomic spins and smaller than the sample [4]. Below the static and the dynamic properties of $\mathbf{M}(\mathbf{r})$ are described.

Taking into account the different energy contributions depicted in 1.10, the local magnetization can be derived from the minimization of the energy of the system

[4]. Defining the *reduced magnetization* $\mathbf{m} = \frac{\mathbf{M}}{M_S}$

$$E = \int_V A \{ [\nabla(\mathbf{m})]^2 + K_{u1} \sin^2(\theta) - \frac{\mu_0}{2} M_S \mathbf{m} \cdot \mathbf{H}_D(M) - \mu_0 M_S \mathbf{m} \cdot \mathbf{H} + e_{\text{DMI}} \} dV \quad (1.15)$$

where the DMI contribution has been included by means of the DMI energy per unit volume e_{DMI} . Dividing and multiplying all the terms by $\frac{2}{\mu_0 M_S^2}$, one obtains:

$$E = \frac{2}{\mu_0 M_S^2} \int_V \left\{ \frac{2A}{\mu_0 M_S^2} (\nabla \mathbf{m}^2 + \frac{2K_{u1}}{\mu_0 M_S^2} K_{u1} \sin^2(\theta) - \frac{1}{M_S} \mathbf{m} \cdot \mathbf{H}_D(M) - \frac{2}{M_S} \mathbf{m} \cdot \mathbf{H} + \frac{2}{\mu_0 M_S^2} e_{\text{DMI}} \right\} dV \quad (1.16)$$

From equation 1.16, important micromagnetic parameters can be derived:

- **Exchange length.** The exchange length l_{ex} is the characteristic length of the magnetic interactions involved into a ferromagnet.

$$l_{\text{ex}} = \sqrt{\frac{2A}{\mu_0 M_S^2}} \quad (1.17)$$

- **Quality parameter.** It is the ratio between the saturation magnetization and the anisotropy constant. The quality parameter gives a measure of how important is the anisotropy with respect to the stray field.

$$Q = \frac{2K_{u1}}{\mu_0 M_S^2} \quad (1.18)$$

- **Domain wall width.** The domain wall width is given by

$$\delta_0 = \pi \sqrt{\frac{A}{K_{u1}}} = \pi \Delta \quad (1.19)$$

Δ is called *domain wall width parameter* and it gives a measure the width of the domain wall. $\delta_0 = \pi \Delta$ is the *domain wall width*, which states that the larger the anisotropy, the smaller the domain wall width. Physically it can be explained by considering that higher is the anisotropy and higher will result the energy associated to the number of magnetic moments tilted with respect to the easy axis. It means that at equilibrium (low energy state) the number of tilted magnetic moments has to be as lower as possible.

- **Critical diameter.** The presence of the stray fields leads to the creation of a multi-domain state, rather than a single domain state. As mentioned before, the stray field depends on the physical dimension of the ferromagnet, which means that it exists a critical dimension under which the stray field becomes less relevant and the sample is more favored to stay in a single-domain state. That dimension is given by the *critical diameter*, which can be expressed as [4]:

$$D_{\text{cr}} = \frac{72\sqrt{AK_{\text{u1}}}}{\mu_0 M_S^2} \quad (1.20)$$

1.2.4 Field-driven magnetic dynamics

When an external magnetic field is applied, the magnetic texture of a ferromagnet is perturbed and the magnetic moments start to move accordingly to the mechanism presented below.

In presence of a magnetic field, the local magnetization is subjected to a torque given by

$$\frac{d\mathbf{M}}{dt} = -\gamma_G \mathbf{M} \times \mathbf{H} \quad (1.21)$$

The equation is true for isolated magnetic moments. When a collective system is considered, the single magnetic moments exchange energy with other subsystems. Mathematically, the interaction is described by a loss term, defined as *Gilbert constant* α_G . The equation, that now takes the name of *Gilbert equation*, becomes

$$\frac{d\mathbf{M}}{dt} = -\gamma_G \mathbf{M} \times \mathbf{H} + \frac{\alpha_G}{M_S} \mathbf{M} \times \frac{d\mathbf{M}}{dt} \quad (1.22)$$

Isolating $\frac{d\mathbf{M}}{dt}$ on one side, the equation reads

$$\frac{d\mathbf{M}}{dt} = -\gamma \mathbf{M} \times \mathbf{H}_{\text{eff}} + \frac{\alpha}{M_S} \mathbf{M} \times (\mathbf{M} \times \mathbf{H}_{\text{eff}}) \quad (1.23)$$

Equation 1.22 is called *Landau-Lishfitz-Gilbert equation* and describes the evolution of the local magnetization in presence of an applied magnetic field. The parameters α and γ are called, respectively, *damping constant* and *gyromagnetic ratio*, which expressions are [4]:

$$\begin{cases} \alpha = \frac{\alpha_G \gamma_G}{1 + \alpha_G^2} \\ \gamma = \frac{\gamma_G}{1 + \alpha_G^2} \end{cases} \quad (1.24)$$

1.2.5 Current-driven magnetic dynamics

A spin-polarized current can activate the motion of magnetic texture, such as domain walls and skyrmions, due to a exchange of torques between magnetic moments and current electron spins. Depending on the direction of the injection (see Figure 1.4), two types of current can be defined: the *spin transfer torque* (STT in short) current and the spin Hall effect current. In the first case the current is injected in the plane of the ferromagnet, while the in the latter case the current is injected vertically into the ferromagnet by means of the spin Hall effect, which cause the splitting of a current injected into a heavy metal (HM in short) depending on the spin of the electrons [7]. These two phenomena have been largely studied for the data transfer and data storage applications[8][9][7].

- **Spin Transfer Torque current.** The magnetic dynamics in presence of a STT current can be derived by extending the Landau-Lifshitz-Gilbert equation 1.22 with two other contributions[10]

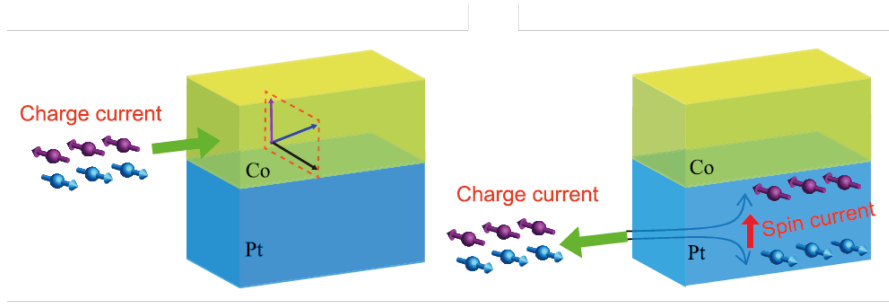


Figure 1.4: Scheme of the spin transfer torque (on the left) and spin Hall effect (on the right) type of currents along a ferromagnetic track[7].

$$\frac{d\mathbf{M}}{dt} = -\gamma\mathbf{M} \times \mathbf{H}_{eff} + \frac{\alpha}{M_S}\mathbf{M} \times \frac{d\mathbf{M}}{dt} - u\frac{\partial\mathbf{M}}{\partial y} + \frac{\beta u}{M_S}\mathbf{M} \times \frac{\partial\mathbf{M}}{\partial y} \quad (1.25)$$

where u and β are called *adiabatic* and *non-adiabatic spin transfer parameters*. β is a phenomenological parameter, while u can be derived as[10]

$$u = \frac{gJ_e\mu_B P}{2eM_S} \quad (1.26)$$

where g is the Landé factor, μ_B is the Bohr magneton, e the electron charge, P the polarisation factor of the current and J_e is the current density injected into the ferromagnet. The different terms of 1.25 exert a torque to the local magnetization. Considering a spherical coordinate system $(\mathbf{e}_r, \mathbf{e}_\theta, \mathbf{e}_\varphi)$ (see

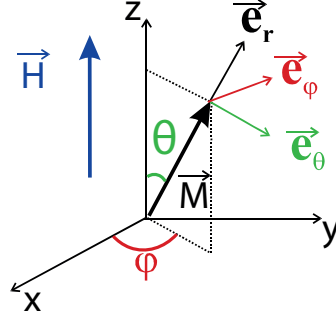


Figure 1.5: Spherical coordinate system ($\mathbf{e}_r, \mathbf{e}_\theta, \mathbf{e}_\varphi$) used to derive the different torque terms. θ corresponds to the out-of-plane angle and φ to the in-plane angle[10].

Figure 1.5), in which θ corresponds to the out-of-plane angle and φ to the in-plane angle, the torques associated to the fields acting on the domain wall are [10]

$$\begin{aligned}\Gamma_H &= \mathbf{M} \times \mathbf{H} && \text{External field} \\ \Gamma_{H_D} &= \mathbf{M} \times \mathbf{H}_D && \text{Demagnetizing field} \\ \Gamma_{H_\alpha} &= \mathbf{M} \times \mathbf{H}_D && \text{Equivalent damping field}\end{aligned}\quad (1.27)$$

The equivalent damping torque is given by $\frac{-\alpha}{\gamma M_S} \frac{d\mathbf{M}}{dt}$. The expressions of the mentioned torques are

$$\begin{aligned}\Gamma_H &= -M_S H \sin\theta \mathbf{e}_\varphi \\ \Gamma_{H_D} &= 4\pi M_S^2 (N_y - N_x) \sin\theta \sin\varphi \cos\varphi \mathbf{e}_\theta + 4\pi M_S^2 \sin\theta \cos\theta [N_z - \\ &\quad - N_y \sin^2\varphi - N_x \cos^2\varphi] \mathbf{e}_\varphi \\ \Gamma_{H_\alpha} &= \frac{\alpha M_S}{\gamma} \dot{\varphi} \sin\theta \mathbf{e}_\theta - \dot{\theta} \mathbf{e}_\varphi\end{aligned}\quad (1.28)$$

N_x, N_y, N_z are the demagnetizing factors which functions of the shape of the ferromagnet. The torques associated to the current interaction are[10]

$$\begin{aligned}\Gamma_u &= \frac{u}{\gamma} \frac{\partial \mathbf{M}}{\partial \theta} \frac{\partial \theta}{\partial y} = \frac{M_S u}{\gamma} \frac{\sin\theta}{\Delta} \mathbf{e}_\theta \\ \Gamma_\beta &= -\frac{\beta u}{\gamma M_S} \mathbf{M} \times \frac{\partial \mathbf{M}}{\partial \theta} \frac{\partial \theta}{\partial y} = -\beta \frac{M_S u}{\gamma} \frac{\sin\theta}{\Delta} \mathbf{e}_\varphi\end{aligned}\quad (1.29)$$

- **Spin Hall Effect current.** Spin Hall effects originates from quantum scattering events, such as spin skew scattering and side jump scattering, which are mechanisms able to change the velocity components of the electrons flowing into a metal. The scattering events are due to the *spin-orbit coupling* effect (SOC in short), which is larger for heavy-metal (HM) materials. For this

reason HM materials are used to induce vertical injections of spin currents, thanks to the spin Hall effect [11][12]. Since the origin of the phenomenon lies the SOC, the type of current is also referred as the *spin orbit torque* (SOT in short) current.

The dynamics of the local magnetization in case of a SOT current can be described by the LLG equation in which two more terms are added (as done for the STT current). In this case the equation takes the name of *Landau-Lifshitz-Gilbert-Slonczewski* equation, which reads

$$\frac{d\mathbf{M}}{dt} = -\gamma\mathbf{M} \times \mathbf{H}_{eff} + \frac{\alpha}{M_S}\mathbf{M} \times \frac{d\mathbf{M}}{dt} - M_S\mathbf{M} \times (a_j\mathbf{M} \times \mathbf{p}) + M_S b_j\mathbf{M} \times \mathbf{p} \quad (1.30)$$

where γ is the gyromagnetic ratio. \mathbf{p} is given by $\mathbf{p} = \text{sign}(\theta_{SH})\mathbf{J} \times \mathbf{n}$, which is a unit vector pointing in the direction of the magnetic moments that are injected into the ferromagnet. \mathbf{J} represents the direction of the current into the HM and \mathbf{n} the normal direction of the surface between the HM and the ferromagnetic layer. θ_{SH} is the *spin hall angle*, which is a material dependent parameter. The two coefficients a_j and b_j appearing into the third and the fourth terms of 1.30 are, respectively, the *damping-like torque* and *field-like torque* coefficients, which give the strengths of the equivalent fields associated to the two torques. The expression of the a_j coefficient is given by

$$\mu_0 a_j = \left| \frac{\hbar\theta_{SH}J}{2eMst} \right| \quad (1.31)$$

where \hbar is the reduced plank constant and t is the thickness of the ferromagnetic layer. The expression of b_j is instead more difficult to be found in literature, but it has been reported to be smaller than a_j [13][11][12].

1.3 Novel magnetic materials

In order to exploit the electron spin properties, a lot of effort has been put into the study of different magnetic materials. The improvement of the deposition techniques, especially for thin films, together with the development of characterization tools had led to important improvements in the material research field [14]. Some important physical phenomena have been discovered thanks to this progress, such as giant magnetoresistance, tunnel magnetoresistance, spin-transfer torque, spin-orbit torque, spin Hall effect, spin Seebeck effect, etc. From a technological point of view, an important property is the *perpendicular magnetic anisotropy* (PMA in short). Magnetic materials with PMA show an easy axis in the direction perpendicular to the surface. Historically, PMA has been observed in large

spin-orbit coupling materials, such as Co/Pt stacks. However these materials are characterized by large switching fields, meaning that higher fields, or higher energies in general, are needed to switch these magnets. It has been observed that also at interfaces of transition metal/oxide thin-films PMA can be found. This is due to the hybridization between the oxygen and the magnetic transition metal orbit across the interface [14]. This systems (e.g. CoFeB/MgO) have been demonstrated to have the potential to be implemented in magnetic storage devices, where an out-of-plane magnetization is needed. This applications, such as magnetic tunnel junctions for STT-MRAM cells, are shown to have a good memory retention, thanks to the large PMA amplitude, and a low writing current, thanks to a relatively weak damping [14].

Materials with PMA have also been studied for field and current-induced motion of magnetic textures, such as domain walls and skyrmions (see Chapter 2 and 3). Current-driven phenomena have been attracted a lot interest due to its potentiality to be integrated in electronic circuits.

1.4 Current-driven motion applications: Racetrack Memory

Up to now, memory devices exploit the magnetic recording as data storage method. It is the most reliable and economic technique and has been used to realize hard disk drives (HDD), characterized by large-capacity storage, but also by a slow writing/reading of the data. Magnetic random access memory (MRAM) has been proposed, characterized by nanosecond access time, non-volatility, reliability in severe environments and compatibility with current Si-based technology [16]. However, in the MRAM cell a capacitor is required for a reliable operation, limiting its speed potentiality. In 2008, Parkin, M. Hayashi, and L. Thomas proposed the Magnetic Domain-Wall Racetrack Memory as an alternative approach to store data, exploiting magnetic domains. The domains are arranged in tall columns of ferromagnetic material. The columns are then positioned perpendicularly to a silicon wafer, as shown in Figure 1.6.

The domains can shifted along the ferromagnetic wire thanks to injected electric current pulses. The current is able to move them thanks to the spin transfer torque effect. In this way the device becomes a shift register in which the bits are written or read at the intersection between the ferromagnetic wire and the silicon wafer, where a magneto tunnel junction device is placed to read the sign of the magnetization in the domain. The writing of the information in the wire can be done in several ways: by an external field generated by a current flowing into a metallic wire, placed near the ferromagnetic wire [15]; using a current directly

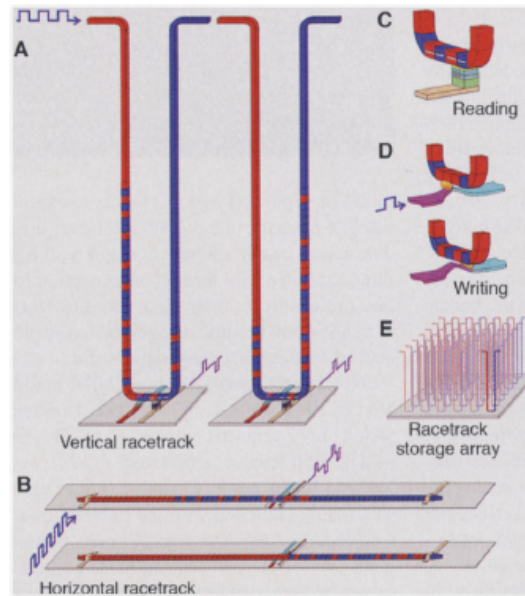


Figure 1.6: Examples of Racetrack Memory proposed by Parkin, M. Hayashi, and L. Thomas [15]. The vertical-configuration (A) is the one that allows the highest storage density, taking advantage of the direction perpendicular to the silicon wafer. An example of the U-shaped racetracks is shown in (E). (B) shows the horizontal-configuration, which is the easiest one to be fabricated. In (C) and in (D) examples of, respectively, reading and writing are shown.

injected into the racetrack, which will cause the local switching of the magnetization, due to spin-transfer torque; using stray fields generated from a domain of a secondary racetrack placed in proximity of the primary racetrack. The motion of the domain, once fixed the direction of the current, is independent on the magnetic charge of the DW. This is why only an injected current can be used to shift the domains: an external magnetic field would move the DWs depending on their magnetic charge. This can be translated in an expansion of the domains with magnetic charge concordant to the magnetic field sign and a compression of the discordant domains. If the field is too large, one can lose the information due to the complete switching of the racetrack, as it happens in a typical magnetization process of a demagnetized magnet.

In this work, the domain wall velocity on Ta/CoFeB/MgO/Ta thin film stack patterned with microns wide wires has been analyzed, with the goal of study the principles from the basis of the racetrack memory (see Chapter 2). The study is then completed with simulations.

Up to now, just the domain walls have been mentioned as main actors, but also skyrmions can be used to realize racetrack memories. Moreover, skyrmions

require less current to be moved, making them very attractive for this application. In Chapter 3 a study over the skyrmion dimension on W/CoFeB/MgO/Ta stack has been performed and a comparison between

2 Domain wall motion

Domain wall (DW in short) motion is a key concept at the base of data storage applications, such as Racetrack Memories, in which the magnetic domains, that encode information, shift from one cell to the other by means of an injected spin-polarized current. The scope of this chapter is to characterize the domain motion in a ferromagnetic microwire, describing the different technological steps for the realization of a racetrack memory cell. Firstly, the basic principles are discussed, providing fundamental tools to analyze the physical phenomena. The domain velocity is then simulated by means of micromagnetic simulations which can help to understand the effects of the interaction between a spin-polarized current and the domain motion, as a function of the DMI strength. The results are then compared with experimentally measured domain velocities on Ta₂/CoFeB_{1.1}/MgO₂/Ta₃ thin-film stack, where the numbers in subscript indicate the nominal thickness of the different layers. The mentioned ferromagnetic material is the one used by Riente et al. in their work[17]. The choice is justified by the fact that the ferromagnetic stack shows perpendicular magnetic anisotropy, as shown by Riente et al. in their work. Moreover, they measured the saturation magnetization M_S and the uniaxial anisotropy constant K_u of the sample, which is not an easy task. The measured material parameters, together with parameters found in literature, are shown in Table 2.1, which are used as inputs for DW velocity simulations. The second part of the chapter is then related to the attempt of creating a racetrack memory bit cell, which consists of a domain confined in barriers that can be overcome thanks to current pulses.

2.1 Basic Principles

Domain walls are transition regions between adjacent domains. In such regions the angle of the magnetic moments changes gradually between the direction of the correlated domains' magnetization. Within a domain the magnetic moments point approximately in the same direction and their alignment is favoured by the exchange and the anisotropy energy. However, such alignment causes an increase of the demagnetizing energy, due to the divergence of the self-magnetic field (so-called

demagnetizing field) generated by the magnetization. The demagnetizing field tries to slit the domains in order to close its field lines decreasing, the associated energy and favoring the creation of domain walls. Therefore, the creation of domain walls is due to the trade-off between the magnetostatic energy and the energy that gives raise when the magnetic moments are tilted, such as exchange and anisotropy energy[3][4].

2.1.1 Classification of domain walls

According to the evolution of the magnetic moments' direction, the domain walls can be classified in two classes[3]:

- **Bloch wall.** In Bloch domain walls, the magnetic moments rotate in a plane parallel to the domain wall plane (see Figure 2.2a).
- **Néel wall.** When the magnetic moments rotate perpendicularly to the plane of the domain wall, it is called Néel domain wall, which is shown in Figure 2.2b.

The magnetostatic energy determines the type of domain wall. In case of Bloch domain walls, the angle θ between the rotation plane and the plane containing the magnetizations of the two domains is constant and the domain wall energy per unit area does not depend on the demagnetizing field:

$$\gamma_{BW} = 4\sqrt{K_u A} \quad (2.1)$$

where K_u is the uniaxial anisotropy constant and A the exchange stiffness. In case of Néel domain walls, the angle θ is not constant, and this creates a

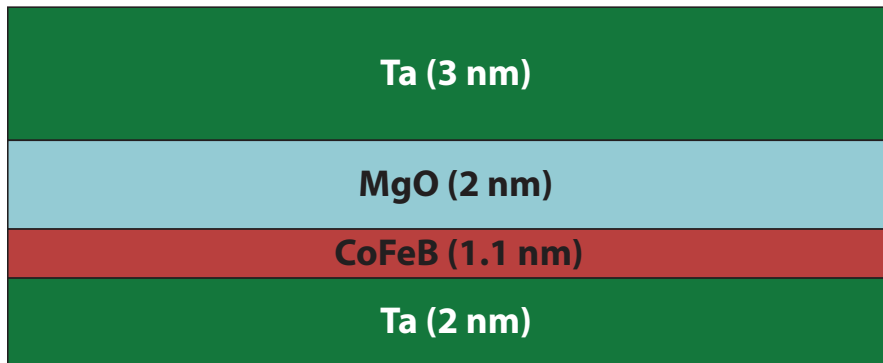


Figure 2.1: Representation in scale of the magnetic thin-film stack used for DW Motion. The CoFeB/MgO bilayer, which gives raise to PMA after thermal annealing, is sandwiched between two Ta thin-films, the latter used as seed/adhesion and as capping layer.

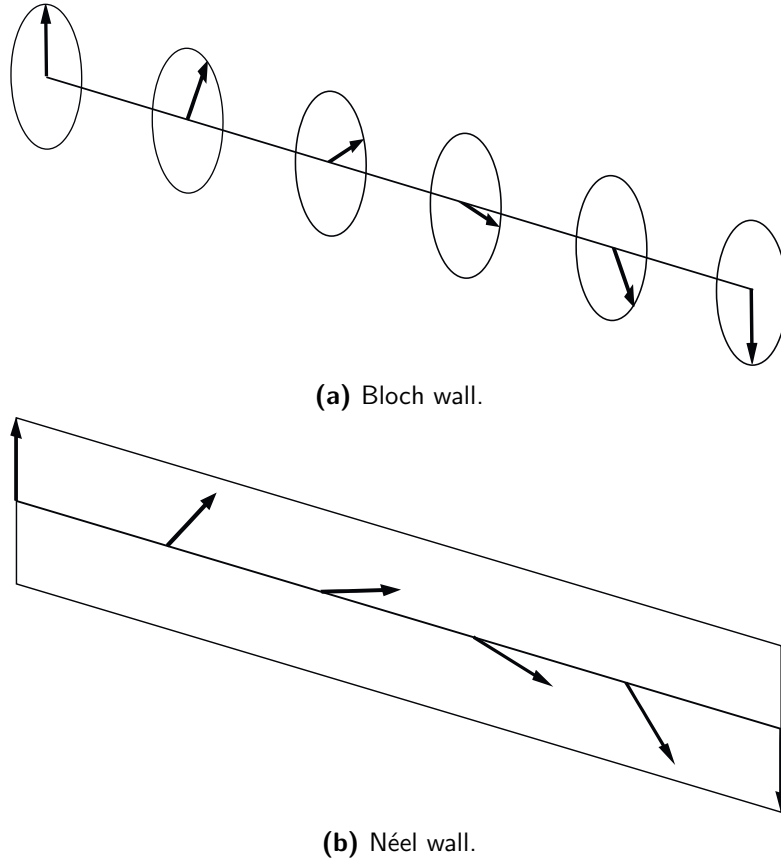


Figure 2.2: Type of domain walls. In the Bloch domain wall (a) the magnetization rotates around the line linking the two domain magnetic moments. The angle between each magnetic moment is constant. In Néel domain walls (b), the magnetization rotates along the line linking the two domain magnetic moments. The angle between the magnetic moments along the line is not constant [4].

dependency of the domain wall energy on the magnetostatic energy. The Néel domain wall energy per unit area results [4]:

$$\gamma_{NW} = 4\sqrt{A\left(K_u + \frac{1}{2}\mu_0 M_s^2\right)} \quad (2.2)$$

Therefore, Bloch domain walls are usually preferred in the bulk materials, since they are favored by the decreasing of the magnetostatic energy, while Néel walls are preferred in thin films because the rotation of magnetic moments out of the magnet plane costs magnetostatic energy[4][3].

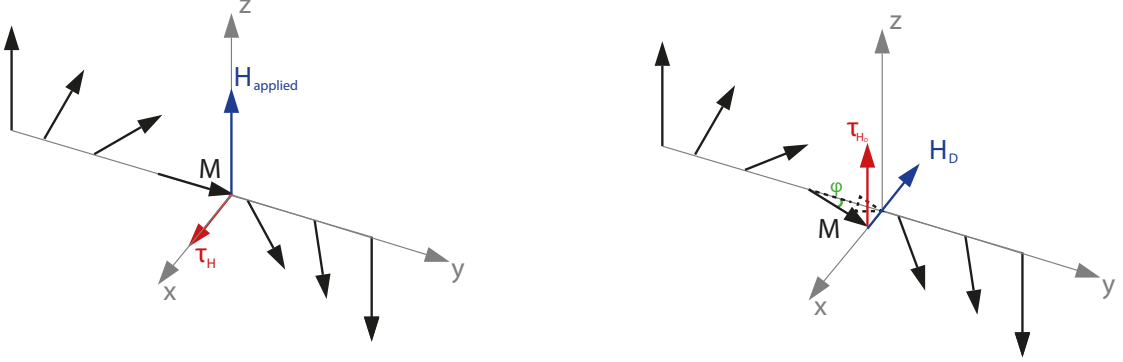


Figure 2.3: Schematic representation of the torques generated by the presence of an applied magnetic field in case of a Néel domain wall.

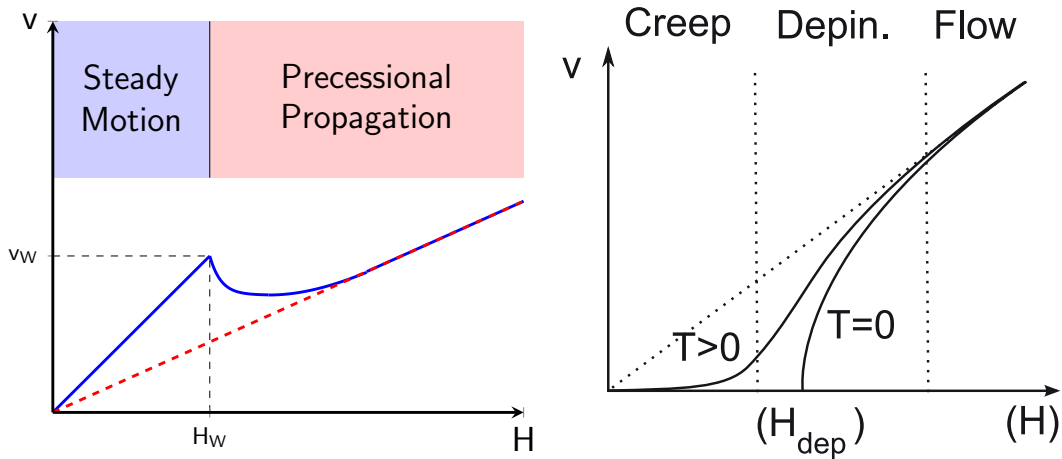
2.1.2 Domain wall motion theory

An external magnetic field exerted to a domain wall will cause its displacement. If the sample is in a multi-domain state, the field causes the expansion of domains whose magnetization points in the same direction of the applied magnetic field.

When a magnetic field is applied, the magnetic moments in the domain wall are canted due to the resulting field torque $\gamma \mathbf{M} \times \mathbf{H}_{\text{ext}}$ (see Figure 2.3). Defining φ as the angle between the magnetic moments and the plane containing the magnetization of the two domains (yz plane), the tilting of the magnetic moments, due to the field torque, generates a demagnetizing field proportional to the φ which imposes a torque $\gamma \mathbf{M} \times \mathbf{H}_{\text{D}}$, called demagnetizing torque, pointed in the same direction of the applied external field. The result is the motion of the domain wall in a way to expand the domains having the magnetization pointing in the same direction of the field[4][9]. An increase of the magnetic field results in an increasing of the demagnetizing torque, leading to faster domain wall motion. In this regime the domain wall velocity is linear to the applied field [10] (see Figure 2.4):

$$v_{\text{steady}} = \frac{\gamma \Delta}{\alpha} \left[H + (\beta - \alpha) \frac{u}{\gamma \Delta} \right] \quad (2.3)$$

When the magnetic field exceeds a threshold, the demagnetizing field is not able to follow the magnetic field anymore. This means that the demagnetizing torque cannot compensate the field torque, which will ignite the typical precessional motion of the magnetic moment in presence of a magnetic field. This transition is called *Walker breakdown* and it is reached when at $\varphi \approx \pi/4$ [4][9], corresponding to $H = H_{\text{W}}$, which is called *Walker breakdown field*, or simply *Walker field*. It has to be considered that the Walker breakdown can occur in presence of a field, but also in presence of a current. In the latter case, the phenomenon can occur at zero



(a) Domain wall velocity vs. applied field, showing the Walker breakdown. (b) Domain wall velocity behavior as a function of the applied field in a realistic system[18].

Figure 2.4: Domain wall velocity profiles after depinning (a) and in the creep regime and depinning regimes (b)

field when the current $J = J_W$, which is called *Walker current density*[10].

Walker breakdown has important implications on the performances of devices that exploit domain wall motion to transfer information: a change in the domain velocity implicates a variation in the design of such devices [4].

2.2 Domain motion simulations

After a brief discussion of the physical principles, the domain wall motion is simulated into a ferromagnetic microwire. The aim is to understand the behavior of the domain velocity with respect to a spin-polarized current. In particular, the simulations are divided in three parts: i) the ideal case in which the material is considered a perfect crystal and the temperature effects are not considered; ii) the temperature case, in which the effects of a non-zero temperature system are explored; iii) the grain case, in which the microwire used in the simulation is made by a granular pattern. In each grain, the material the uniaxial anisotropy constant is varied by 5 % with respect to the nominal value reported in Table 2.1. The aim of the last step is to understand the domain motion in presence of pinning centers, originated by material inhomogeneities. All the three cases are repeated for low and high DMI coefficients. The parameters used for the simulations are referred to the stack depicted in Figure 2.1 and are shown in Table 2.1.

M_s [$A\ m^{-1}$]	K_u [$J\ m^{-3}$]	A [$J\ m^{-1}$]	D [$J\ m^{-2}$]	α	θ_{SH}
8.308×10^5	5.5788×10^5	2×10^{-11}	$0.03 \div 3 \times 10^{-3}$	0.015	0.15

Table 2.1: $Ta_2/CoFeB_{1.1}/MgO_2/Ta_3$ material parameters from [19].

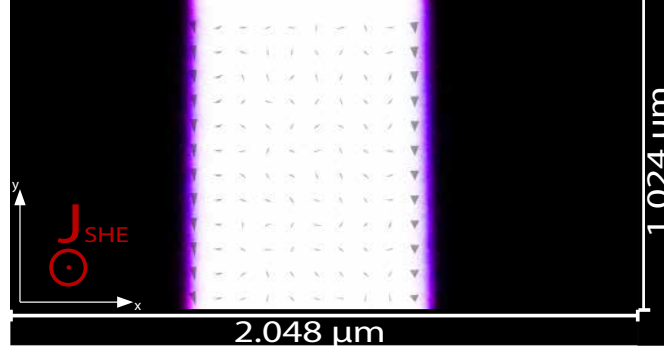


Figure 2.5: Simulation image of a domain moving in a $2048 \times 1024\ \mu\text{m}^2$ wire by means of a spin Hall effect current for low DMI strength ($D = 0.03\ \text{mJ}/\text{m}^2$).

2.2.1 Ideal case

The first case study is related to a ferromagnetic wire without thermal or material disorder effects. The sample under test is a microwire, which dimensions are $2048 \times 1024\ \text{nm}^2$ shown in Figure 2.5 with a cell size of 2 nm. A 300 nm domain is initialized at on the left-hand side of the wire. Then a vertical spin current is applied for 50 ns and at each nanosecond the domain walls positions are registered. The width of the domain is computed by the difference between the positions of the two domain walls, while the domain position is computed by adding half of the width to the position of the leftmost domain wall. This procedure is then repeated for different current steps.

As can be seen in Figure 2.6, the velocity increases up to $J = 2 \times 10^9\ \text{A}/\text{m}^2$. In this range the motion is followed by a domain expansion (see Figure 2.7). For higher current densities the velocity drops to a local minimum at $J = 4 \times 10^9\ \text{A}/\text{m}^2$ and increase again. Looking at the width of the domain during its motion, one can notice that the expansion of the domain is followed by a compression up to $J = 7 \times 10^9\ \text{A}/\text{m}^2$. After that value the domain firstly experiences a compression and then an expansion. One possible reason for this oscillatory behavior can be related to the Walker breakdown: at the beginning, the torque exerted by the current is supported by the demagnetizing field. This is the basic principle behind the steady-state regime. For higher values of $J \approx 2 \times 10^9\ \text{A}/\text{m}$, the demagnetizing torque is not able to balance the torque exerted by the current and the velocity

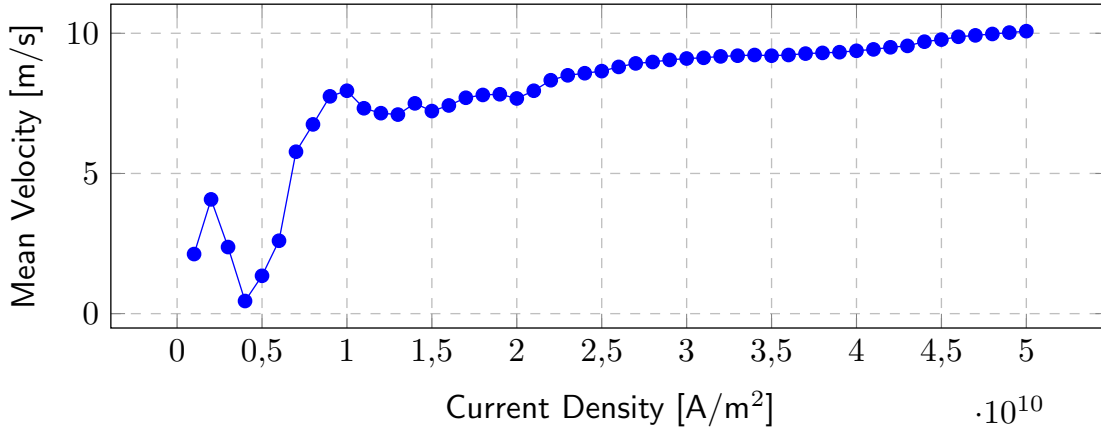


Figure 2.6: Domain velocity in the ideal case for $D = 0.03 \text{ mJ/m}^2$.

drops. Moreover, it has to be considered that the domain wall in this case is Bloch-type and, as shown by Mougín et al. in their work [10], the Walker breakdown can occur at zero field.

To better highlight the evolution of the domain position and width, in Figure 2.8 the two quantities, for three current steps, are shown. For low current densities, the domain expands, which means that the two domain walls move away from the center of the domain. However, the two domain walls do not move at the same speed. This can be noticed by considering that the increasing of the width, calculated by the difference of the domain walls position, is followed by an increasing in the domain position, calculated as the sum of the position of the leftmost domain wall and half of the domain width, corresponding to the center of the domain. In the second ramping of the velocity, the two domain walls move, but still not uniformly, as shown by the waving of the position in Figure 2.8a. Then for higher currents the velocity increases slowly, characterized by a linear evolution of the position and of the width.

The previous simulation was carried out considering a low DMI value. As shown by Thiaville et al. in their work Thiaville et al., the presence of the DMI forces the domain to enter into the Néel domain wall configuration. Moreover, the DMI helps the demagnetization field to counteract the current torques, shifting the onset of the Walker breakdown towards higher currents and the steady regime is extended.[20].

The velocity simulated with the parameters presented in Table 2.1 and with different values of the Dzyaloshinskii-Moriya interaction constant is shown in Figure 2.10. The first striking result is the difference in magnitude of the velocity values for low and high DMI. This result has been reported in literature [20] and it is confirmed for the material parameters listed in Table 2.1. Moreover, $D = D = 3$

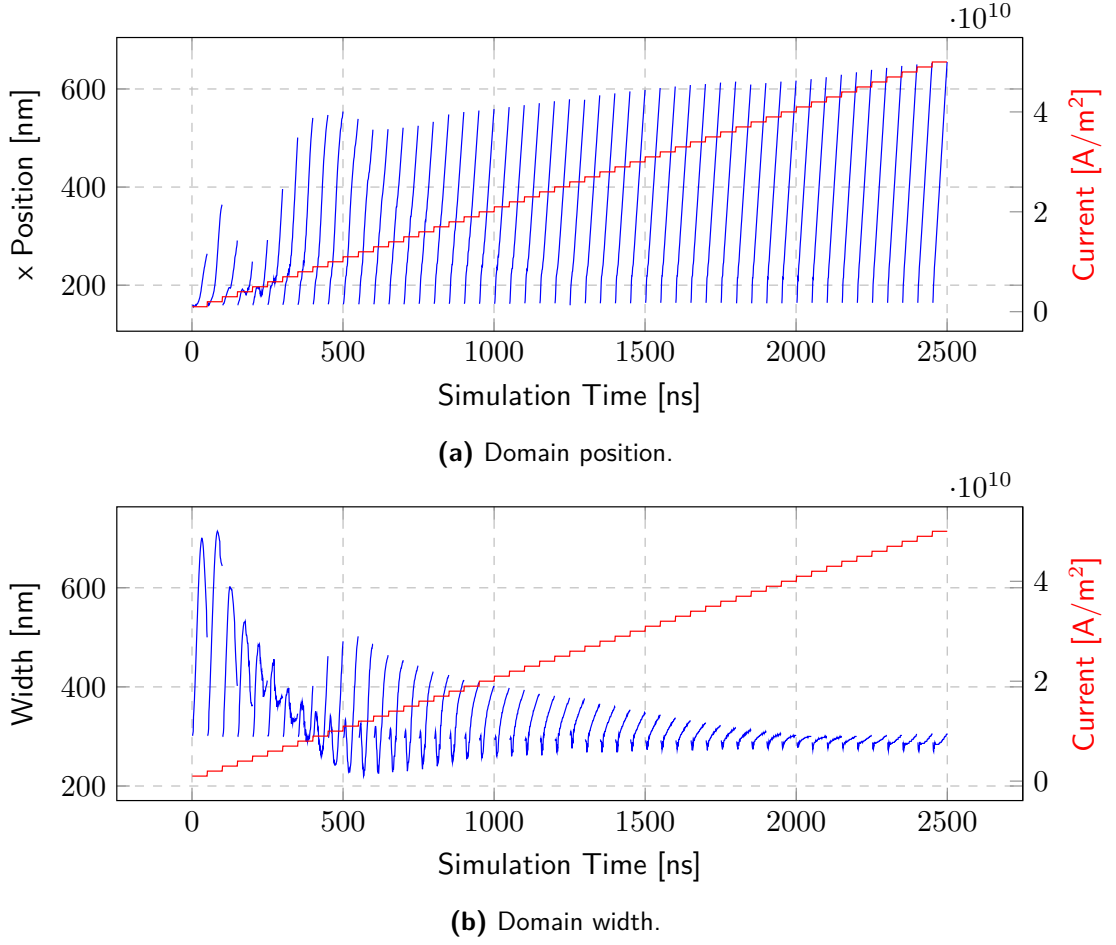


Figure 2.7: Evolution of the domain longitudinal position and domain width in the ideal case, for $D = 0.03 \text{ mJ/m}^2$, for different current density steps of 50 ns. After each step the domain is reset to its initial configuration, in which it has a width of 300 nm, while the initial position is 150 nm. The value of the current density of each step is depicted by the red curve.

mJ/m^2 the Walker breakdown is not visible anymore. This result is not expected, but the phenomenon could be masked by the high velocity values. Moreover, the increasing of the velocity saturates over a certain value of DMI, as one could notice by looking at the curves in case of $D=1\text{mJ/m}^2$ and $D=3\text{mJ/m}^2$.

The absence of the Walker breakdown is also confirmed by the trend of the domain width for high DMI strength (see Figure 2.11b), where the quantity reaches its stable configuration of $\approx 500\text{nm}$ already during the first nanoseconds of the simulation step time. It has to be noticed that the average width of the domain is higher in case of high-D with respect to the low-D case. During their motion, the domain walls are tilted by an angle, as shown in Figure 2.9, which means that,

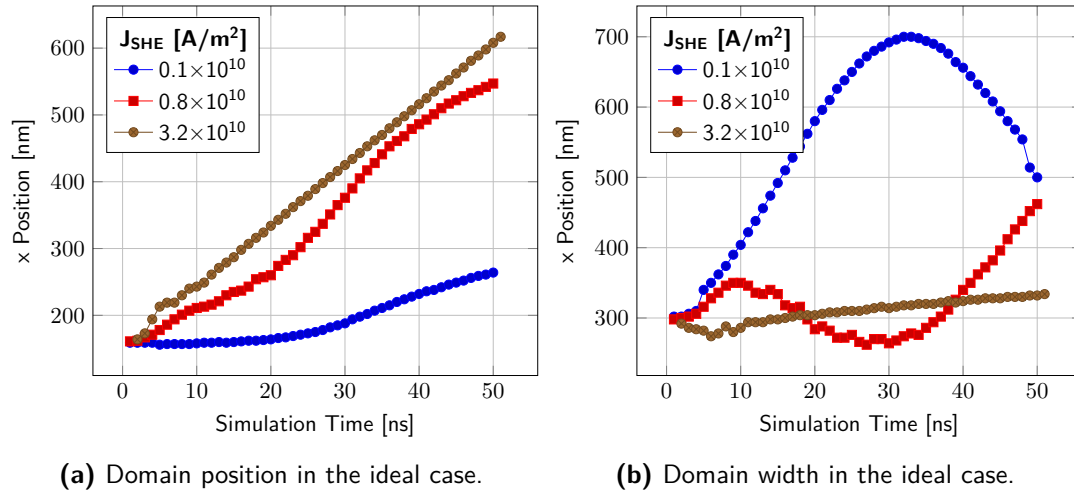


Figure 2.8: Domain position (a) and width (b) in the ideal case for low DMI strength (for $D = 0.03$ mJ/m²). The three current values correspond to the range before the first increase of the velocity, before the second one and in the saturated range.

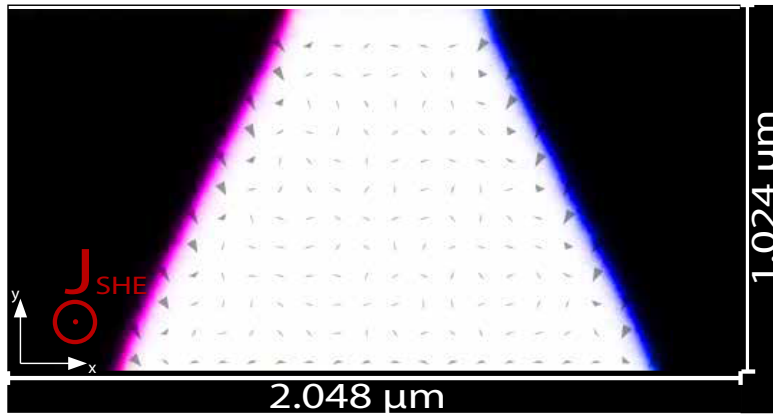


Figure 2.9: Simulation image of a domain moving in a $2048 \times 1024 \mu\text{m}^2$ wire by means of a spin Hall effect current for high DMI strength ($D = 3$ mJ/m⁻²).

since the position of the domain is calculated by analyzing the magnetization along x at a fixed height y , the width becomes dependent on the chosen height. Another possible reason could be related to the presence of the DMI that, similarly to the effect of the demagnetizing field, it favors the tilting of the atomic spins, causing the broadening of the domain walls. This is reflected also by the larger width of the domain, that remains stable with respect to the current density.

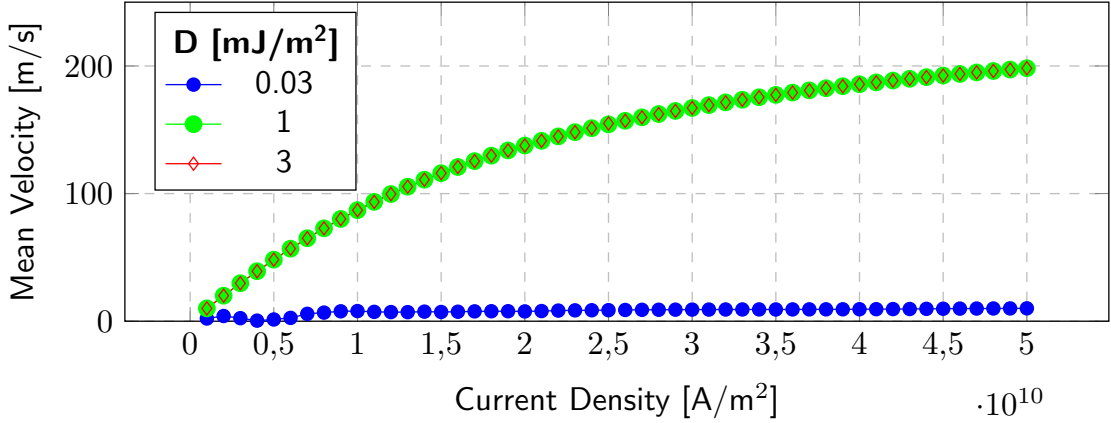


Figure 2.10: Domain velocity in the ideal case for different values of DMI coefficient.

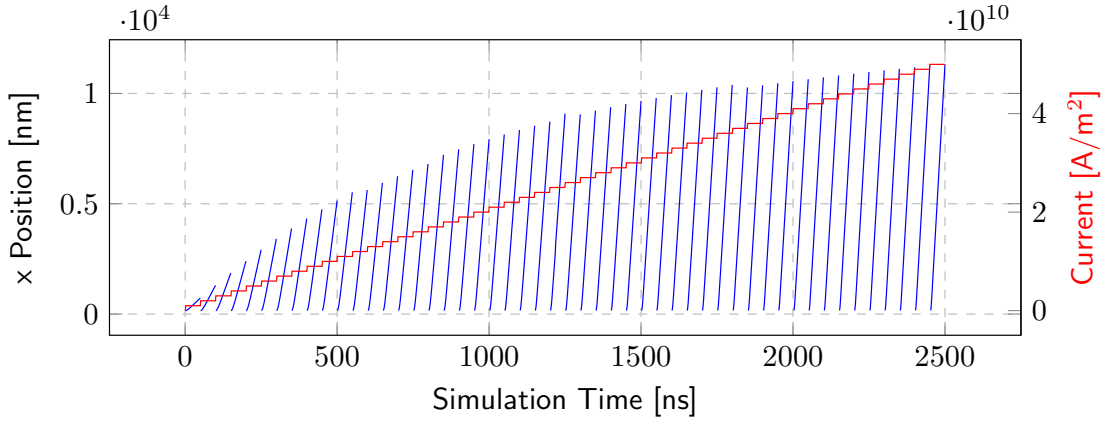
2.2.2 Temperature case

In this section the effects of the temperature on the motion of the domain are analyzed. From literature[21], it is known that a temperature different from zero decreases the critical current needed to ignite the motion of a domain wall. This because the temperature provides a thermal energy contribution that helps to overcome pinning barriers. In Figure 2.12 the result of the simulation for high DMI strength is shown. The velocity of the domain does not seem to be affected by the temperature with respect to the ideal case, both for low and high DMI. However, one difference can be found in the low-DMI case study: the Walker breakdown occurs at $J \approx 5.1 \times 10^9 \text{ A m}^{-2}$, which is higher than the Walker current density value in the ideal case.

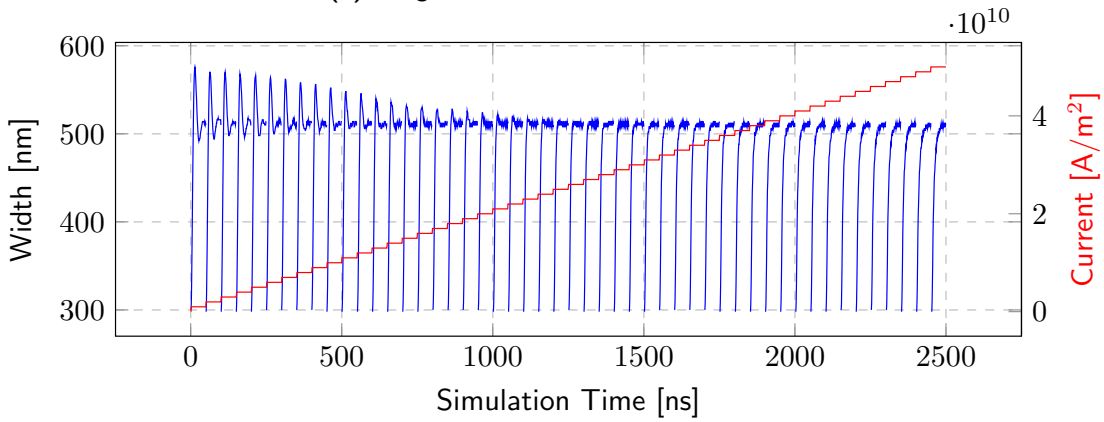
2.2.3 Material disorder

The last picture to be analyzed includes the contribution of the material grains, that naturally are formed during the crystallization of thin-films. The first consequence of the addition of material disorder is the creation of pinning sites at the grain interfaces[22]. They are regions in which the motion of the domain is obstructed by local variation of magnetic properties. In Figure 2.13 the microwire with grains, in which the anisotropy constant varies by the 5 % with respect to the nominal value listed in 2.1, is shown. The black regions are the ones with the lowest value of K_u , while the white ones have the highest K_u .

The domain velocity considering grains is shown in Figure 2.14. For intermediate values of DMI, such as $D = 0.1 \text{ mJ/m}^2$, one can recognize the different regimes: a tail due to creep regime, the velocity increasing in the depinning regime



(a) Longitudinal Position of the domain.



(b) Domain width.

Figure 2.11: Evolution of the domain longitudinal position and domain width in the ideal case, for $D = 3 \text{ mJ/m}^2$, for different current density steps of 50 ns. After each step the domain is reset to its initial configuration, in which it has a width of 300 nm, while the initial position is 150 nm. The value of the current density of each step is depicted by the red curve.

and the flow regime for higher current densities. It has to be noticed that the different curves have a current threshold at which the domain starts to move. A phenomenon absent in the ideal and temperature case studies and which is related to grains. Moreover, for $D = 0.1 \text{ mJ/m}^2$ the motion seems to start before the other two cases of lower and higher D value. A possible reason is that, the DMI favors the depinning of the domain by adding an energy contribution to the domain wall, however this does not explain the higher DMI case. Moreover, in figure the values of the velocity reported are the ones for which a presence of a domain is detected. This means that the motion of the domain is stable at higher currents in case of

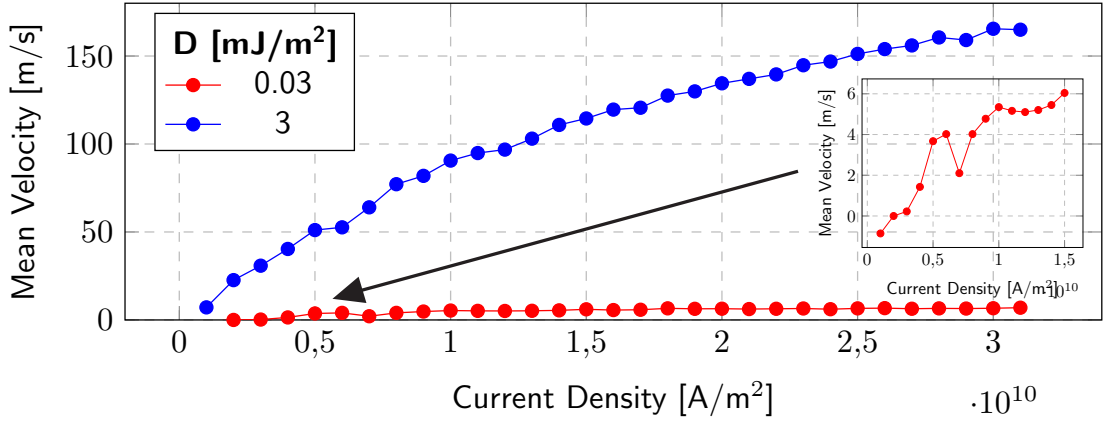


Figure 2.12: Domain velocity at a temperature of 300K for low and high DMI strengths.

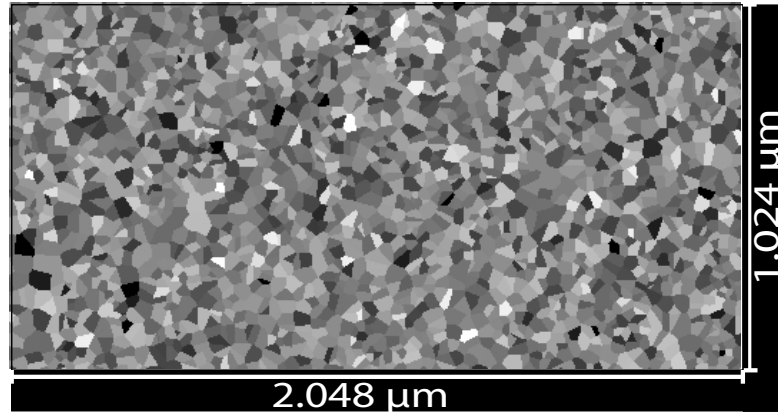


Figure 2.13: Example of grain distribution with a K_u variation of 5% with respect to the value of the ideal case.

intermediate DMI, while for $D = 0.1 \text{ mJ/m}^2$ the motion is unstable. Furthermore, it has to be considered, as mentioned before, that for low DMI ($D = 0.03 \text{ mJ/m}^2$) the domain walls are Bloch type, while in the other two cases they are Néel type. The velocity trend reflects the trend shown in Figure 2.4b. In the creep regime the domain motion is activated by local fluctuations, the depinning regime, which is a function of the variation of the material parameters, and finally the flow regime where the two previous effects are negligible [18].

The high-DMI case is also analyzed (see Figure 2.14, blue curve). Even in presence of the grains, having materials with high Dzyaloshinskii-Moriya interaction, the domain motion can still achieve high velocities. The grain case study has been tested also with $D = 3 \text{ mJ/m}^2$ as done for the ideal and temperature case, however simulation results show that the local variation of the material parameters make

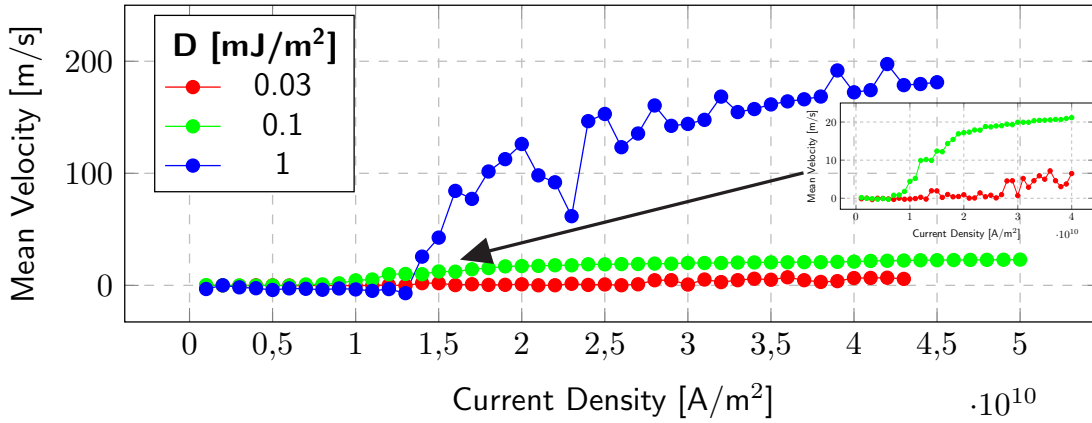


Figure 2.14: Domain Wall velocity in presence of grains with $D=0.1\text{mJ/m}^2$.

the domain motion instable at high velocities. Therefore, in order to achieve high domain velocities, the ferromagnetic material should present high average grain size, which means low material parameter variations.

2.3 Domain wall motion in microwires

In this section the experimental measurements of the current-driven motion of domain walls into micrometer wires are presented. The present work is divided into three experiments: i) producing a reliable nucleation process able to have a control over the position where the creation of a domain occurs; ii) the characterization of the current-driven domain motion thanks to a current injected into the ferromagnetic stack. In this experiment the domain velocity is measured as a function of the current density for different pulsewidths; iii) the last experiment is related to the exploration of a method to confine a domain, while allowing at the same time a motion. This is the basic principle of the information transfer into a magnetic racetrack memory [15].

The study is performed onto the ferromagnetic stack shown in Figure 2.1, whose fabrication process is described below.

2.3.1 Microwire fabrication

The fabrication of the micromagnetic wire involves different steps, which are presented below.

- **Sputtering.** The first step concerns the deposition of the thin films composing the ferromagnetic stack, depicted in Figure 2.1. Each magnetic film is

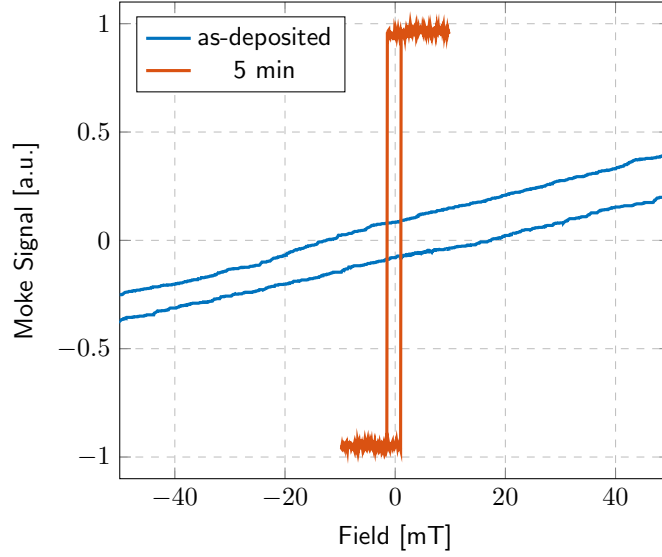


Figure 2.15: Hysteresis loops of $\text{Ta}_2/\text{CoFeB}_{1.1}/\text{MgO}_2/\text{Ta}_3$ before and after thermal annealing.

deposited via confocal RF-magnetron sputtering at room temperature onto silicon substrate, covered by a thermal grown silicon dioxide of ≈ 50 nm. The sputtering parameters used for the deposition are listed in Table 2.2.

Layer	Material	Power density [W cm^{-2}]	Pressure [$\times 10^{-7}$ mbar]	Time [s]	Thickness [nm]
Seed	Ta	0.5	4	43.8	2
Magnetic	CoFeB	0.5	4	39.4	1.1
Oxide	MgO	0.5	1	300.0	2
Capping	Ta	0.5	4	65.6	3

Table 2.2: $\text{Ta}_2/\text{CoFeB}_{1.1}/\text{MgO}_2/\text{Ta}_3$ sputtering parameters.

- **Thermal annealing** After the sputtering deposition, the sample undergo thermal annealing in N_2 atmosphere at 275 °C for 5 minutes. The thermal annealing ignites the crystallization of the CoFeB, which results in an increasing of the effective anisotropy K_{eff} , improving the PMA of the film [23]. As shown in Figure 2.15, after deposition the sample is in-plane magnetized, while after thermal annealing the sample shows a typical ferromagnetic hysteresis.
- **UV Lithography** The patterning of microwires is performed by means of optical lithography. It consists of different steps: firstly, the AZ ECI 3027 positive

photoresist is deposited on top of the sample using spin coating technique at 4000 rpm for 30 seconds after a pre-exposure bake at 150° for one minute. The sample is then exposed using a UV light which hits a chromium mask, reproducing its pattern. The illuminated sample is then immersed into the AZ 726 MIF solvent to remove the exposed photoresist, leaving the patterned non-illuminated photoresist which reproduces the chromium mask.

- **Ion beam etching** The aim of the photo resist is to protect the sample below it from the etching process. The latter can be performed by means of ion beam etching technique, in which of an Ar+ ion beam shot towards the sample, that rotates to uniformly etch away the non-masked magnetic thin film. The sample still have the photoresist on top of the patterned structures, which is then washed away from an acetone solution.
- **Metal contacts evaporation.** The last step involves the creation of the metallic contacts used to inject current into the microwires. To deposit the contacts, the process mentioned above are repeated using the negative resist MA-N1420, optical lithography and development with the MAD533S developer to wash away the non-irradiated negative photoresist. The result is a photoresist with the contact complement pattern. On top of the sample is then deposited, by means of thermal evaporation, a metal stack consisting of 15 nm of Ti as adhesive layer, 400 nm of Cu as contact material and a 50 nm Cr used layer to enable the bonding with external wires, to then inject a current.
- **Lift-off.** The fabrication process is completed by the lift-off process: the evaporated sample is put into an acetone solution to dissolve the photoresist as well as the metallic film portion on top of it, leaving the desired metal contact structures. The sample is then ready to be tested.

2.3.2 Nucleation mechanisms

The first task to be addresses is the creation of a domain. The nucleation process can occur thanks to an injected current or to an applied magnetic field. However, several critical aspects have to be considered, which are discussed below.

In general, starting from a completely magnetized wire, the nucleation of a domain can be due to:

- **Magnetic field.** An applied magnetic field, higher than the switching field, is able to nucleate a domain. The nucleation starts from weak spots, such as defects of the material. However, in order to create an isolated domain in the wire, the magnetic field has to be applied locally, avoiding the expansion of the domain throughout the whole wire. It means that one can use a setup able to

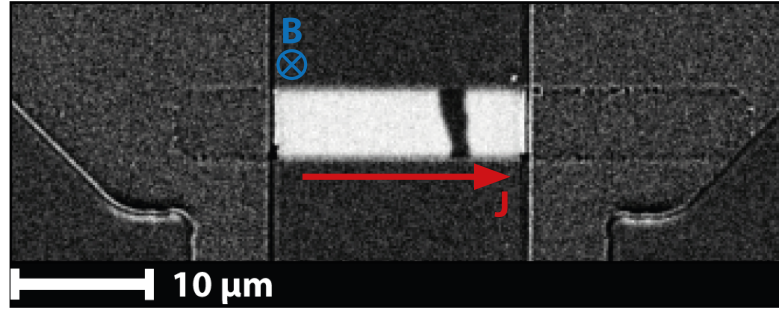


Figure 2.16: Domain Nucleation on a $50 \times 5 \mu\text{m}^2$ wire. The gap between the contacts is $25 \mu\text{m}$, which is the region in which the current flows. The nucleation current pulse is of $J \approx 7.2 \times 10^{11} \text{ A m}^{-2}$ for 150 ns and with a field offset of 1.5 mT .

create locally a magnetic field or one can apply very short pulses in the range of nanoseconds, in order to stop the expansion before the saturation of the wire. In the first case, the approach sets already a limit to the scalability of the application. In the second case, short magnetic pulses can be very effective because the nucleation can happen without the risk of damaging the wire, as would be the case of high current density pulses. However, having short magnetic pulses is not an easy task, especially at the research level. Moreover, if the field is not local and restricted to a magnetic wire, it influences also other ferromagnetic structures, such as other wires, which is not desirable for potential applications.

- **Electric current.** A current flowing into a ferromagnetic wire exerts torques on the magnetic moments, which can nucleate a domain. However, the torque, and accordingly the amount of current, needed to locally reverse the magnetic moments is higher with respect to the torque needed to move a domain wall. Higher current density means also an increase of temperature due to Joule effect. In the wire used for the domain velocity experiments, or in general in ferromagnetic wires used for spintronic devices, the cross-section of the wire is small and the temperature increasing can be too high. The increasing of the temperature could modify the magnetic properties of the wire by means of an induced thermal annealing. This phenomenon has been reported during the experimental studies of this work, where a decreasing of the switching field of the wire for high current densities has been observed.
- **Magnetic field and electric current.** The two nucleation mechanisms listed above can be used together to improve the nucleation process. The combination of the torques originating from both the magnetic field and the injected current can nucleate a domain using low current densities. This approach has been tested in the experimental studies of this work. An example of a

domain nucleated according to this approach is shown in Figure 2.16. A more detailed explanation of what seen experimentally is discussed in the section below.

2.3.3 Improving nucleation efficiency

As mentioned before, the best way to nucleate a domain is to have a combination of a short current pulse together with a field offset. In Figure 2.16 the result of the nucleation process is shown.

It has been observed experimentally that the nucleation happens in different steps (see Figure 2.17):

- The magnetic field offset of some mT perturbs locally the magnetization. In weaker spots, such as defects or the edges of the wire, the switching field is lowered due to inhomogeneties of the material parameters, leading to an enhancement of the magnetic field perturbation. When a current pulse is injected into the wire, the nucleation of many domains (Figure 2.17 (A)) or of a single domain (Figure 2.17 (D)) starts from the weak spots, thanks to the combination of the mentioned torques.
- Once the domain (or eventually the domains) is nucleated, it starts to expand due to the presence of the magnetic field offset (Figure 2.17 (B) and (E)).
- If the value of the magnetic field is not too high, the expansion stops when the domain walls run into other domain walls (Figure 2.17 (C)) or wire edges (Figure 2.17 (F)).

This approach has been found to be very effective, lowering the risk of degrading the material parameter due to high current densities. However, the control over the position where the domain nucleates is still missing.

2.4 Artificial Nucleation Centers

In the previous section, a method to improve the efficiency of the domain nucleation has been discussed. In order to establish a reliable nucleation process, a control of the nucleation site is needed. For the application point of view, it allows to define an input region from which the information, encoded into a domain, can be shifted towards the output, giving a directionality to the transferring of information. In this section, *artificial nucleation centers* (ANCs in short) are proposed to address this task. They are regions where the magnetic properties of the thin film are intentionally degraded, locally lowering the energy required to reverse magnetic

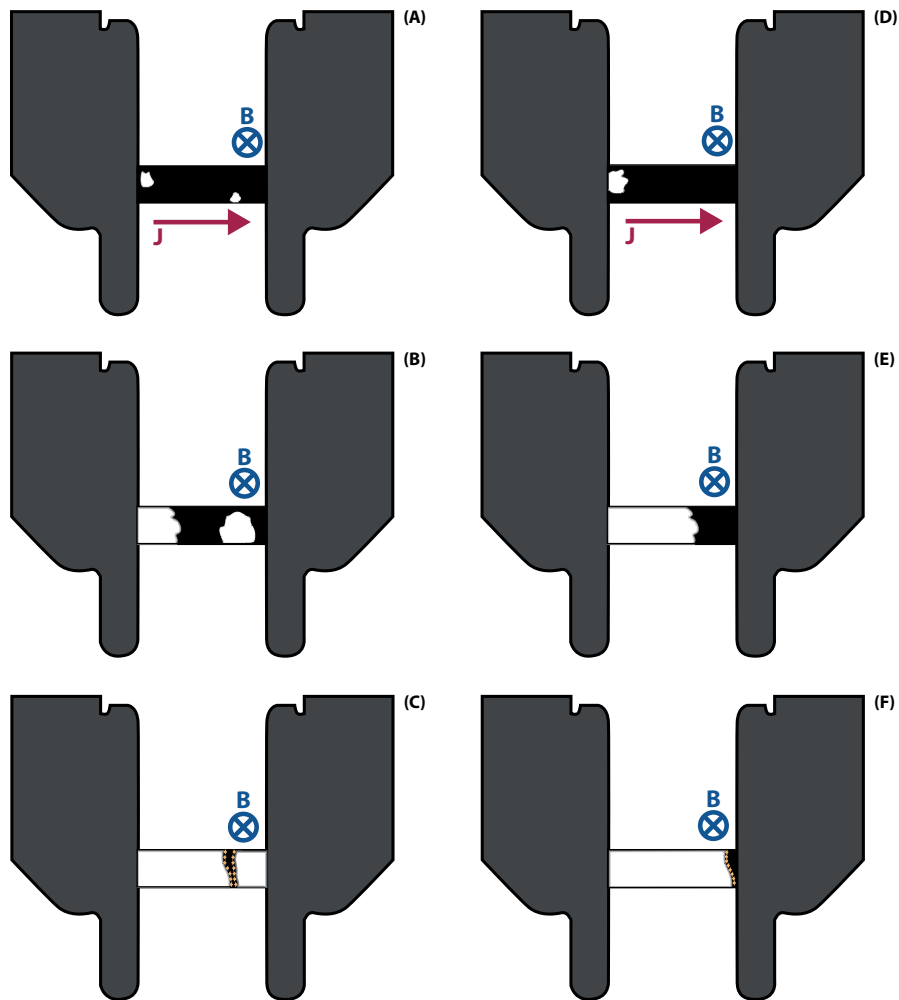


Figure 2.17: Domain nucleation scheme with a current pulse together with a field offset. Figures (A)-(C) show the formation of a domain starting from two defects. The nucleation is due to the superposition of current and field torques (A), then the domains expand due to the field offset (B), whose expansion stops when two domains are faced, leading to the creation of a domain with opposite magnetization with respect to the ones nucleated by current pulse (C). The field offset has to be chosen low enough to not overcome the repulsion force between the domain walls of the nucleated domain. Figures (D)-(F) show the same nucleation process, but starting from the nucleation, due to a current pulse, of one domain, whose expansion stops due to repulsion forces of the edges.

moments. The result is a local reduction of the switching field, making that regions the first to switch in respect to the thin film. It has been shown in literature that the material properties can be tailored by using Focus Ion Beam (FIB) irradiation

[24], in which ions are shot in a defined region of the sample.

As shown by Mendisch et al. in their work [19], where they studied the evolution of switching field with respect to Ga^+ ion doses (see Figure 2.18), the switching field, proportional to the effective anisotropy K_{eff} , increases for low and medium doses up to $\approx 3.5 \times 10^{13}$ ions/cm² and then it drops for higher doses. As can be seen, the domain size follows the trend of the curve, giving a qualitative estimation of the phenomenon. The same increasing trend is found also in the work of Devolder et al. [24], where He^+ ions are used and in which the trend is justified by the different decreasing rates of M_S and K_u . However, for high irradiation doses, the trend is not matched in the two works. A possible reason could be related to the different ions used during FIB irradiation, which have different masses.

In Mendisch et al. work, it has been shown that the best way to create effective artificial nucleation centers is to first irradiate a region (which is called *background irradiation* region) and to secondly to create an ANC inside it by means of a second irradiation. The scope of the background irradiation is to create an anisotropy gradient between the ANC and the pristine material. This results to be an effective way to overcome the barrier between a very low anisotropy region (ANC) and a higher anisotropy area (the surrounding pristine material). Subsequently, the second step involves the irradiation of the ANC geometry. It has to be mentioned that the ANC geometry influences the efficiency of the domain nucleation [19]. The effect of the ANC geometry will not be studied in this work, but it will be chosen according to the results of Mendisch et al. in their studies [19].

Upon Ga^+ ion irradiation, the thin-film stack used for this work shows the same trend, although at different irradiation doses. This means that, due to process variations, the tailoring of the material properties by means of FIB can be shifted to different ion doses depending on the sample. For this reason, in order to find the best ion dose for the ANC fabrication, an irradiation study on the ferromagnetic stack used for the domain wall motion experiment is needed.

2.4.1 Background irradiation

According to Mendisch et al. studies [19], the creation of an artificial nucleation center requires a preliminary step, called *background irradiation* consisting of an ion irradiation of a region containing the ANC position. The irradiation is found to produce an increase of the switching field, followed by an increasing of the average domain size, up to a certain value of ion dose [19]. After that, the switching field and the domain size drops (see Figure 2.18). Moreover, this process increases K_{eff} , as shown in literature [24], even in ion dose ranges where the switching field starts to drop [19]. In his work [19], Mendisch et al. show that the most effective background ion dose corresponds to the one for which the peak in the switching field trend is found and where a single-domain state is observed.

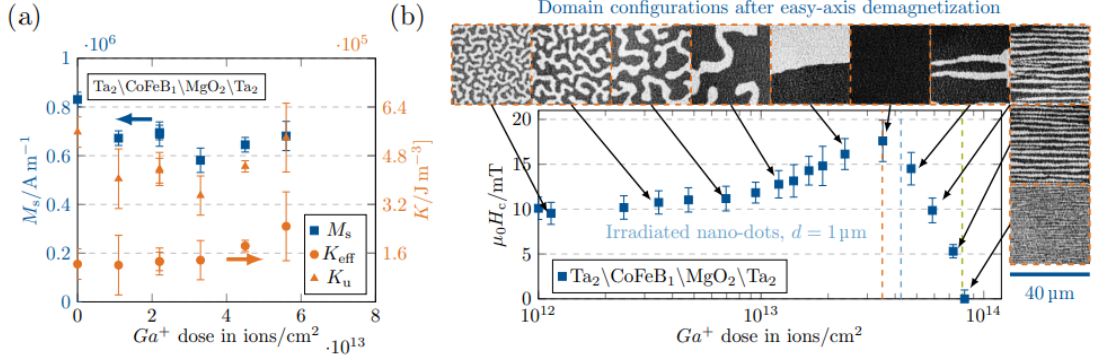


Figure 2.18: In (a) the measured values of M_S and K_{eff} for different ion doses are shown. K_u is derived considering $K_u = K_{\text{eff}} + \frac{1}{2}\mu_0 M_S$. In (b) it is shown the coercivity evolution with respect to the Ga^+ ion dose.

Square	Dose [ions cm^2]						
A	0.36×10^{13}	D	0.95×10^{13}	G	1.57×10^{13}	J	2.14×10^{13}
B	0.49×10^{13}	E	1.05×10^{13}	H	1.61×10^{13}	K	2.42×10^{13}
C	0.62×10^{13}	F	1.19×10^{13}	I	1.80×10^{13}	L	2.46×10^{13}

Table 2.3: Ga^+ ion doses used for the background irradiation study, whose results are shown in 2.19.

In order to reproduce the mentioned results, an irradiation study of the background irradiation has been performed by irradiating $19 \times 19 \mu\text{m}^2$ squares on the thin-film stack depicted in 2.1. The qualitative results of the domain size trend are shown in Figure 2.19, with the corresponding irradiation doses listed in Table 2.3. In the widefield magneto-optic Kerr effect (WMOKE in short) images, the domain size for low doses ((A) and (B)) remains equal to the one found in the pristine thin-film stack in the demagnetized state. As soon as the ion dose increases, the multi-domain state starts to be unstable in the irradiated square, meaning that the domain size is higher than the square and a single-domain state is achieved (D). For higher irradiation doses ((E)-(K)) the average domain size drops, leading to the formation of domains smaller than the optical resolution for high doses (L). According to Mendisch et al. studies [19], The best background (BB in short) irradiation is then chosen to be the one for which the single-domain state is observed, corresponding to an ion dose $\approx 1 \times 10^{13}$ ions/ cm^2 . The BB irradiation dose can be used to irradiate regions of the ferromagnetic stack to find the best ANC ion dose.

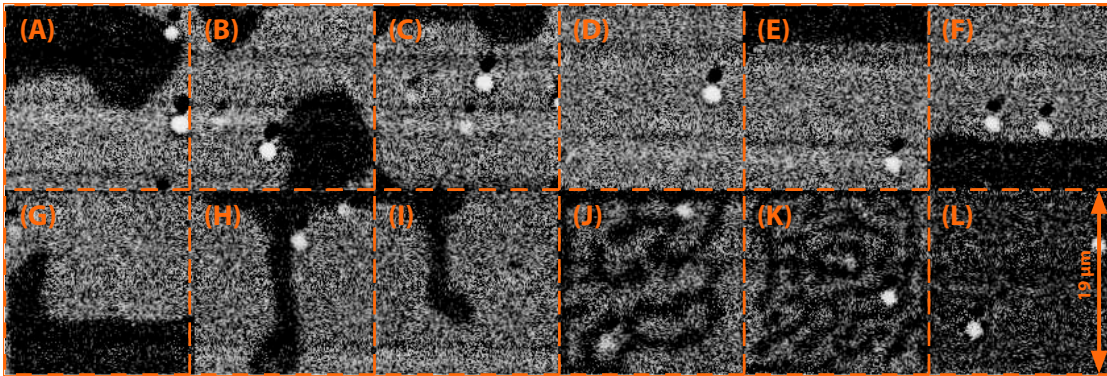


Figure 2.19: Background irradiation study. The Ta/CoFeB/MgO/Ta thin-film stack has been irradiated in different $19 \times 19 \mu\text{m}^2$ squares with increasing Ga^{2+} ion doses. In figure the some squares are reported, whose ion doses are listed in Table 2.3.

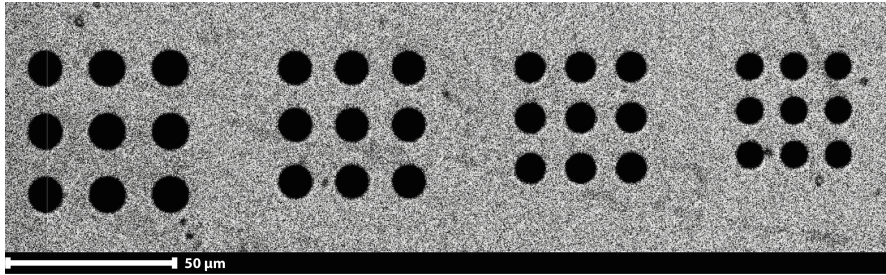


Figure 2.20: Widefield magneto-optic Kerr effect image of the ferromagnetic dots used for the ANC study.

2.4.2 ANC irradiation

After locally lowering the anisotropy in a well-defined area of the sample thanks to the background irradiation, the next step is to create the ANC in that region. The aim of the artificial nucleation center is to create a preferred nucleation site, determining a control of the nucleation position. It can be achieved by strongly lowering the anisotropy in a defined area [19]. In order to find the best ion dose for the creation of an artificial nucleation center, an irradiation study has been performed. For this purpose, circular microdots of the lithography test structures present on the sample have been irradiated with the background dose to lowering the anisotropy as discussed above. After that, the ANC is created by irradiating a 500 nm square onto the microdots. The switching fields of the dots after irradiation are measured and compared with the switching field before irradiation. In this way the dots can be analyzed quantitatively.

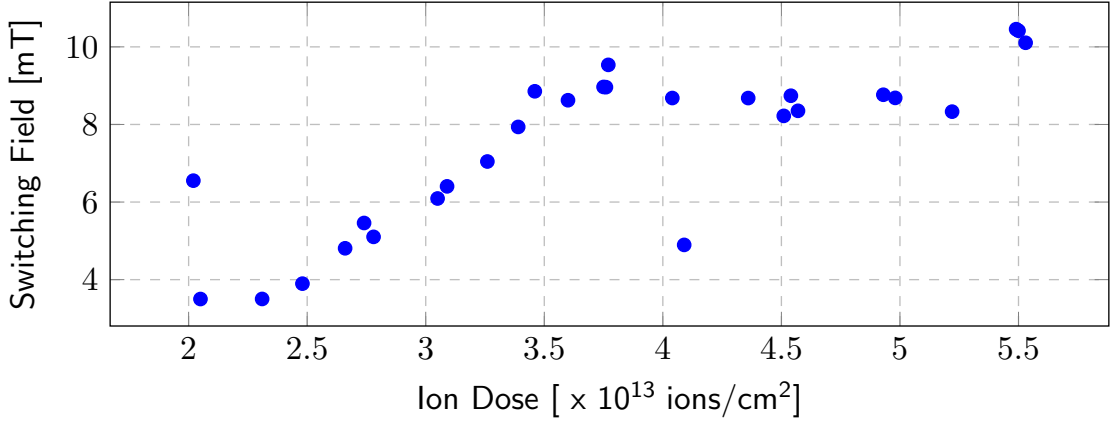


Figure 2.21: Evolution of the switching field with respect to the Ga^+ irradiation dose. The ion dose values include the background irradiation.

Irradiation	Dose [ions/cm 2]
Background	1×10^{13}
ANC	2.5×10^{13}

Table 2.4: Ga^+ irradiation doses for the background irradiation and for the artificial nucleation center, respectively. The ANC irradiation dose is the sum of the background irradiation, done before, and the new irradiation to reach the desired value.

The results of the analysis are shown in Figure 2.21. The depicted ion doses include already the BB ion dose. As can be seen, for low ion doses, the switching field of the microdots is decreased. As soon as the irradiation dose increases, the switching field increases again. This behavior could be explained by considering that the aim of the two-step irradiation (background and ANC irradiation) is to create a gradient between low and high anisotropy regions and if the ANC is strongly irradiated the anisotropy gap between the latter and the background irradiation becomes too high, vanishing the gradient effect. Stated that, the best irradiation dose for the artificial nucleation center is found to be around $\approx 2.5 \times 10^{13}$ ions/cm 2 , where the lowest switching field is observed.

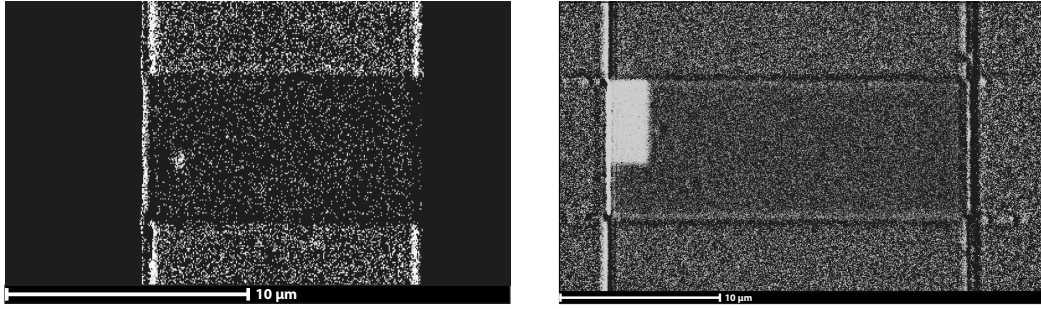
Summing up, the two irradiation studies led to the creation of a preferred nucleation site. This approach can be used to create artificial nucleation centers onto ferromagnetic wires to effectively nucleate a domain that can be moved by mean of an injected current. In order to confirm the reliability of this method, the two-steps ANC irradiation as to be tested onto patterned ferromagnetic microwires present on the sample and used for domain velocity experiments.

2.4.3 Irradiation on wire

To conclude the nucleation study, the last step is related to the attempt of proving the efficiency of the domain nucleation according to the two-step ANC irradiation described above. In order to do that, a ferromagnetic microwire is irradiated by means of Ga^+ ions FIB irradiation using a $5\ \mu\text{m}$ and $500\ \text{nm}$ squares for background and ANC irradiation respectively.

According to the combined current-magnetic field nucleation mechanism described in Section 2.3.2, the nucleation of a domain occurs after a current pulse of $J \approx 7.2 \times 10^{11}\ \text{A m}^{-2}$ for 150 ns with a field offset of 1.5 mT. In Figure 2.22 WMOKE images before and after the nucleation of a domain are shown. Before the injection of the nucleation current pulse, a magnetic field offset is applied. In this condition the WMOKE images (see Figure 2.22a) shows a bright spot corresponding to the ANC. It is expected since in the artificial nucleation center the switching field drops and the field offset is already enough to induce the magnetization reversal in that region. Another possibility that explains the brighter spot is that the ANC results in-plane magnetized, meaning that the magnetization is following the magnetic field. However, considering the previous ANC irradiation studies and considering the ion dose used for the irradiation, the ANC should be out-of-plane magnetized. In Figure 2.22 the background irradiation cannot be seen because, in agreement with what said in the background irradiation studies, the switching field has been increased, which means that the field offset is not able to overcome the anisotropy gradient between the ANC and the pristine wire. The latter could be overcome applying a higher field offset, but it would produce an expansion of the nucleated domain, leading to the complete saturation of the wire.

The effects of the background irradiation can be seen after the injection of the nucleation current pulse (see Figure 2.22b). In figure a misalignment of the background irradiation FIB mask can be noticed, but still the experiment results effective. After the current pulse, the nucleated domain expands thanks to the applied magnetic field offset. The expansion is stopped at the background irradiation region boundaries. It means that the background region is a well in terms of energy. It could explain why the domain, once nucleated in the ANC (low K_{eff}) it is favorable to expand in an irradiated region with the BB dose (high K_{eff}) with respect to the pristine wire. The discussion about creating traps by irradiating the film is done in Section 2.6.



(a) WMOKE image of an artificial nucleation center. (b) WMOKE image after the nucleation process with the domain confined.

Figure 2.22: WMOKE images before and after the nucleation of a domain. The two images are taken on different wires which are both $5\mu\text{m}$ wide, but with a different contact distance. The nucleation process is for both equal. Before the nucleation (a), the offset switches only the ANC (white dot), which it has lower switching field; after the nucleation (b) the domain expands until it reaches the background irradiation region edges, meaning that this region is energetically a trap.

Concluding, the nucleation studies so far discussed show an efficient and reliable way to nucleate a domain. This represents one of the requirements to the implementation of current-driven domain motion-based devices. In the application point of view, the next step is related to the characterization of the domain motion, which is addressed in the following section.

2.5 Velocity

In this section the experimental measured velocity of current-induced domain motion is discussed. In Section 2.2 it has been shown simulation results describing the behavior of the domain velocity with respect to the injected current density for different DMI strengths. In the experimental work, the information about the Dzyaloshinskii-Moriya constant is missing. Here we compare the experimental results with the simulative ones. The measurements of the domain velocity are performed onto a $50 \times 15 \mu\text{m}^2$, shown in Figure 2.23. The wire is contacted by two Cu wires deposited on top of the edges of the wire. The gap between the contacts is $25 \mu\text{m}$, which is the portion of the wire where the current flows and where the domain velocity is measured. The ferromagnetic material used is the one depicted in Figure 2.1. The measurement is composed by different steps, described below.

- **Nucleation.** Firstly, a domain has to be nucleated. The nucleation mechanism used for the domain velocity is the one depicted in Figure 2.17, since

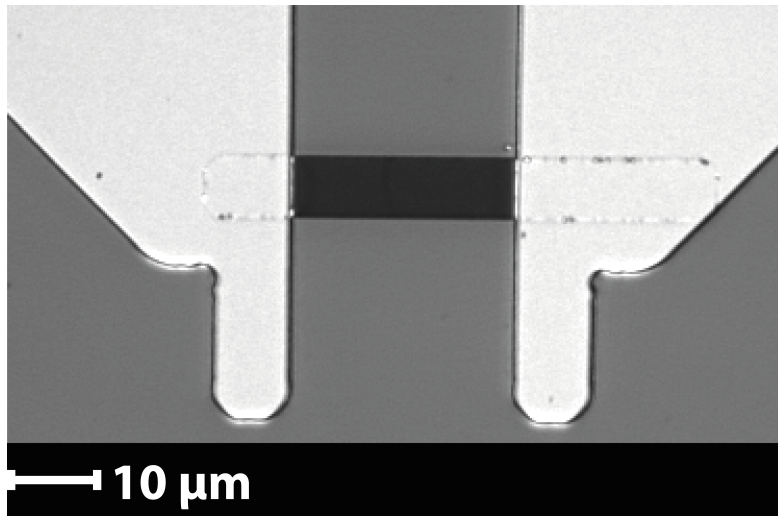


Figure 2.23: Setup used for domain velocity experiment. It consists of a ferromagnetic wire with dimensions of $50 \times 15 \mu\text{m}^2$. The gap between the contacts is $25 \mu\text{m}$, which is the region of the wire in which the current flows.

the ANC is not present. The nucleation optimization has been studied after completing the velocity experiment.

Once it is nucleated, the domain position adjusted by playing with the magnetic field in order to repeat the experiment with the same initial configuration, depicted in the top-left image of Figure 2.24.

- **Domain Wall Motion.** Once the domain is set, hundreds of current pulses are injected into the magnetic wire and the position of the domain is registered at each pulse, taking a WMOKE image.
- **Current Density Sweeping.** Both nucleation and current pulsing are repeated, sweeping over different current density values for different pulsewidths.

Some examples of images registered during one measurement are shown in Figure 2.24. As can be seen, the domain moves from left to right, which is also the direction of the current. At the same time, the domain expands, especially at the beginning of the motion, in order to reach the most energetically favorable configuration. During its motion, it can happen that the domain is pinned at pinning sites. They can be due to local defects present into the ferromagnetic thin-film, such as defects at the interface between CoFeB/MgO thin-films or due to the roughness of the edges of the wire which can act as notches. Moreover, during their motion, the domain walls are tilted. As shown in micromagnetic simulations, this could be related to the presence of DMI in the ferromagnetic film under test.

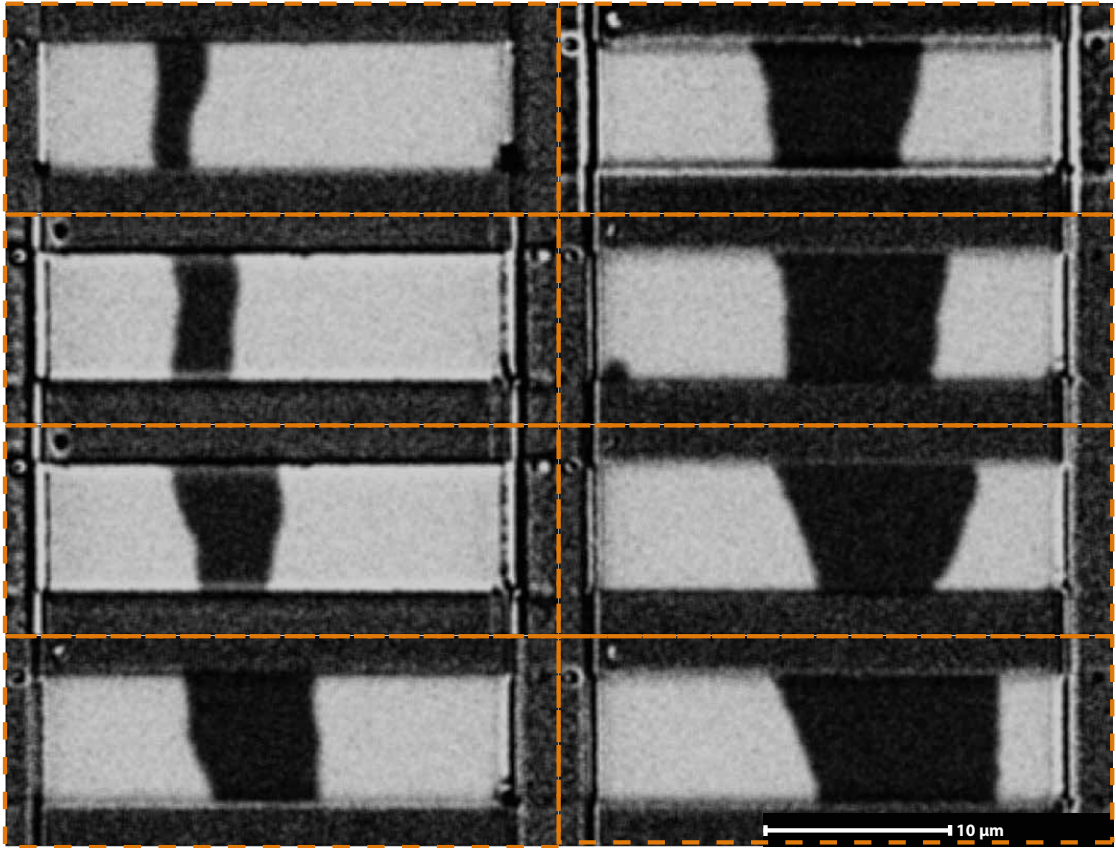
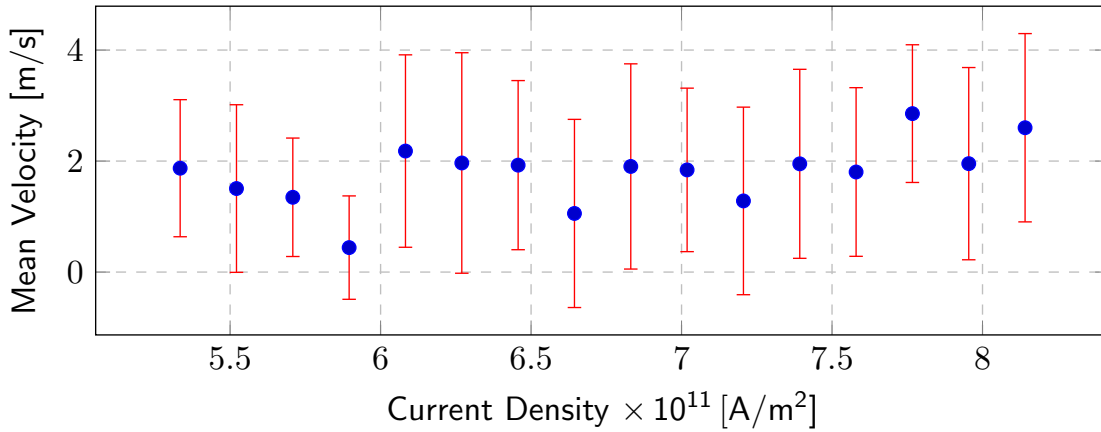


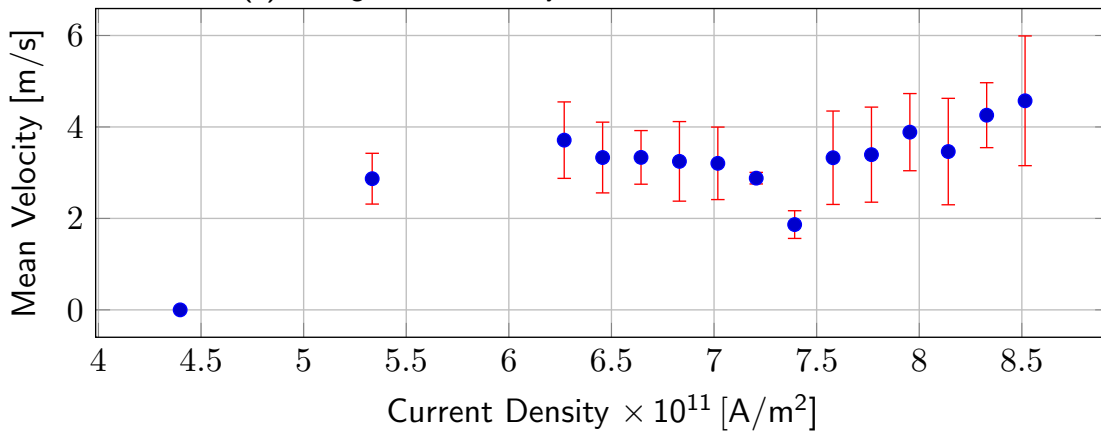
Figure 2.24: Example of domain motion images at different time stamps, in the microwire used for the domain velocity experiment. The images are taken after each current pulse of $J \approx 7 \times 10^{11} \text{ A m}^{-2}$.

The results of the measured domain velocity are shown in Figure 2.25 and Figure 2.26, for pulsewidth of 100 ns and 150 ns respectively. Considering the 100 ns picture, two plots are shown: in the first plot (see Figure 2.25a) the domain velocity is calculated by averaging over the values detected between consecutive images recorded at each current pulse, even when the domain does not move due to pinning effects, which corresponds to zero velocity entries. It means that the depicted velocity trend gives also a measure of the pinning events. In the second plot (Figure 2.25b) one can appreciate the measured domain velocity calculated only when the domain moves.

When increasing the pulsewidth to 150 ns, one can expect that the velocity does not change with respect to the 100 ns case. However, this is true unless thermal effects become relevant. Increasing the pulsewidth, the generated heat due to Joule effect increases. This case is the limit of the analysis because increasing further the pulsewidth means inducing thermal annealing to the ferromagnet due to heat



(a) Average domain velocity measured in the microwire.

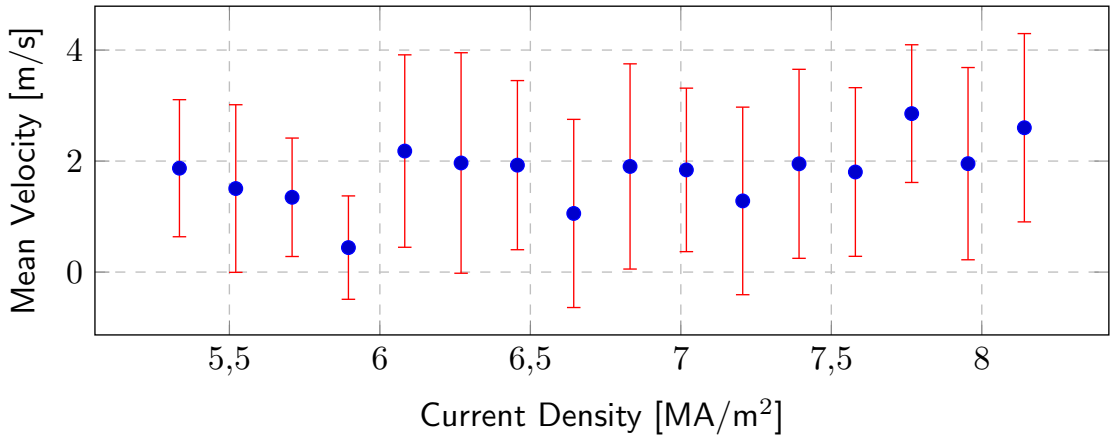


(b) Average domain velocity measured in the microwire without counting the pinning events.

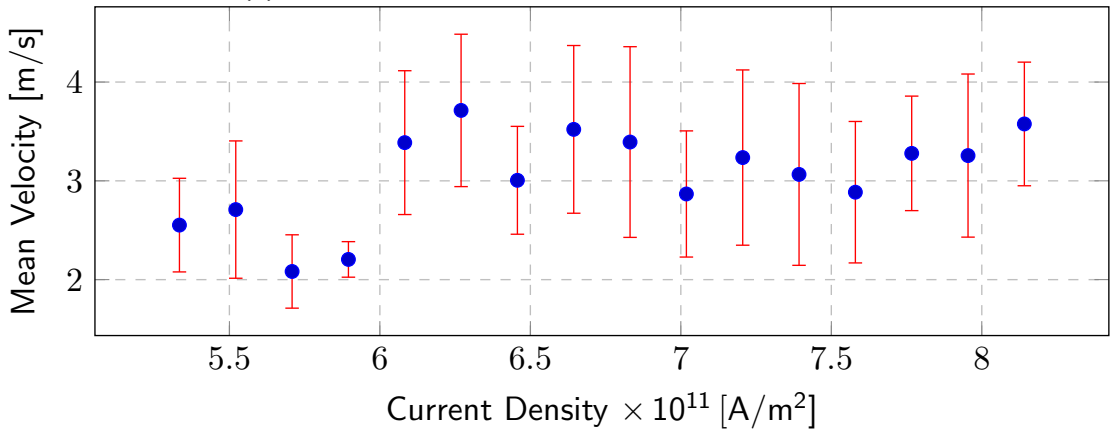
Figure 2.25: Evolution of the measured mean velocity with respect to the current density. The average is calculated over 100 pulses with a pulsewidth of 100 ns.

increasing, therefore inducing a degradation of the material properties. In Figure 2.26, the measurements with a pulsewidth of 150 ns show a slightly lower velocity trend. Looking at the values considering the pinning events (see Figure 2.26a) the difference between of the trend of two pulsewidths falls into the error range, but without considering the pinning events the velocity seems to be slightly lower. This could be related to thermal effects that raise already at 150 ns.

Concluding, the domain motion experiment shows velocity values, in case of 100 ns of pulsewidth, around 3 m/s, with a slight increasing for current densities up to 5 m/s. It has been shown experimentally that higher currents densities damages the ferromagnetic wire due to Joule effect. Considering current densities below 8.5×10^{11} A/m², the domain shows a motion influenced by pinning sites. It means



(a) Average domain velocity measured in the microwire.



(b) Average domain velocity measured in the microwire without counting the pinning events.

Figure 2.26: Evolution of the measured mean velocity with respect to the current density. The average is calculated over 150 pulses with a pulsewidth of 100 ns.

that the domain width can be altered during the motion. From the application point of view, in which the domain encodes an information and the number of domain into a track defines the number of information that can be stored, the width variation leads to an unwanted variation of the information density. Below, an approach to confine domains in order to have a regular spacing of domains, while still allowing their motion through the wire, is proposed.

2.6 Barriers

Another key concept to build devices such as racetrack memories is to have a controlled domain motion. As seen in the previous section, the motion of the domain

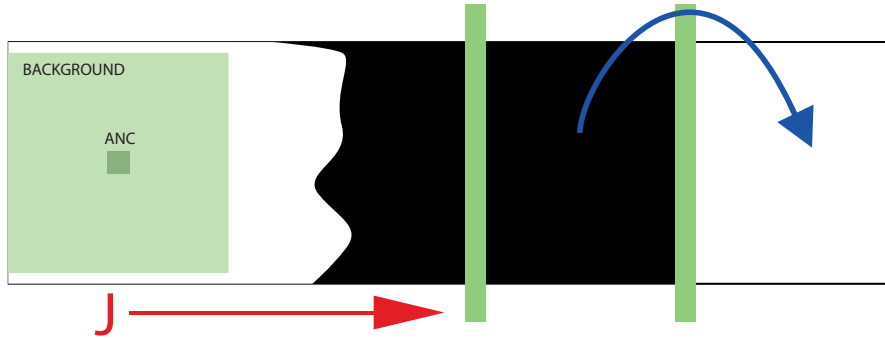


Figure 2.27: Schematic representation of domain nucleation and domain shifting from one memory cell to another. The latter are regions confined by Ga^+ ion irradiated barriers.

is very sensitive to homogeneity of the magnetic thin film, when a domain faces a pinning site it can be deformed or even annihilated, causing loss of information. In this work a solution to have a stable and controlled motion of domains is presented. An example of the main idea is shown in Figure 2.27. It consists of exploiting energy barriers to confine a domain, avoiding unwanted expansions due to the pinning of one domain wall with respect to the other (as shown in the previous section), but at the same time to allow the domain shifting between the different barriers.

2.6.1 Barrier Demonstration

The mentioned energy barriers can be realized by irradiating, by means of Ga^+ Focus Ion Beam, 500 nm width lines perpendicularly to the longitudinal direction of the ferromagnetic wire, as shown in Figure 2.28. Depending on the ion dose, the material parameters will be locally degraded, leading to a pinning of the domain. Below, a tuning of the barrier strength as a function of the ion dose is discussed. The experiment consists of an irradiation of $0.5 \times 19 \mu\text{m}^2$ barriers with different doses along a $8 \times 500 \mu\text{m}^2$ stripe (see Figure 2.28). The barrier ion dose increases from the left to the right, as shown in the figure. The choice is justified by the assumption that a higher ion dose produces a stronger barrier, which is then confirmed by the experiment results.

On the left edge of the stripe, an ANC is positioned, fabricated according to the recipe explained in Section 2.4. Being the stripe long enough, it is possible to nucleate a domain using magnetic field pulses with millisecond pulsewidths: after the nucleation the domain wall moves towards the right edge of the wire, however it is not fast enough to reach it during the time in which the pulse is applied. In case of contacted wires used for the current-induced domain motion,



Figure 2.28: Irradiation scheme in scale of a long stripe to tune the barrier strength. The nucleation of the domain wall occurs on the left-hand side of the stripe due to background and ANC irradiation. The ion dose, as well as the barrier strength, increases from left to right over the different barriers.

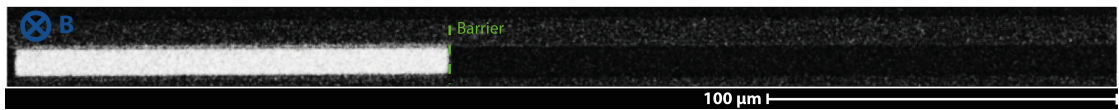


Figure 2.29: Widefield magneto-optic Kerr effect image of a portion of a 500×8 μm stripe. It is a frame of the measurement of the field-driven domain wall motion through the different barriers.

it is not possible, since the setup used for this work is not able to create magnetic field below the millisecond range. It means that, if the wire is not long enough, the nucleated domain expands over the whole wire. In the long stripe, once the domain is nucleated, it can be retracted back to the initial position, behind the first barrier.

An example of the domain wall motion through the stripe is shown in Figure 2.29. The magnetic field is swept from the first value at which the domain wall stops at the first barrier (around 0.65 mT), up to 2.3 mT, corresponding to the magnetic field value at which the domain wall stops at the last barrier. For each value of the magnetic field, 30 pulses, with a pulsewidth of 5 ms, are applied for lack of statistics. The first barrier able to stop the domain wall is found to be the one corresponding to an ion dose of 6.43×10^{12} ions/cm². Barriers with lower ion dose do not affect the domain wall motion, while for ion doses higher than 1.11×10^{13} ions/cm² the barriers are able to retain the domain wall up to the switching field of the stripe, which is not wanted from an application point of view, since the domain should be able to overcome them when a transfer of information, encoded into the domain, is required.

The magnetic field trend as a function of the barrier ion doses is shown in Figure 2.30. As expected, increasing the magnetic field, the domain wall is able to overcome higher energy barriers. This results will be taken in consideration to tune the barrier irradiation dose also in case of current-driven domain wall motion (see Section 2.6.4). One important aspect to be considered in this experiment is related

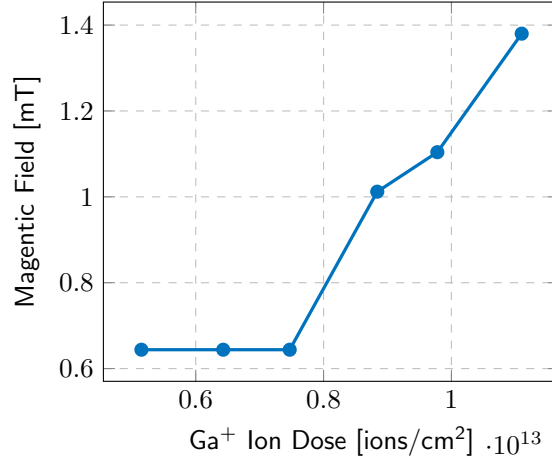


Figure 2.30: Measured magnetic fields at which a crossing of the different Ga⁺ irradiated barriers is recorded.

to the question: is the barrier really a higher energy barrier or an energy well? In other words, is the energy associated to the barrier higher or lower with respect to the pristine regions? Experimentally, it has been observed that when the domain wall gets close to the barrier, it seems to be attracted to it. It means that, for the domain wall, it is energetically favorable to fall into the barrier region, leading to the assumption that the barriers are energy wells, acting as a trap. This is the case of Figure 2.29, where it was found that, starting from that configuration, the domain wall does not move anymore until a threshold field is reached, even trying to apply an opposite magnetic field to retract it. To confirm this assumption, one can look at Figure 2.22b, it is clear that the domain is stopped at the barrier edges, meaning that the pristine region has a higher energy landscape with respect to the background region. It can be counterintuitive, especially considering that the irradiation induces an increasing of the effective magnetic anisotropy [19][24].

To sum up, in the background irradiation the average domain size is increases, which means that the effective anisotropy increases, leading to the assumption that, being M_S and K_u degraded after irradiation [19], the decreasing of the magnetostatic term present in K_{eff} (in which the dependence of M_S) is quadratic, is higher respect to the decreasing of the uniaxial anisotropy. However, energetically, it means that the energy of the system is decreased. This could also explain why the creation of an ANC works better with the background irradiation, acting as an intermediate energy step between the ANC and the pristine ferromagnet.

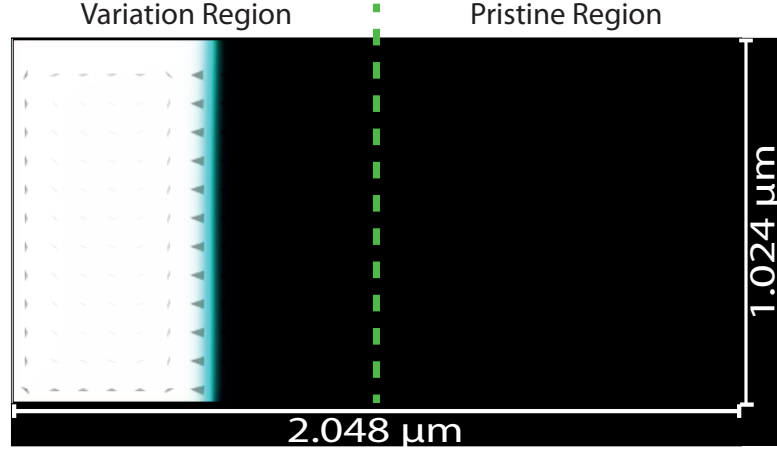


Figure 2.31: Simulation image of a domain wall moving in a $2048 \times 1024 \mu\text{m}^2$ wire by means of a spin Hall effect current for high DMI strength ($D = 1 \text{ mJ/m}^{-2}$). The dashed line divides the variation region, which is the region in which M_S and K_u are varied, and the pristine region, in which the material parameters are the ones listed in 2.1.

2.6.2 Barrier simulations

To better understand the behavior of the domain in the barrier, some simulations have been performed considering a current-induced domain wall motion through regions with different uniaxial anisotropy coefficient. The simulation setup is shown in Figure 2.31, which consists of two regions: the left half of the wire, called variation region, is the region in which K_u and M_S are varied; in the right half of the wire, the pristine region, the simulation parameters correspond to the ones listed in Table 2.1, with $D = 1 \text{ mJ/m}^2$. At 300 nm from the left edge, a Néel domain wall is initialized in the variation region (see Figure 2.31). A vertical spin current J_{SHE} current, due to spin Hall effect, is injected into the wire for 10 ns, which is swept from $1.2 \times 10^{10} \text{ A/m}^2$ to $5 \times 10^{10} \text{ A/m}^2$, that is the range where the domain moves, as shown above in the previous simulations.

For each K_u and M_S value, the position of the domain wall is registered. In Figure 2.32 a phase diagram showing when the domain wall escapes from the variation region is depicted.

The escaping of the domain wall occurs only for certain values of K_u and M_S . The background color of the diagram shows the behavior of K_{eff} . As can be seen, the region of the diagram where the domain wall escapes from the variation region, corresponds to points where K_{eff} is constant with values in the range of $0.95 \div 1.35 \times 10^5 \text{ J m}^{-3}$. For lower values of K_{eff} (high values of M_S and low values of K_u) the domain wall is not able to overcome the transition between the two

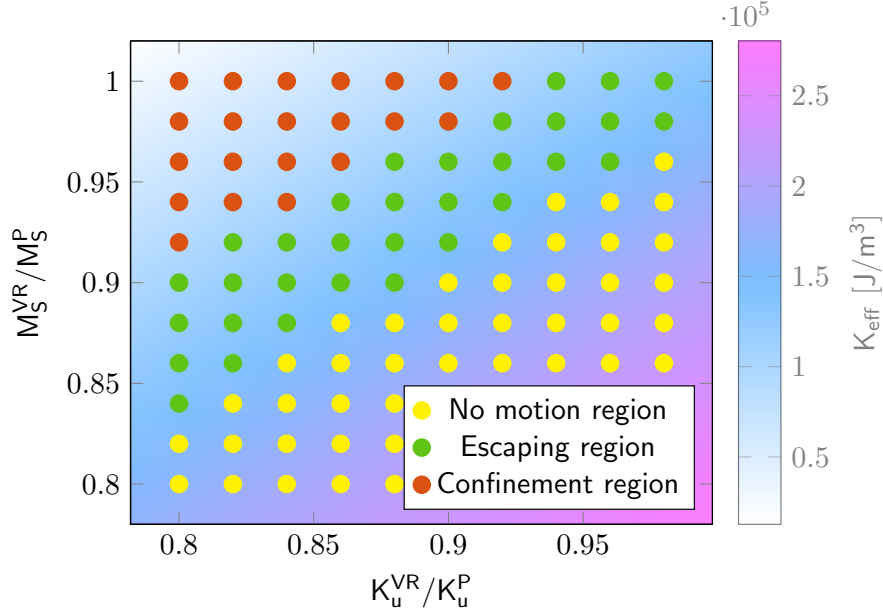
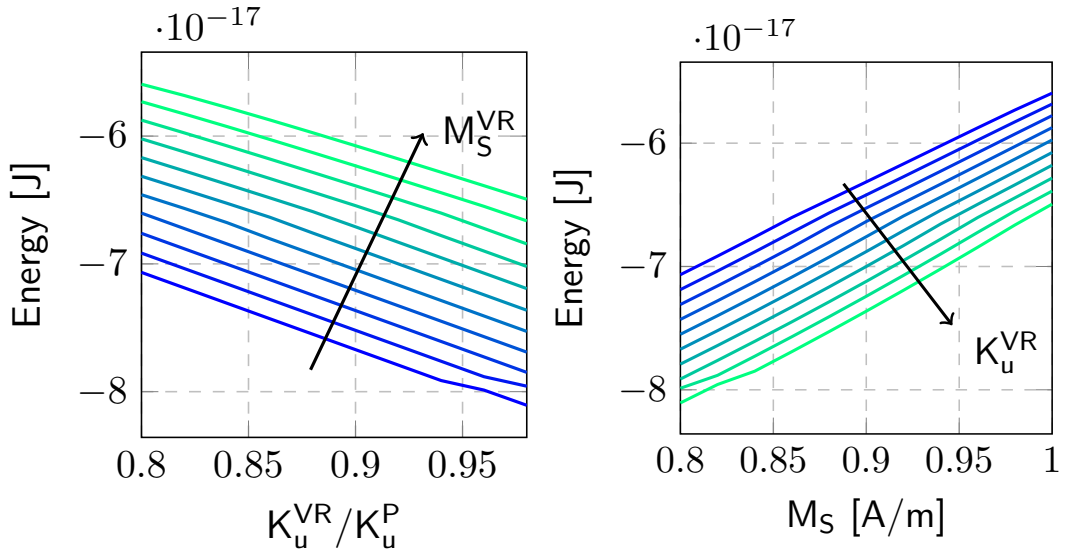


Figure 2.32: Phase diagram showing the K_u and M_S values for which the domain wall escapes from the variation region. K_u^{VR} and M_S^{VR} are the uniaxial anisotropy coefficient and the saturation magnetization in the variation region. The axes show the ratios between the variation region parameters and the ones in the pristine region, which are the ones listed in Table 2.1 with $D = 1 \text{ mJ/m}^2$. The yellow dots correspond to simulations in which the domain wall did not move; the green ones are related to the simulations in which the domain escaped from the variation region; simulations with the parameters of red dots showed a domain reaching the transition between the variation and the pristine regions, but it was not able to overcome it. The background color corresponds to values of K_{eff} calculated with the K_u^{VR} and M_S^{VR} parameters.

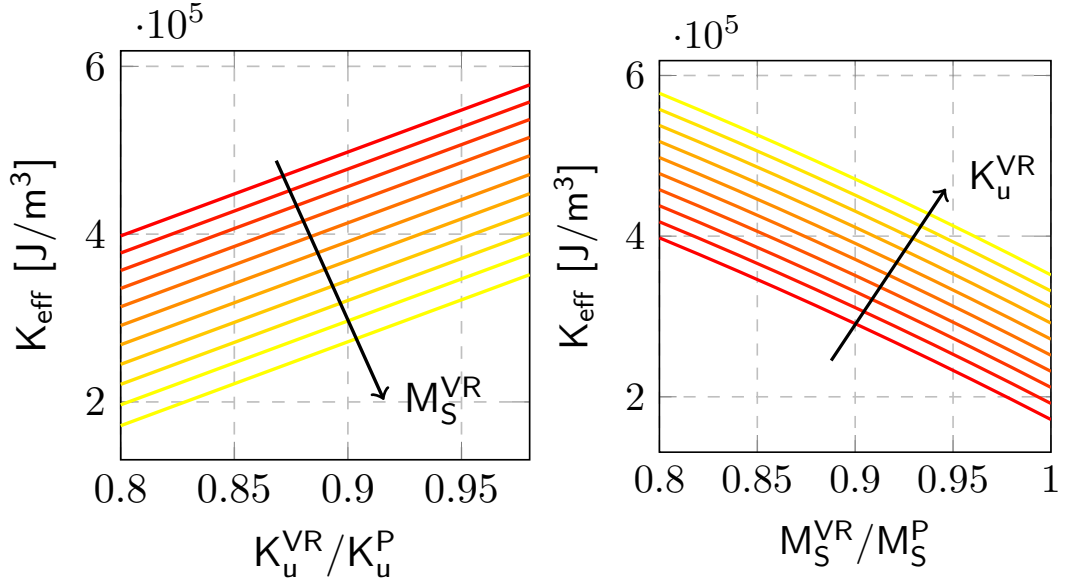
regions. For high K_{eff} values (low M_S and high K_u), no domain wall motion is observed. This could be due to the different material parameters that could set a higher current threshold to start the domain wall motion.

Looking at the diagram, if M_S and high K_u are degraded with the same rate, so following the values having the same x and y coordinates, it can be seen that K_{eff} slowly increases, this because its dependence on M_S is quadratic. In our experiments assuming the same rate of degradation, this could explain why the domain size increases, being the domain size related to K_{eff} . In order to explain why the barriers result to be wells for domain walls, one should consider the behavior of the total energy of the system as a function of M_S and high K_u .

In Figure 2.33 the trends of the total energy of the system, which includes both variation and pristine region, and of K_{eff} in the variation region with respect to



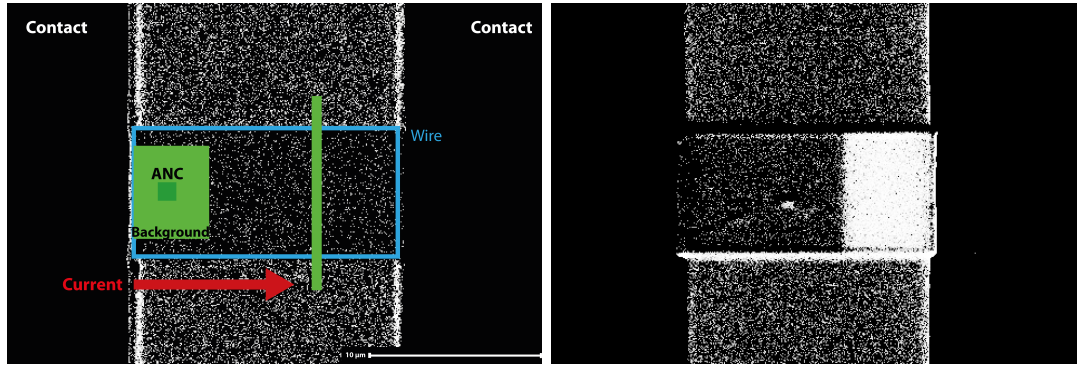
(a) Energy evolution with respect to K_u^{VR} at different M_S^{VR} values. (b) Energy evolution with respect to M_S^{VR} at different K_u^{VR} values.



(c) K_{eff} evolution with respect to K_u^{VR} at different M_S^{VR} values. (d) K_{eff} evolution with respect to M_S^{VR} at different K_u^{VR} values.

Figure 2.33: Variation of the energy and of K_{eff} for different values of K_u^{VR} and M_S^{VR} . The energy increases when K_u^{VR} decreases or M_S^{VR} increases, while K_{eff} shows the opposite trend.

K_u^{VR} and M_S^{VR} (which are the uniaxial anisotropy and the saturation magnetization values in the variation region) are shown. One can notice that the total energy of



(a) Example of the measurement setup used for the tuning of the barrier with current-induced domain wall motion. (b) WMOKE image of a domain wall stopped by the barrier. The black nucleated domain is pushed toward the barrier by a current.

Figure 2.34: Irradiation scheme (a) and WMOKE image (b) of a 5 μm wide wire used for measuring the domain wall motion through an irradiation barrier.

the system decreases increasing K_u^{VR} , while it increases when M_S^{VR} increases.

According to what observed experimentally in the barrier and in the nucleation experiments, the simulations support the assumption that the ion irradiation degrades the material parameters and the rate of degradation of M_S is higher, because if so, K_{eff} increases explaining the increasing in the domain dimension, while the total energy decreases, explaining why the barriers and the background irradiation are energetic wells.

2.6.3 Current-induced domain wall motion through barriers

It has been demonstrated that irradiating ferromagnetic structures is it possible to stop the field-induced expansion of a domain creating energetic barriers, which can be overcome for a certain field threshold. However, the most important question for our final goal is: are we able overcome such barriers with a current? In other words, is the effect of the current-induced torque able to provide enough energy to escape from the barrier?

In order to answer to this question, a ferromagnetic wire patterned onto the CoFeB/MgO stack (depicted in Figure 2.1) has been irradiated in order to create a barrier along the domain motion path. The irradiation scheme is shown in Figure 2.34a, which consists of a $0.5 \times 19 \mu\text{m}^2$ barrier placed in the middle of the wire and an ANC, together with the background irradiation, near the left contact in order to nucleate the domain before the barrier, accordingly to the direction of the current. The same irradiation pattern is then repeated for different wires, changing the barrier dose.

In Figure 2.34b, an example of a domain stopped in correspondence of a barrier

is shown. Starting from this configuration, a current pulse is injected into the wire with a pulsewidth of 100 ns and repeated 100 times. The current density is then swept from $\approx 4 \times 10^{11}$ A/m² to $\approx 1 \times 10^{12}$ A/m².

As done for velocity measurements, at each current pulse an image is recorded and then the position of the domain wall is compared to the position of the barrier to understand when it is overcome. The different curves are computed by counting the number of events in which the domain crosses the barrier (favorable events), over the total number of event. The difference between the favorable events and the total events gives the number of unfavorable events in which the domain does not cross the barrier.

The first barrier analyzed is the one with an irradiation dose of 5.52×10^{12} ions/cm², in which two initial domain wall configurations have been tested: positive domain on the left and negative domain on the left (which in the WMOKE images used in this work they correspond to black and white domains respectively). This to test the presence of field offset that can influence the crossing of the barrier. The results of this preliminary test can be found in Figure 2.35 curves blue and light blue. At $J \approx 8.5 \times 10^{11}$ A m⁻² the probability rises in both cases as expected, even though the probability in the case of a negative domain seems to be lower. However, the study needs a further exploration, not done for lack of time.

Taking into account the different barrier irradiation doses, the probabilities of the domain wall to cross the barrier as a function of the current density and for different barrier irradiation doses are shown in orange and bordeaux curves (see Figure 2.35).

As can be seen, the different curves are shifted at different current density values. One could expect that lower is the irradiation dose of the barriers and lower will be the current density needed to shift the domain from one region to the other. However, the plots in Figure 2.35 show a different trend. This could be related to the fact that the different doses have been tested on wires having different widths. Even considering it in the calculation of the current density, there could be a difference in the resistance of the ferromagnetic wire which shifts the expected nominal current towards lower values. Nevertheless, each probability curve have a recognizable increasing trend. Moreover, the lowest and the highest doses have been tested onto two wires of the same width and the shift of the two curves can be clearly noticed, which can be related to the different energy associated to the different barrier irradiation doses.

Concluding, the experiment shows that irradiation barriers can be used to stop a domain wall and that they can be overcome using current pulses. For lack of time, the experiment needs a further study to better characterize the crossing probability.

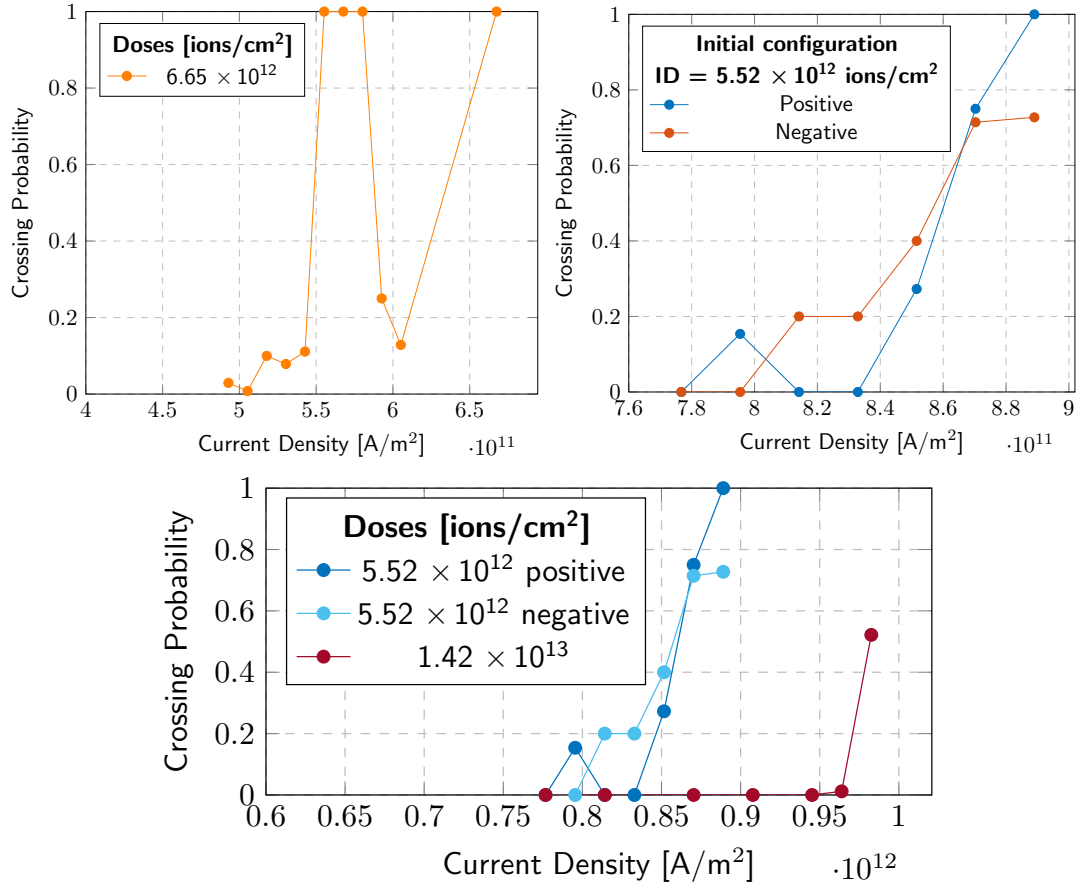


Figure 2.35: Probability curves of the domain wall crossing the irradiation barriers with different doses.

2.6.4 Domain shifting

The last step towards the realization of a preliminary memory bit cell consists of the realization of adjacent regions in which a domain can be confined and shifted from one region to the other. This is the working principle of the Racetrack Memory described in Section 1.4.

As shown in Figure 2.27, the aim is to have a controlled movement of the domain using irradiation barriers. In Figure 2.36 an attempt of demonstration of the domain shifting, in a $10 \mu\text{m}$ wide wire, between one region confined by two barriers and the successive one is shown. It has to be mentioned that it is a differential WMOKE image. It means that the black region is the position of the domain before the first current pulse, while the white region corresponds to the domain after the last current pulse. The differential image has been taken using a current pulse of $J \approx 5.7 \times 10^{11} \text{ A m}^{-2}$ with a pulsewidth of 100 ns repeated 250

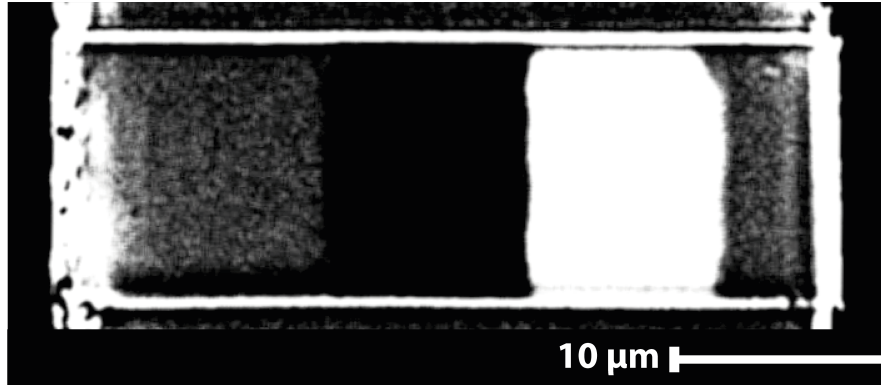


Figure 2.36: Experimental demonstration of the shifting of a domain between the one confinement region to another. It is a widefield magneto-optic Kerr effect differential image, which means that the white region represents the domain after the last current pulse, while the black region represents the position of the domain before the first current pulse. The latter corresponds to the initial configuration, showing that the domain is correctly shifted.

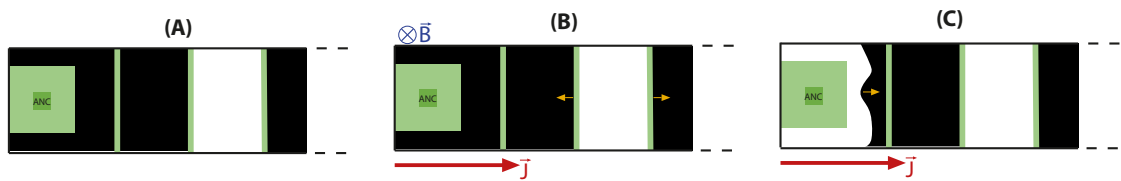


Figure 2.37: Schematic representation of the nucleation of a domain in a ferromagnetic wire with two bit cells. The latter are regions confined by two Ga^+ ion irradiated barriers. (A) shows the initial configuration, in which a domain is confined in a memory cell. In this configuration a current pulse, together with a magnetic field offset, nucleates a domain wall (B) in the left-hand side of the wire thanks to an artificial nucleation center. The domain wall is then moved towards the first barrier due to the magnetic field offset (C).

times.

In this case the optimized nucleation method, in presence of an ANC, has been used (see Section 2.3.2). This plays a fundamental role in creating a domain, avoiding the shifting of the domain from one confinement region to the other during the nucleation. From an application point of view, it is important to write an information (nucleate a domain) without destroying the already present ones (already shifted domains). This process results stable due to the presence of the field offset. The concept can be explained by considering a positive domain in the first confined region (which corresponds to the black domain in the region between the first two barriers of Figure 2.37(A)), called memory cell from now on. To create

another negative domain (white domain in the figure) a negative magnetic field offset is needed during the nucleation current pulse injection. The negative field offset tries to shrink the positive domains (black), as shown in Figure 2.37 (B), but since the presence of the barrier it cannot happen. In this configuration, when the nucleation current pulse is injected, it will create a domain without moving the one already present. This sets a minimum required value of the irradiation dose of the barriers, because each barrier should be able to keep the domain walls inside it. A lower current pulse can be used to move the domain wall towards the barrier, in order to reach a stable configuration (see Figure 2.37(C)). A higher current density pulse can shift the already present domain, while shifting at the same time the created domain.

2.7 Conclusions and future prospects

To summarize, it has been shown the different technology and characterization tasks to be fulfilled in order to achieve a preliminary domain motion-based device implementation level. They consist of: i) finding a stable and reliable way to efficiently nucleate a domain into a specific region of a ferromagnetic wire. This can be achieved by means of Focus Ion Beam irradiation of artificial nucleation centers (ANC in short). They are localized areas where the material parameters, such as K_u and M_S , are degraded, leading to a lower energy required for the magnetization reversal. This defines a control over the nucleation position. Defined the ANC, an efficient way to nucleate a domain involves the injection of a current pulse in presence of a field offset. The combination of the field-induced and current-induced torques enables a nucleation process characterized by low current densities, reducing the risk of the ferromagnetic wire damaging due to thermal Joule effects; ii) characterization of the domain motion, in which the dependence of the domain velocity with respect to the current density is discussed, showing velocity values from 3 m/s to 5 m/s for high current densities; iii) finding a way to control the spacing between consecutive domain walls, allowing at the same time a regular motion of domains, in which information are encoded. In this work an approach based on FIB irradiated barriers is discussed. Experimentally, it has been observed that ion irradiation, due to induced degradation of K_u and M_S , decreases the total energy, which means that the irradiated barriers are energy wells. A study over the probability of a domain wall to cross such barriers, as a function of the ion dose, is performed showing that domain walls are able to overcome barrier thanks to field or current-induced DW motion. The study of the controlled domain motion through irradiation barriers ends by a demonstration of a memory bit cell consisting of domain confined between two irradiation barriers. It can be shifted to the successive confinement region by a current pulse.

It has to be considered that, the related work has been performed with common CMOS technology processes, such as sputtering, optical lithography, evaporation and Focus Ion Beam technologies, meaning that the building of domain motion-based devices does not require unusual fabrication technologies, leading also to a low-cost technology.

In spite of the different tasks covered, the study still could be extended by addressing different issues related to the simulative and experimental understanding of the domain motion. In simulations, it has been found that increasing the DMI constant, besides the increasing of the velocity, the domain walls are tilted during their motion, as shown in Figure 2.9. The tilting of the domain walls have been observed also experimentally (see Figure 2.24). Understanding the correlation between the tilting angle, the current density and the DMI, could then provide a simple tool to measure the DMI strength in the thin-film stack under test. The characterization of the DMI is not an easy task, and usually it is performed by using in-plane magnetic fields Diez et al. to move a domain wall. However, the tilting stud could reveal a new current-based DMI measuring technique.

Another aspect to be explored is the dependence of the domain velocity with respect to the width of the wire. One could think that narrower wires could show higher domain wall velocities due to the presence of a less number of pinning sites, or also due to the lower energy due to a less number of atomic spins that are tilted. However, it has to be considered also that the increasing of the current density gives raise to heating due to Joule effect, especially if the thin-film geometry presents fabrication inhomogeneities that could locally concentrate the amount of current. Moreover, changing the width of the wire means altering magnetic properties, such as the stray field, changing the configuration of the domain wall[9]. Furthermore, the velocity could be improved by using high spin-orbit coupling materials [26], such as W, below the CoFeB/MgO bi-layer. A tungsten seed layer could be used to enhance the spin Hall effect current, which has been demonstrated to have higher efficiency to the motion of magnetic textures [7]. Ultimately, the domain velocity can be improved by decreasing the number of pinning sites into the thin-film stack. As shown in Figures 2.25 and 2.26, where the velocity dependence on the current density with and without considering the pinning events, one can notice that there are differences on the two trend, meaning that the domain motion is sensitively affected by defects on the ferromagnetic material.

A further study could be performed on the influence of the magnetic field with respect to the current-induced nucleation of a domain. In the nucleation study, it has been shown that using a single current pulse to nucleate a domain from an artificial nucleation center would require a large amount of current density, which could be higher than the threshold current to ignite the Joule effect. An efficient way to nucleate is to couple a current pulse together with a perpendicular magnetic field offset. The values of the latter are low (≈ 0.7 mT), since the aim of

the offset is to add a torque contribution to the current-induced torque. It means that in a real device it can be realized by coil on chip than can be fabricated with the same fabrication process used for the deposition of the metal contacts. Moreover, it has to be mentioned the possibility of the magnetic field-induced nucleation. The switching field of the ferromagnetic wires used for the domain wall motion is around 10 mT. This value can be reached with a coil-on-chip, however it has to be considered that the magnetic field pulses should be in the micro or even nanoseconds range, because higher pulsewidth, at amplitudes higher than 1 mT, will cause a nucleation of a domain with a fast expansion, leading to the annihilation of the nucleated domain or even leading to the complete switching of the wire.

Lastly, the domain shifting through different confinement regions are demonstrated, however it has been done only at a preliminary level by merging the results of the nucleation and barrier experiments. This means that a deeper characterization helps to discover the potentiality of the information transfer due to domain shifting, setting the basics for the implementation of a memory bit cell, building block of racetrack memories [15], which is represented by an information encoded into a magnetization of a domain confined between two barriers.

3 Influence of Ga-ion irradiation on skyrmion size and dynamics

In the 1980s, devices exploiting magnetic bubbles have been proposed as promising nonvolatile storage technology. However, the improvements in Hard Disk Drives and other storage technologies caused the failure of bubble technology. Recently, the studies on magnetic skyrmions, particle-like magnetic textures, showed that magnetic skyrmion-based memory technologies can offer higher storage density and the potentiality of the logic-in-memory. This because of the small size of a magnetic skyrmion, which can be reduced down to several nanometers, and the low current density needed to move such magnetic textures. Moreover, skyrmions can be stabilized by the geometry of the system, adding another degree of freedom on the improvement of the robustness of the related technologies [7].

In this chapter a brief discussion over the physical fundamentals related to magnetic skyrmions is presented. Two important properties for implementing skyrmion-based technology are then studied: the skyrmion size dependence on the material properties and the current-induced skyrmion motion. Both studies are composed by a simulative and an experimental part. The latter has been carried out on W/CoFeB/MgO/Ta magnetic stack depicted in Figure 3.1.

3.1 Basic Principles

After theoretical calculations on chiral magnetic textures and after the study on surface-induced interactions, such as the Dzyaloshinskii-Moriya interaction, it has been demonstrated the existence of magnetic skyrmions.

Skyrmions are particle-like magnetic textures, composed by a core and a tail, which have opposite magnetizations one respect to the other. In between, the magnetization whirls to complete the transition between the core and the tail. Depending on how the magnetization rotates, two types of skyrmions can be defined: Bloch and Néel-skyrmions 3.2. In Bloch-skyrmions the magnetic moments rotate in the tangential plane, so perpendicularly to the radial direction; in Néel-skyrmions the magnetic moments rotate in the radial plane from the core to the tail

[2]. Typically, the latter ones are found in thin-films because they are supported by interfacial DMI, while Bloch-skyrmions are found in B-20-type bulk materials by bulk DMI[7].

3.1.1 Topology of magnetic textures

In spin textures, such as skyrmions, the topology of the magnetization plays a fundamental role on their behavior. Even though the existence of such whirling spin textures has been demonstrated in bulk materials, the attention of the research is on 2D thin-films because they are better understood and preferred for spintronic applications[7][27]. The topological characteristics of the skyrmions can be described by the *topological charge*. Defining the topological charge density $\rho(\mathbf{r})$ as

$$\rho(\mathbf{r}) = \frac{1}{4\pi} \mathbf{m}(\mathbf{r}) \cdot (\partial_x \mathbf{m}(\mathbf{r}) \times \partial_y \mathbf{m}(\mathbf{r})) \quad (3.1)$$

where $\mathbf{m}(\mathbf{r})$ is the reduced local magnetization. The topological charge, referred also as *Pontryagin number*, can be derived as

$$Q = \frac{1}{4\pi} \int \mathbf{m}(\mathbf{r}) \cdot (\partial_x \mathbf{m}(\mathbf{r}) \times \partial_y \mathbf{m}(\mathbf{r})) \cdot d^2 \mathbf{r} = \int \rho(\mathbf{r}) d^2 \mathbf{r} \quad (3.2)$$

Q counts how many times the magnetization wraps on a 2D surface of a 3D sphere[27]. Depending on its value, the topological charge defines different type of magnetic textures, such as skyrmioniums ($Q = 0$), magnetic vortexes ($Q = -0.5$) or merons ($Q = -0.5$). In case of skyrmions $Q = -1$ for both Néel and Bloch configurations, and it takes the name of *skyrmion number* Q_s [7][27]. However,

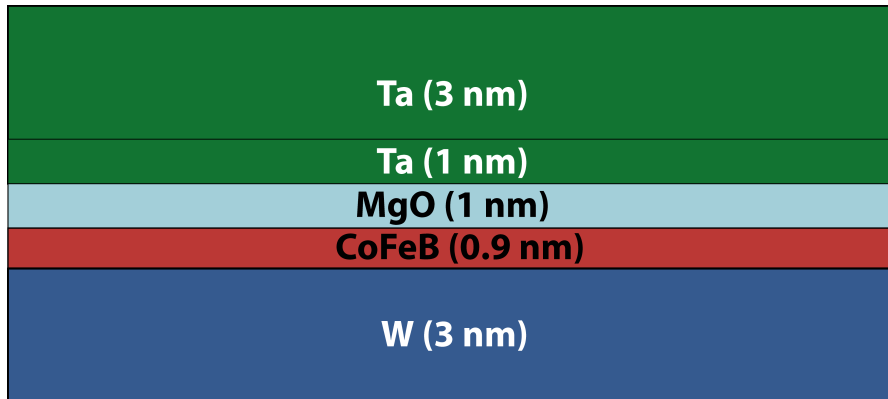
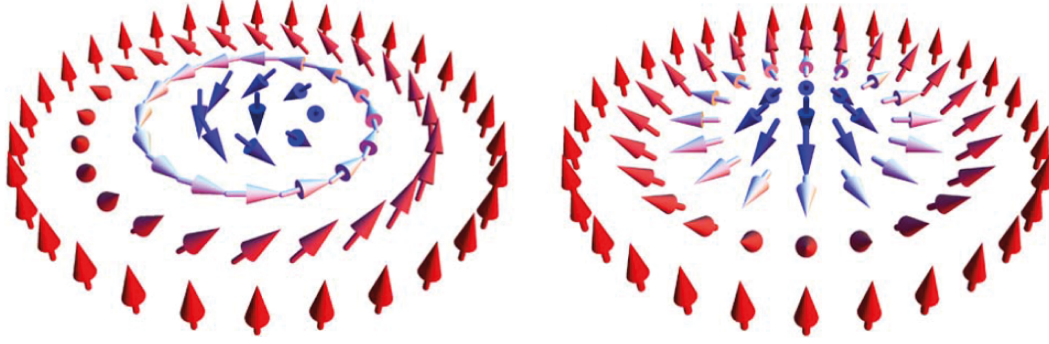


Figure 3.1: Magnetic stack used for skyrmion study. The CoFeB/MgO bilayer, which gives rise to PMA, is sandwiched between W and Ta thin-films, used as seed/adhesion and as capping layer, respectively.



(a) Bloch skyrmion.

(b) Néel skyrmion.

Figure 3.2: Illustration of two types of magnetic skyrmions[7].

the Néel and Bloch configurations cannot be distinguished only from the skyrmion number. In general, to identify different whirling magnetic textures a more complete description is needed exploiting other topological charges, described below.

Chiral spin texture are uniquely defined by three topological numbers:

$$(Q_s, Q_v, Q_h)$$

where Q_s is the mentioned skyrmion number, Q_v and Q_h are called *vorticity number* and the *helicity number*, respectively. In order to understand the meaning of these three quantities, considering a spherical coordinate system, the local magnetization, as a function of the out-of-plane (OOP) angle θ and the in-plane (IP) angle ϕ , is expressed as:

$$\mathbf{m}(\theta, \phi) = (\sin\theta\cos\phi, \sin\theta\sin\phi, \cos\theta) \quad (3.3)$$

One can notice that the OOP angle θ rotates from 0 to π , while ϕ rotates from 0 to 2π . Considering this coordinate system, the vorticity number can be defined as:

$$Q_v = \frac{1}{2\pi} \oint_C d\phi = \frac{1}{2\pi} [\phi]_{\phi=0}^{\phi=2\pi} \quad (3.4)$$

Considering a parametrization of the x-y space:

$$x = r\cos\varphi, y = r\sin\varphi \quad (3.5)$$

the evolution of the in-plane angle can be defined as:

$$\phi = Q_v\varphi + Q_h \quad (3.6)$$

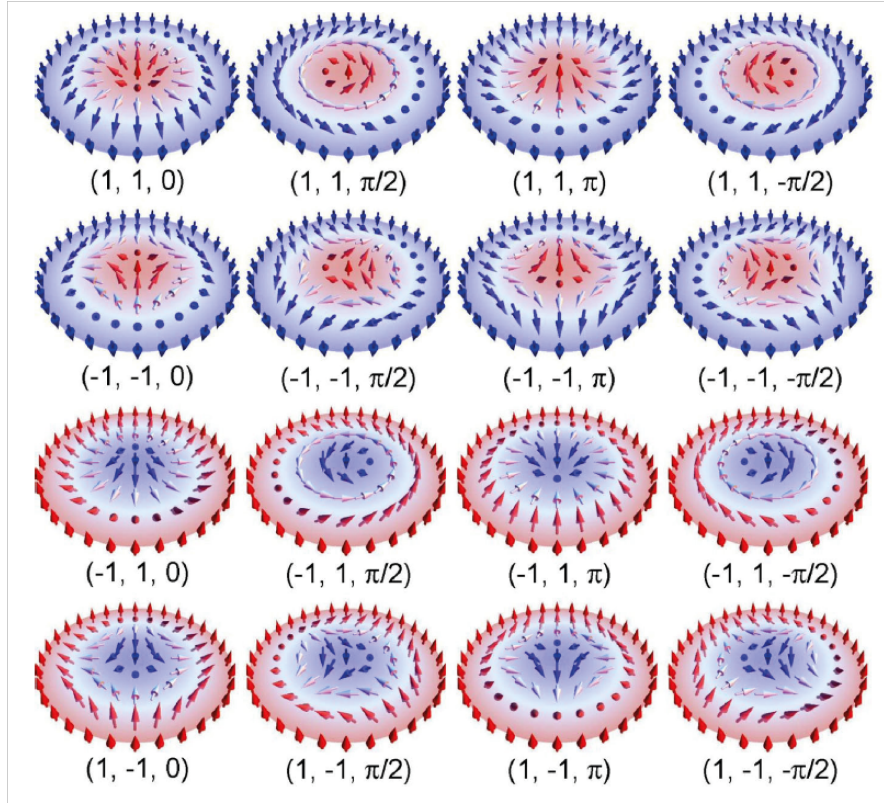


Figure 3.3: 2D illustrations of magnetic skyrmions with different topological numbers [27].

where the helicity number can be introduced as a phase term.

Therefore, the local magnetization can be rewritten as [27]:

$$\mathbf{m}(\theta, \phi) = [\sin\theta\cos(Q_v\varphi + Q_h), \sin\theta\sin(Q_v\varphi + Q_h), \cos\theta] \quad (3.7)$$

The different magnetic textures as a function of the topological numbers are shown in Figure 3.3. Between the illustrations, the Néel skyrmions can be recognized having $Q_h = 0$ or $Q_h = \pi$ while Bloch skyrmions can be recognized having $Q_h = \pi/2$ or $Q_h = 3\pi/2$. In both cases $Q_s = -1$, $Q_v = -1$. In function of the topological charge, the *anti-skyrmions* can be recognized by considering $Q_s = 1$. They are considered the anti-particles of skyrmions.

3.1.2 Dynamics of magnetic skyrmions

The motion of magnetic skyrmions can be achieved by injecting a current into a ferromagnetic wire. The motion can be due to the spin transfer torque (STT) or due to the spin Hall effect (SHE) [7]. In the first case the current is injected

directly into the ferromagnetic wire hosting the skyrmions, while in the second case the current is injected into a heavy metal layer (HM in short), like W or Pt, under (or above) the wire. The injected current will be split depending on the spin of the electrons, which are pushed towards the ferromagnetic layer, injecting a vertical spin-polarized current into the wire. The two mechanisms are depicted in Figure 1.4.

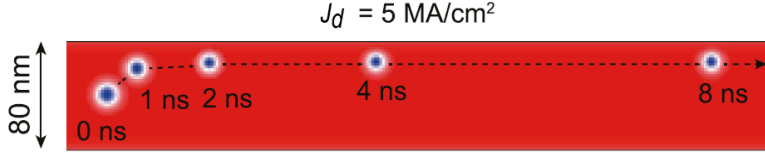


Figure 3.4: Trajectory of a skyrmion driven by a vertical spin-polarized current in a nanotrack [7].

In literature [7][27], it has been shown that the trajectory of the skyrmion during its motion is not straight. Figure 3.4 shows the typical motion of a skyrmion. At the beginning, the skyrmion moves with a velocity which has both longitudinal and transverse components. As soon as the skyrmion reaches the edges, it moves straight due to repulsive forces that the magnetization at the edges exerts on the skyrmion. The force that deviate the trajectory from a straight line is called *Magnus force*. It has to be mentioned that repulsive forces acting on skyrmions, besides the interaction with the edge of the nanotrack, can be induced by the presence of another skyrmion. It is an important aspect to be considered when studying the storage density of a memory device in which the information is encoded into the presence of a skyrmion.

The skyrmion dynamics is governed by the *Thiele equation*:

$$\mathbf{G} \times \mathbf{v}_s - \alpha \mathcal{D} \cdot \mathbf{v}_s + 4\pi \mathcal{B} - \mathbf{J}_{\text{SHE}} + \nabla \mathbf{V}(\mathbf{r}) = 0 \quad (3.8)$$

where \mathbf{G} is called *gyromagnetic coupling vector* and its expression is:

$$\mathbf{G} = (0, 0, 4\pi Q_s) \quad (3.9)$$

The first term in 3.8 describes the Magnus force. The term containing α , the damping constant, is related to the dissipative force, where \mathcal{D} is the dissipative force tensor. \mathcal{B} is the tensor linked to the STT effect, being the third term associated to the STT phenomenon. The fourth term sums up the repulsive forces $\nabla \mathbf{V}(\mathbf{r})$ acting on the skyrmion during the motion. It has to be mentioned that equation 3.8 is valid only for the SHE current case, related to a current injected into an HM adjacent to the ferromagnetic layer (this configuration is called current-perpendicular-to-plane CPP configuration). In case of a STT current, which is a

current-in-plane (CIP) configuration, the Thiele equation takes the form of equation 3.10.

$$\mathbf{G} \times (\mathbf{v}_s - \mathbf{v}_c) + \mathcal{D}(\beta \mathbf{v}_c - \alpha \mathbf{v}_s) + \nabla \mathbf{V}(\mathbf{r}) = 0 \quad (3.10)$$

In this case the (\mathbf{v}_c) describes the velocity of the conduction electrons, proportional to \mathbf{J}_{STT} , which expression is:

$$\mathbf{v}_c = \frac{pa^3}{2eM_S} \mathbf{J}_{\text{STT}} \quad (3.11)$$

where p is the spin polarization of the current e the elementary charge and β the nonadiabatic torque coefficient [7]. As shown by Kang et al. in their work [7], the SHE current shows higher efficiency. This derives from the higher spin polarization efficiency compared to the STT case. Therefore, in general, SHE current is preferable in the prospective of low-power electronic designs of skyrmion-based integrated circuits.

Considering the described fundamental physics, in this work a study of the skyrmion size and dynamics on the W/CoFeB/MgO/Ta ferromagnetic thin-film stack is presented. These two aspects are found to be strongly affected by the material parameters, such as magnetic anisotropy and saturation magnetization. Below, the characterization of the skyrmion size as a function of material parameters is discussed.

3.2 Tailoring the skyrmion size by FIB irradiation

One of the advantages of using skyrmions is the small size that characterize them. Knowing the skyrmion size, together with the repulsion distance of two skyrmions, gives a measure about the information density that can be stored in skyrmion-based storage devices, where a single bit is encoded into the presence of a skyrmion[28] and where requirements such as small bit sizes, long term thermal stability and stability in zero or low applied field have to be met[29]. In this section, in order to address the small bit size requirement, we explore the dependence of the skyrmion size with respect to the crystalline anisotropy constant and the saturation magnetization, which are two parameters that mostly change with irradiation or thermal annealing and that sensitively affect the skyrmion size. The study consists of a simulative part, in which the skyrmion dimension is analyzed within the zero-field skyrmion state, characterized by a small range of K_u and M_S values, where the skyrmion results stable. However, this state is accessed by common ferromagnetic materials [29]. Therefore, a study over a larger set of K_u and M_S values is performed showing different ferromagnetic states.

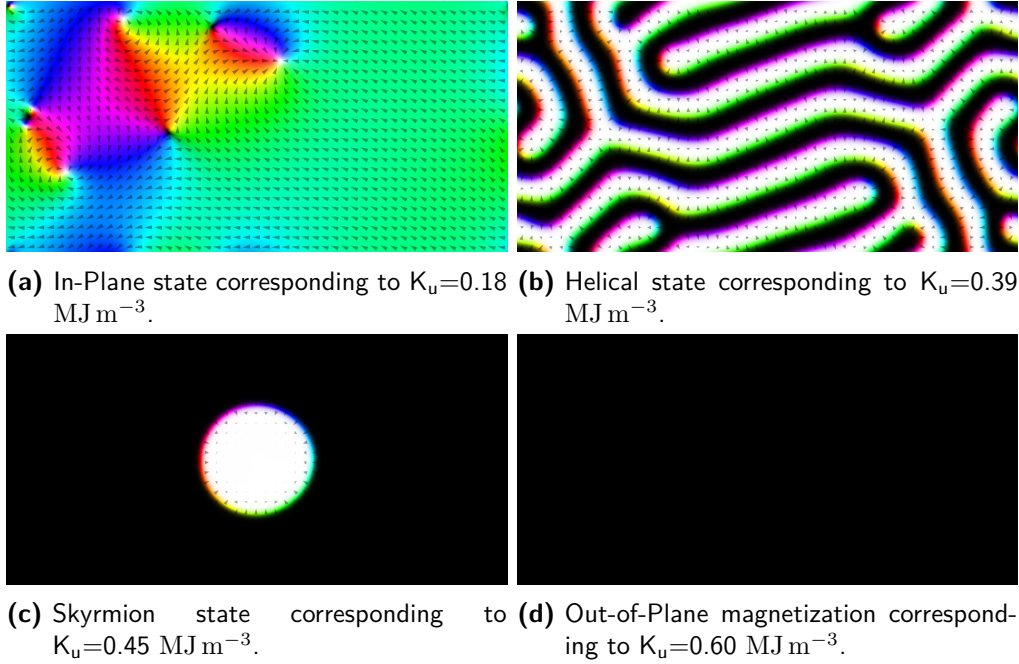


Figure 3.5: Evolution of the magnetization texture at $K_u=0.75$ MA/m for different uniaxial anisotropy values. In all the simulations, the simulation domain is 2048×1024 nm^2 .

The simulative skyrmion size results are then compared with the experimental ones, analyzed on W/CoFeB/MgO/Ta ferromagnetic stack, depicted in Figure 2.1.

3.2.1 Magnetic states in W/CoFeB/MgO/Ta

As discussed in Section 2.4 the FIB irradiation degrades the material properties of the thin-film [19]. It has been observed that for low irradiation doses, the average domain size increases, due to the increasing of the effective magnetic anisotropy. However, as shown by Zhao et al. in their work [30] this trend is not matched in case of a tungsten seed layer. This can be related to the different values of K_u and M_S .

In order to understand the behavior of the W/CoFeB/MgO ferromagnetic stack, in this section an exploration of the magnetic textures observed at different K_u and M_S values is presented, using micromagnetic simulations. The investigation starts from K_u and M_S values for which a skyrmion results stable. This choice is justified by considering that the presence of magnetic skyrmions has been observed experimentally in the ferromagnetic stack under test.

The micromagnetic simulations involve the initialization of a skyrmion with a diameter of 800 nm^2 into a $2048 \times 1024 \text{ nm}^2$ wire. Then, the system relaxes, reaching

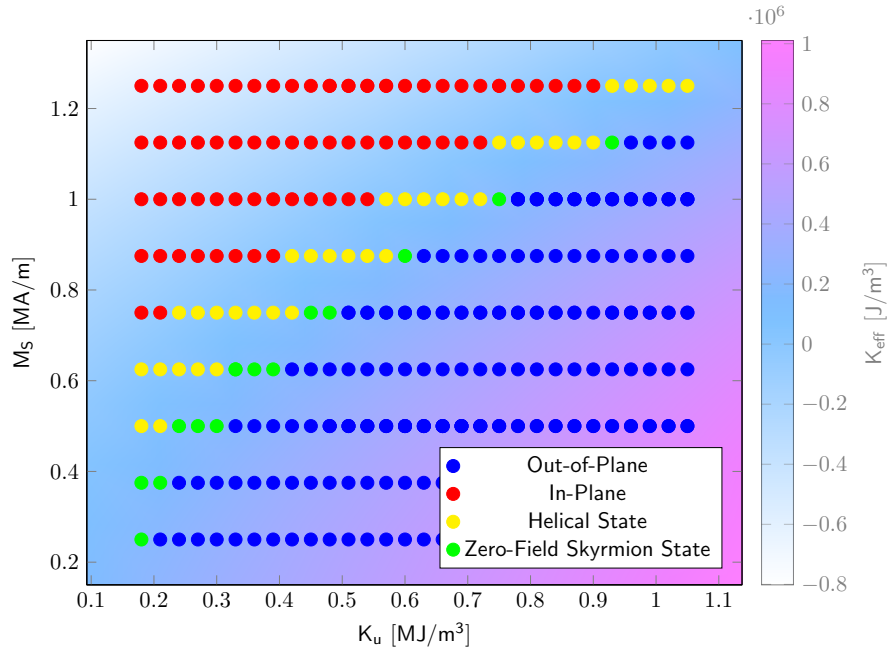
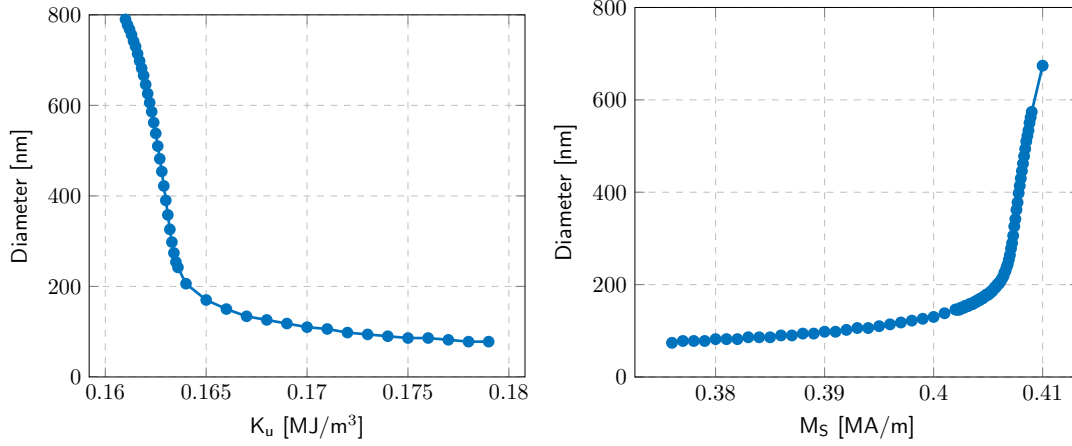


Figure 3.6: K_u - M_S diagram for $D = 1.5 \text{ mJ/m}^2$. In the background, the colormap shows the evolution of $K_{\text{eff}} = K_u - \frac{1}{2}\mu_0 M_S^2$. The colors of the points of the scatter plot indicates the type of magnetic textures at equilibrium, which are also shown in Figure 3.5.

its stable configuration. Depending on the material parameters, the magnetization enters into different ferromagnetic states, which are described below.

- **In-Plane Magnetization.** The skyrmion is not stable and the system is out-of-plane demagnetized.
- **Helical State.** The skyrmion is not stable and the system is out-of-plane magnetized. In this state the domain size is very low and the magnetic moments of the magnet are arranged in helical patterns.
- **Zero-Field Skyrmion State.** In this state the skyrmion is stable and slightly changes in K_u or M_S will change skyrmion dimension.
- **Out-of-Plane Magnetization.** The skyrmion is not stable and the system is out-of-plane demagnetized.

An example of evolution of the magnetization across all the mentioned states is shown in Figure 3.5. In this case the M_S is fixed, while K_u changes. A more complete study is depicted in Figure 3.6. As can be seen, the out-of-plane (OOP)



(a) Diameter evolution as function of K_u at $M_S = 0.375$ MA/m. (b) Diameter evolution as function of M_S at $K_u = 0.18$ J/m³.

Figure 3.7: Simulation results of the evolution of the skyrmion diameter for different M_S and K_u values.

state is characterized by high values of K_u and low values of M_S . This result is expected because taking into account the effective anisotropy constant expression

$$K_{eff} = K_u - \frac{1}{2}\mu_0 M_s^2 \quad (3.12)$$

where for $K_{eff} < 0$ the magnetization results in-plane, while for $K_{eff} > 0$ the ferromagnetic material becomes out-of-plane magnetized (see Section 1.2.1). Moreover, since the dependence of K_{eff} with respect to M_S is quadratic, a slight variation of the saturation magnetization has more influence with respect to K_u . This means that, in order to have out-of-plane magnetization, the crystalline anisotropy contribution has to be higher than the saturation magnetization one. It can happen only if the value of M_S is not too high.

The in-plane (IP) magnetization, red dots in Figure 3.6, represents the opposite configuration with respect to the one mentioned above. In this case the contribution of the quadratic term is higher and K_{eff} results negative. In between the OOP and the IP states, the helical and the zero-field skyrmion state can be found.

In the helical state the sample results out-of-plane magnetized, however it is characterized by a small domain size. Considering the spin moments along a line perpendicular to the domain walls, one can notice that the spins are arranged in regular helices. This state is relevant also because the relative orientation of spin moments between magnetic planes affects the flow of electric current [31]. Moreover, in this configuration, the skyrmion state can be accessed by means of an applied magnetic field.

Layer	Material	Power [W]	Pressure [$\times 10^{-7}$ mbar]	Time [s]	Thickness [nm]
Seed	W	40	4	130.4	3
Magnetic	CoFeB	40	4	32.2	0.9
Oxide	MgO	40	1	150.0	1
Capping	Ta	40	4	21.9	1
Protection	Ta	40	4	65.6	3

Table 3.1: W₃/CoFeB_{1.1}/MgO₂/Ta₄ sputtering parameters.

Following the trend in Figure 3.6, for slightly higher values of K_{eff} with respect to the helical state the skyrmion state is found. In this case the skyrmions are stable without an external magnetic field. Unfortunately, as shown by Büttner, Lemesh, and Beach in Figure 3.6[29], the skyrmion state is out of most of the common material parameter ranges reported in the literature, which instead can be found in the helical state. Moreover, even though the zero field skyrmion state seems to be accessible, it is impossible to have skyrmions below 10 nm, required to exploit the advantage of the skyrmion small size, because the low M_S -high K_u range is inaccessible in common ferromagnets.

Lastly, the skyrmion size is analyzed in the zero-field skyrmion state. The results of the simulations are shown in Figure 3.7. As can be seen, the diameter of the skyrmion increases with respect to M_S , while it decreases with respect to K_u . This is a result reported in literature [32], which is confirmed also in this work.

3.2.2 Skyrmion stack fabrication

Before showing the experimental results on the skyrmion dimension, a brief discussion about the fabrication of the skyrmion stack depicted in Figure 3.1 is presented. The fabrication process is composed by the same fabrication steps performed for the Ta/CoFeB/MgO/Ta stack (see Section 2.3.1). Below, only the differences in the fabrication process are discussed.

The production of the W/CoFeB/MgO/Ta stack starts from the deposition of the different thin-films. In Table 3.1 the sputtering parameters are shown. In Figure 3.1 the presence of two capping layers, made of the same material, can be noticed. The deposition of the second capping layer, called protection layer, is done after thermal annealing. The reason for this choice can be explained by looking at the hysteresis loop evolution in respect to the annealing time (see Figure 3.8). The sample without the protection layer is subjected to different annealing steps. After 5 minutes at 275 °C, in a controlled atmosphere, the sample develops PMA. To reach a skyrmion state, the sample should be degraded. The correct material

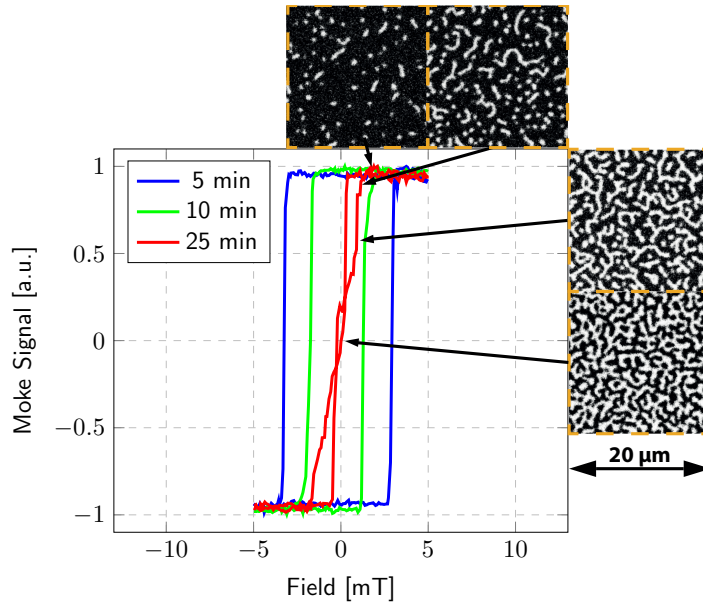


Figure 3.8: Hysteresis loops as a function of the thermal annealing time, measured with the laser magneto-optic Kerr effect technique. The annealing temperature is kept at 275 °C in controlled N₂ atmosphere in all the different steps. The image shows decreasing of the switching field after each thermal annealing. After the first step, which is the one to give raise to the PMA, the coercivity is around 3 mT, after 10 minutes it is around 1.5 mT, to then reaching the zero-remanence state, where the sample gets demagnetized at 0 mT. From the latter case, a slight increasing of magnetic field makes the skyrmions appearing. The evolution of the sample magnetic texture is shown in the widefield magneto-optic Kerr effect images.

state to stabilize skyrmions in the stack is reached after 25 minutes in the same annealing conditions. The degradation is possible thanks to the thin Ta capping layer. Experimentally, it has been shown that with a thicker capping layer, the degradation of the material parameters is lower and the skyrmion state cannot be reached.

The protection layer is deposited once the mentioned state is achieved. This layer plays a fundamental role in the further processing of the sample. It was noticed that the sample without the protection layer results to be very sensible to the successive fabrication processes, such as wet chemistry and ion beam etching, leading to the damaging of the magnetic properties. For this reason, after the tailoring of the magnetic properties by means of thermal annealing, onto the sample a further Ta protection layer is deposited with a sputtering process.

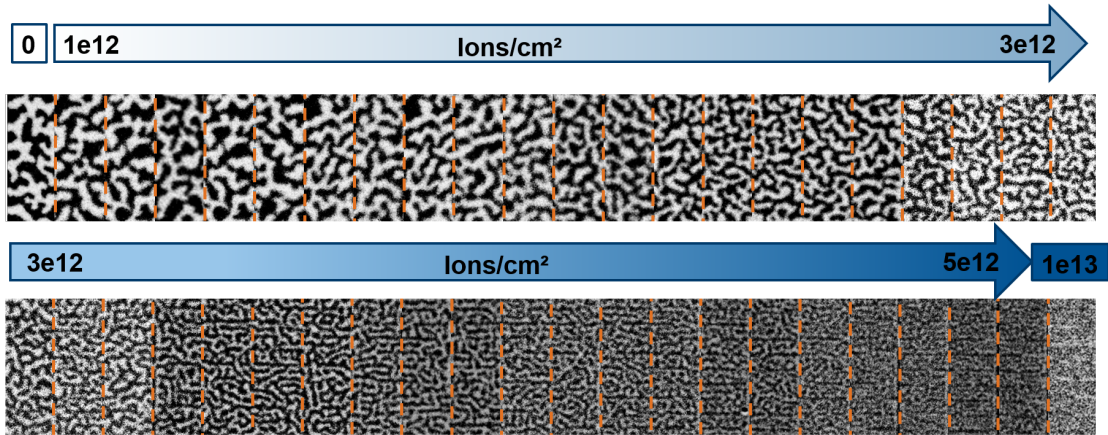


Figure 3.9: Widefield magneto-optic Kerr effect images of the evolution of the magnetization in the W/CoFeB/MgO/Ta stack sample for different irradiation doses at zero magnetic field.

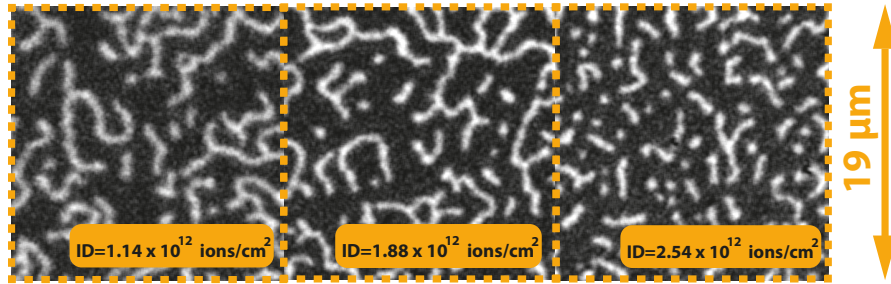


Figure 3.10: Widefield magneto-optic Kerr effect images of the evolution of the magnetization in the W/CoFeB/MgO/Ta stack sample for different irradiation doses at a magnetic field of 0.64 mT.

3.2.3 Skyrmion dimension experiment

The first experiment towards the understanding of the skyrmion behavior into W/CoFeB/MgO/Ta stack is the study of the skyrmion dimension as a function of the material parameters, as done in the simulative part. Experimentally, the tailoring of the material parameters can be performed by means of Focus Ion Beam irradiation. The experiment consists of the irradiation of $19 \times 19 \mu\text{m}^2$ squares at different irradiation dose. Images of the different squares at different magnetic field values are taken and analyzed. The result of the FIB irradiation is shown in Figure 3.9, where WMOKE images of domains in the demagnetized state are shown. Increasing the irradiation dose, the domains get smaller, as seen in Section 2.4.1 for the Ta/CoFeB/MgO/Ta stack. However, in this case, for low irradiation doses, the average domain size does not increase. This can be explained by considered that in

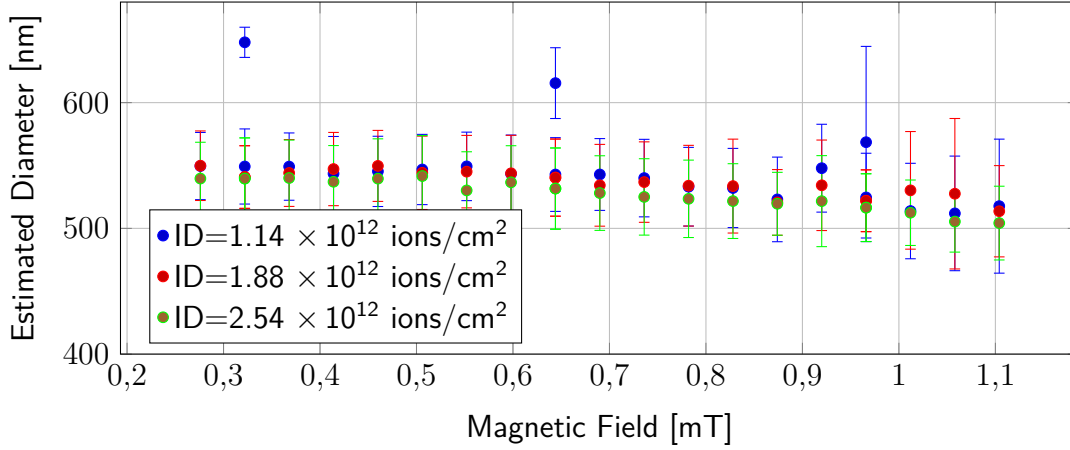


Figure 3.11: Evolution of the measured skyrmion diameter with respect to the applied magnetic field at different Ga⁺ ion doses (ID in short). For the ID = 1.14 × 10¹² ions/cm² case, two values of the estimated diameter are shown. They belong to different measurements and are reported for completeness.

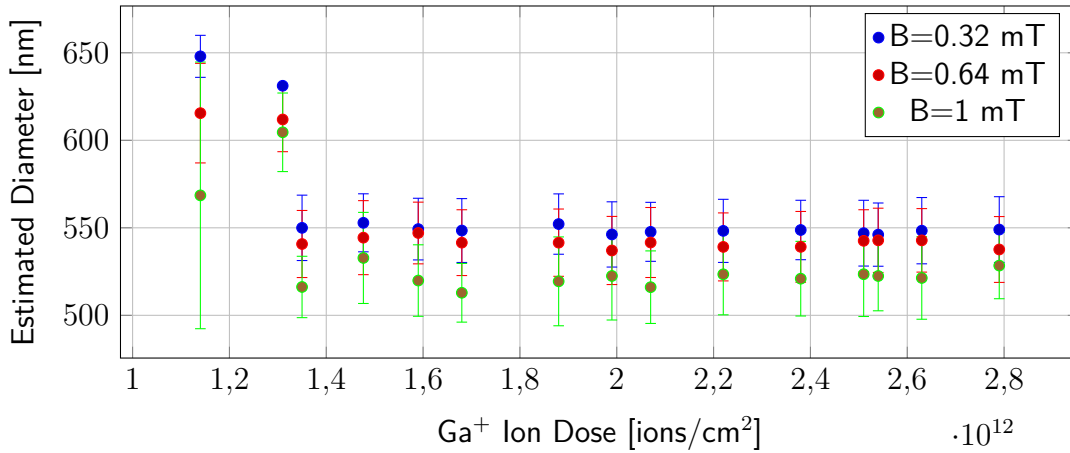


Figure 3.12: Evolution of the measured skyrmion diameter respect to the Ga⁺ ion doses at different applied magnetic field values.

order to observe a skyrmion state, the sample has to be degraded under thermal annealing, bringing the magnetization near the onset of the in-plane condition. This means that the value of K_{eff} is very small ($K_{eff} = 0$ corresponds to the transition to the in-plane condition) and a further degradation of K_u and M_S cannot produce an increase of K_{eff} , as observed for the Ta/CoFeB/MgO/Ta stack.

After a preliminary discussion of the effect of the ion irradiation on the average domain size, the sample is subjected to an applied magnetic field, which shrinks the domains, leading to the formation of skyrmion. The analysis of the skyrmion

dimension is performed by sweeping over different magnetic field values, and at each step an image of the irradiated squares is recorded. The different images are then analyzed by using Trackmate, a tool distributed in Fiji, able to characterize particles in an image.

Firstly, we consider the skyrmion diameter variation with respect to the magnetic field. In Figure 3.11 three different curves for three different ion doses are shown, while in Figure 3.10 an example of measurement frames at 0.64 mT for three different ion doses is shown. Increasing the magnetic field, the skyrmion size gets smaller, even though the estimated diameter values fall into the error range. Moreover, the decreasing trend seems to be more accentuated for lower ion irradiation doses. One possible reason could be related to the fact that the irradiation increases the number of pinning sites [24], obstructing the compression of the skyrmion. For magnetic field values higher than 1.1 mT the skyrmions are annihilated.

The study continues by considering the variation of the diameter with respect to the irradiation dose. As can be noticed from Figure 3.12, there is a decreasing trend of the skyrmion size with respect to the ion dose, which is more accentuated for low ion doses. One possible reason could be that, already for low ion doses, the material parameters, such as K_u and M_S , start to be degraded and, following the trends observed in the simulations (see Figure 3.7), the degradation of M_S seems to affect more the skyrmion diameter.

3.3 Skyrmion Velocity

Compared to domain wall motion, skyrmion motion has been demonstrated to be characterized by lower current densities and by higher velocities [7]. In skyrmion-based devices, in which information are encoded into skyrmions, such as skyrmion-based racetrack memory, the skyrmion dynamics becomes one of the most important phenomena to define the velocity of information processing[7][27].

In this section, the skyrmion velocity is firstly simulated according to the material parameters discussed in Section 3.2.1. The results of the simulations are then compared to experimentally measured skyrmion velocities as a function of the material properties, tailored by means of FIB irradiation.

3.3.1 Skyrmion velocity simulations

The simulations of the skyrmion velocity are composed by different steps. Firstly, a 800 nm wide skyrmion is initialized into the center of a 2048x1024 nm² wire and the system relaxes, achieving the lowest energy configuration. In this step the skyrmion reaches its stable dimension, which changes depending on the material

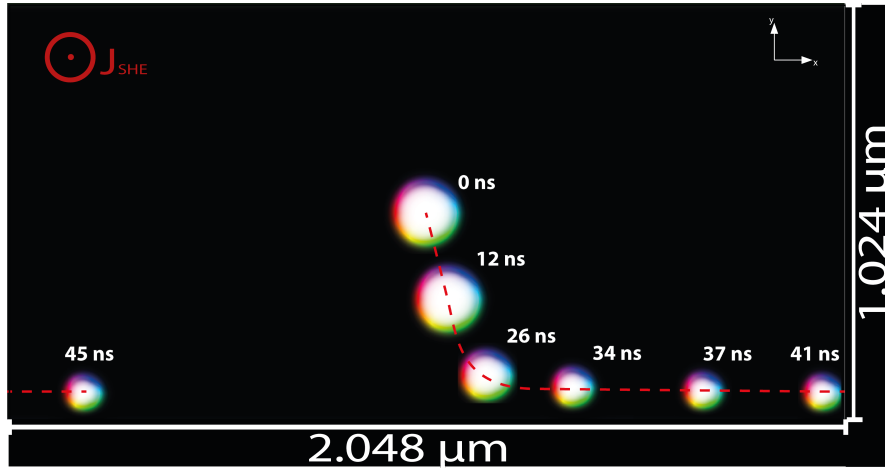


Figure 3.13: Example of skyrmion motion at different time stamps of the simulation. The skyrmion is initialized in the center of the microwire and, after relaxation, a current flows. This image has been realized considering $M_S = 0.404$ MA/m, $K_u = 0.18$ MJ/m³, $D = 1.5$ mJ/m² and $J = 1.5 \times 10^{10}$ A/m².

parameters. Starting from this equilibrium configuration, a vertical spin-polarized current is injected into the microwire, igniting the motion of the skyrmion. At each 0.1 ns the position of the skyrmion is recorded. Periodic boundary conditions are set along the longitudinal direction, meaning that the simulation domain is repeated along this direction, extending the simulation to a longer wire (in this case the simulation domain is repeated two times). The simulation is then repeated for different current steps and for different M_S and K_u values.

In Figure 3.13 an example of the trajectory computed by the skyrmion during its motion is shown. The time 0 ns corresponds to the instant just after the relaxation, while the other skyrmions are superposition of different simulation frames taken at different time steps. As can be seen, the skyrmion initially moves with a certain angle with respect to the x axis, due to the Magnus force. The trajectory is then deviated thanks to the edge repulsive forces. During the initial motion of the skyrmion, before the interaction with the wire edge, the skyrmion velocity and the skyrmion angle are extracted.

The first simulation results involve the dependence of the skyrmion dynamics with respect to the saturation magnetization. The values of M_S are chosen in the range corresponding to the curvature of the d - M_S curve (see Figure 3.7b), where differences between skyrmions of different diameters can be appreciated. The results of the simulations are depicted in Figure 3.14. As shown in Figure 3.14a, the velocity of the skyrmion increases with the injected current density, as expected. Moreover, it also increases with the saturation magnetization, especially at higher current densities. The skyrmion angle (see Figure 3.14b) is found to

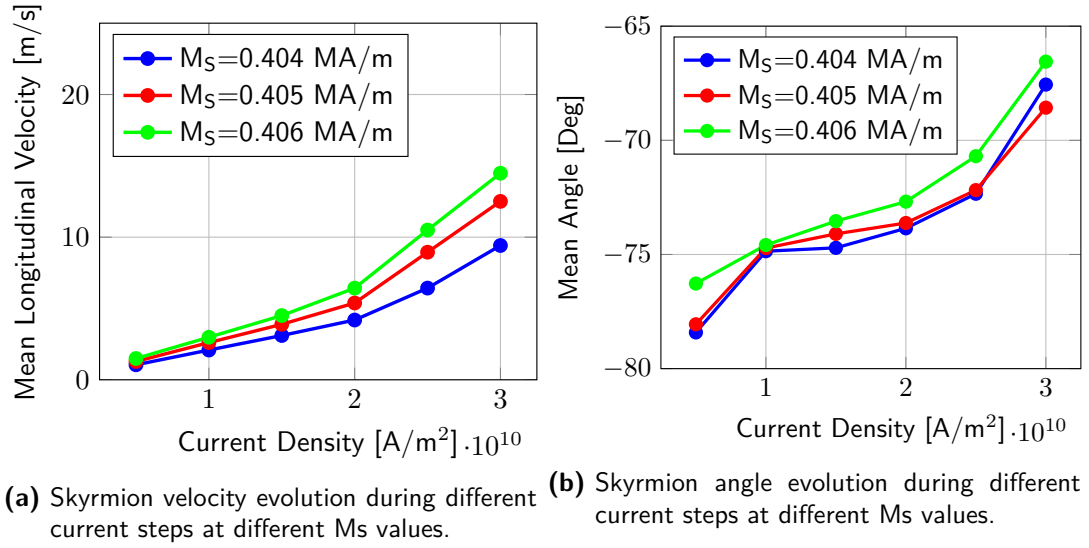


Figure 3.14: Evolution of the skyrmion velocity and skyrmion angle for different current density and M_S values. The simulations have been performed considering $K_u = 0.18$ MJ/ m^3 , $D = 1.5$ mJ/ m^2 , $\alpha = 0.015$ and $\theta_{SH} = 0.15$.

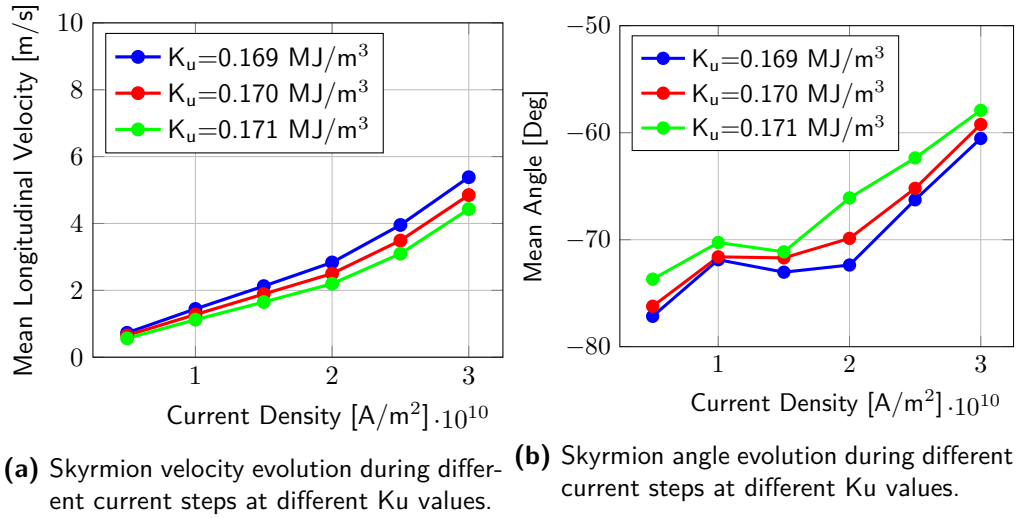


Figure 3.15: Evolution of the skyrmion velocity and skyrmion angle for different current density and K_u values. The simulations have been performed considering $M_S = 0.375$ MA/m, $D = 1.5$ mJ/ m^2 , $\alpha = 0.015$ and $\theta_{SH} = 0.15$.

slightly decrease (notice that it is measured from the direction of motion of the skyrmion to the x axis and since the skyrmion deviates towards the bottom of the track, it is negative) with respect to the increasing of the current density. A

lower skyrmion angle means a more straight motion of the skyrmion, which from an application point of view could be preferable. However, it has to be considered that going towards high current density is detrimental because, besides increasing of the heating due to Joule effect in real systems, the skyrmion is pushed towards the edge of the track. If the current density is enough large, the repulsive force that takes the skyrmion in the track is overcome, leading to the annihilation of the skyrmion [7][27][33]. One can also notice that the skyrmion angle decreases with the increasing of the saturation magnetization.

The second parameter to be analyzed is the uniaxial anisotropy K_u . Also in this case, the values chosen are the ones corresponding to the curvature of the $d-K_u$ curve (see Figure 3.7a). The results of the simulations are shown in Figure 3.15, where both the velocity and the angle evolutions at different current density and K_u steps are shown. As shown by Figure 3.15a one can notice that the velocity of the skyrmion increases with the current as expected, but it also decreases with K_u . The same behavior can be found in the angle evolution (see Figure 3.15b).

By merging the simulation results of the skyrmion motion with the ones related to the simulations of the skyrmion dimension, Figures 3.14 and 3.15 show that bigger skyrmions travel slightly faster with respect to smaller ones.

3.3.2 Skyrmion velocity experiment

The last experiment to be explored is the skyrmion velocity. For this purpose two wires of $25 \times 50 \mu\text{m}^2$ and $35 \times 50 \mu\text{m}^2$ have been patterned using UV lithography and ion beam etching onto W/CoFeB/MgO/Ta magnetic stack. Half of each wire has been irradiated using Ga^+ FIB irradiation, in order to compare the velocities in both the pristine and in the irradiated regions. The ferromagnetic wires are contacted at the horizontal edges by copper wire deposited by means of metal evaporation. The resulting gap between the contacts is $35 \mu\text{m}^2$, which is the portion of the wire in which the current flows. The fabrication process is the same of the one described in Section 3.2.2, while the patterning on the microwires corresponds to the one described in Section 2.3.1.

In order to measure the skyrmion velocity, current pulses of 50 nanoseconds are injected into the wires. The measurement consists of 100 repetition of a train of 4 current pulses. Between each repetition a WMOKE image is recorded. The relative displacement of the skyrmions between successive images is measured using Trackmate, a tool distributed in Fiji, able to characterize the motion of particles in a set of images. The measurement process is then repeated sweeping over different current density values. The results of the experiment are shown in Figure 3.16.

For low current densities (less than $2 \times 10^{11} \text{ A m}^{-2}$) the skyrmion velocity is found to be equal in all the reported cases. As remarked by the black dashed line, this corresponds to the thermal activated motion of the skyrmion and no

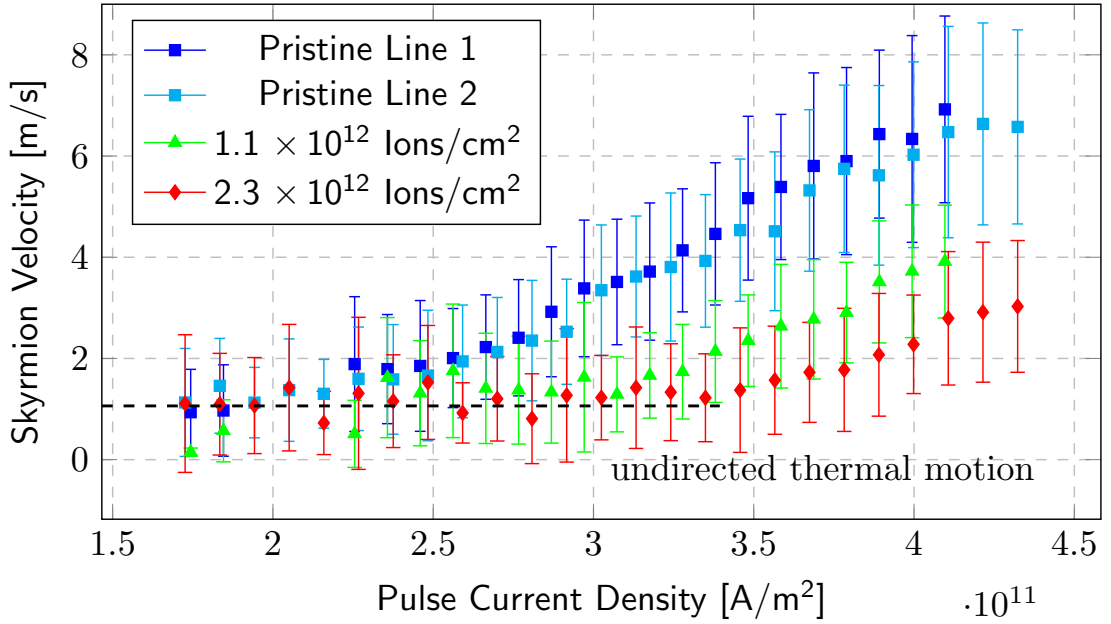


Figure 3.16: Dependence of the skyrmion velocity with respect to the current density, for different irradiation doses. The measurements have been performed by injecting 100 times a train of 4 current pulses with pulsewidth of 50 ns into the ferromagnetic wires. Between each train of current pulses, a widefield magneto-optic Kerr effect images are recorded. Analyzing the images, the displacement of the skyrmions is measured, from which the skyrmion velocity is derived.

real current-induced motion is registered. As soon as the current density increases (more than $2 \times 10^{11} \text{ A m}^{-2}$) the curves start to split, corresponding to the onset of the current-induced skyrmion motion. It has to be noticed that the motion in the irradiated wires starts at higher threshold currents with respect to the motion in the pristine wire. This can be explained by considering that the irradiation increase the number of pinning sites into the ferromagnet [24], leading to an increase of the depinning current density. The higher threshold current needed in the higher irradiation case (red points) with respect to the lower irradiation one (green points) supports this assumption. Moreover, in the work of Herrera Diez et al. [22] it has been observed an increasing of the depinning fields due to irradiation in the case of domain wall motion in the creep regime. A similar behavior is expected in case of skyrmion motion.

Besides the different threshold current densities, important differences can be found in the values of the different trends. The measured skyrmion velocity is higher in case of the pristine portions of the wires, while it decreases in the irradiated regions. Moreover, for the highest irradiation dose, corresponding to 2.3

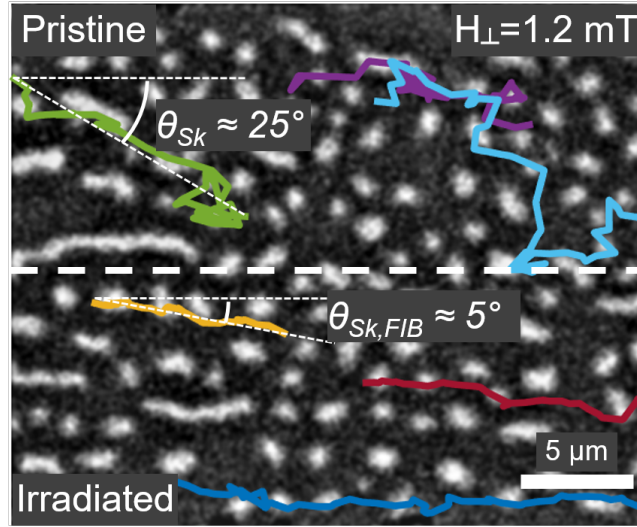


Figure 3.17: Widefield magneto-optical Kerr effect image of a 35 μm wide wire during after skyrmion motion measurement. The white dashed line separates the pristine region from the irradiated one. The colored lines indicate detected skyrmion motion trajectories, which are used for the calculation of the depicted skyrmion angle θ_{Sk} .

$\times 10^{12}$ ions/cm², the lowest values of the skyrmion velocity is observed. One possible reason for this behavior can be related to the presence of pinning sites, which are enhanced upon ion irradiation [24]. A further explanation can be given by considering that the ion irradiation degrades the material properties of the ferromagnetic material, such as K_u and M_S [19][24]. As shown in Section 3.3.1, a variation of these two parameters produces an effect on the velocity and on the angle of the skyrmion motion. In particular, a reduction of K_u produces an increase of the skyrmion velocity and a decrease of the skyrmion angle (see Figure 3.15), while a reduction M_S produces a decrease of the skyrmion velocity, followed by an increase of the skyrmion angle (see Figure 3.14). Considering the simulation results, a possible explanation of the behavior of the skyrmion velocity with respect to the irradiation doses can be related to the higher degradation of M_S with respect to K_u . In particular, by weighting the two contributions and assuming a higher reduction of the saturation magnetization with respect to the anisotropy constant, the net effect of the ion irradiation is the lowering of the skyrmion velocity. Moreover, this assumption is supported by the behavior of the skyrmion angle. In Figure 3.17 a measurement of the skyrmion angle on detected skyrmion motion trajectories is shown. As can be seen, in the irradiated region, the skyrmion angle results to be reduced with respect to the pristine region. Also in this case a higher reduction of M_S with respect to K_u can explain the reduction of the skyrmion

angle.

In summary, the skyrmion velocity experiment shows that using Focus Ion Beam irradiation it is possible to locally change the material parameter of the ferromagnetic stack, which has a direct influence on the skyrmion motion. From an application point of view, the ion irradiation can be used to locally tailor the angle and the velocity of the skyrmion motion.

3.4 Conclusions

In this chapter a characterization of the influence of the Ga⁺ Focus Ion Beam irradiation on the W/CoFeB/MgO/Ta stack is discussed. The study on the ferromagnetic material is divided into two experiments: i) the characterization of the skyrmion size as a function of ion dose and the applied magnetic field and ii) the evaluation of the current-induced skyrmion velocity on pristine and irradiated regions of a patterned microwire.

In the skyrmion size experiment, it has been shown that the skyrmion diameter depends on the irradiation dose. In particular, the study shows that for ion doses higher than 1.35×10^{12} ions/cm² the skyrmion size is decreased down to ≈ 525 nm, and it saturates at this value for higher irradiation doses. In order to explain this behavior, micromagnetic simulations have been performed, in which the skyrmion diameter is analyzed under different values of K_u and M_S . The simulation results show that the skyrmion size increases for a decrease of K_u , while it decreases for a reduction of M_S . Considering that the FIB irradiation induces a degradation of the material parameters [24][19], the experimental trend matches the variation trend of the skyrmion size when M_S is reduced. This leads to the conclusion that, during FIB irradiation, the degradation rate of the saturation magnetization is higher with respect to the anisotropy one.

The second part of this chapter is focused on the dynamics of the skyrmion motion on W/CoFeB/MgO/Ta ferromagnetic stack. The study shows that the FIB irradiation influences the skyrmion velocity. For the experiment two patterned microwires have been used, in which a region, corresponding to half of the wire, is irradiated, in order to understand the effect of the FIB irradiation. The results of the current-driven motion of skyrmion in such wire is shown in Figure 3.16, where different colors are associated to different ion doses. It can be noticed that the FIB irradiation lowers the skyrmion velocity values, and this effect is proportional to the ion dose. As done for the skyrmion size experiment, micromagnetic simulations have been performed in order to support the characterization of the skyrmion dynamics with respect to variation in the material properties. In particular, the simulation results show that the skyrmion velocity is increased for a reduction of K_u , while it is increased when M_S is enhanced. As shown in the skyrmion

size experiment, also in this case the experimental trend matches the skyrmion velocity trend when a reduction of the saturation magnetization is considered. This supports the idea that, upon FIB irradiation, the degradation rate of the saturation magnetization is higher with respect to the anisotropy one.

In summary, in this chapter it has been demonstrated that Focus Ion Beam Irradiation can tailor the dimension and the motion of the skyrmions, by locally changing the material parameters. It has been found that the dominant effects upon ion irradiation are given by a higher degradation of the saturation magnetization with respect to the degradation anisotropy constant.

In spite of the different tasks covered, the study of the size and the dynamics of the skyrmions can be further extended by considering other process and parameter variations. For example, an important interaction that stabilizes magnetic skyrmions is the Dzyaloshinskii-Moriya interaction. The information of the value of the DMI constant D for the W/CoFeB/MgO/Ta magnetic stack used in this work is missing, as well as micromagnetic simulations on the behavior of the size and of the velocity of skyrmions as a function of D .

Another key parameter that from the application point of view cannot be neglected is the skyrmion angle at experimental level. A preliminary attempt for the characterization of this quantity is shown in Figure 3.17, where a difference of the measured skyrmion angle between the pristine and the FIB irradiated region of the wire is depicted. However, the phenomenon needs a deeper study, considering different ion dose irradiation.

Concluding, the achievement of a full characterization of the skyrmion size and dynamics by adding the missing studies allows to set the basis of the skyrmion-based application. In this prospective, such devices are expected to attract the attention of the modern storage industry research.

4 Conclusions

The present work explores the fundamental principles of the current driven motion of domain walls and skyrmions, aiming to the implementation of novel storage devices.

In the first part, the current-induced domain motion is explored, focusing on the different technologies and characterization tasks to be fulfilled in order to achieve a preliminary implementation of a domain motion-based device. In this prospective, the domain motion study is divided in three main steps: i) finding a stable and reliable way to efficiently nucleate a domain into a specific region of a ferromagnetic wire. This can be achieved by means of Focus Ion Beam irradiation of artificial nucleation centers (ANC in short). They are localized areas where the material parameters, such as K_u and M_S , are degraded, leading to a lowered switching field. This defines a control over the nucleation position. Defined the ANC, an efficient way to nucleate a domain involves an injection of a current pulse in presence of a field offset. The combination of the field-induced and current-induced torques enables a nucleation process characterized by low current densities, reducing the risk of damaging of the ferromagnetic wire due to thermal Joule effects; ii) characterization of the domain motion, in which the dependence of the domain velocity with respect to the current density is discussed, showing velocity values from 3 m/s to 5 m/s for high current densities; iii) finding a way to control the spacing between consecutive domain walls, allowing at the same time a regular motion of domains, in which information are encoded. In this work an approach based on FIB irradiated barriers is discussed. Experimentally, it has been observed that ion irradiation, due to the induced degradation of K_u and M_S , decreases the total energy making the barriers to result energy wells. A study over the probability of a domain wall to cross such barriers, as a function of the ion dose is performed, showing that domain walls are able to overcome barrier thanks to field or current-induced DW motion. The study of the controlled domain motion through irradiation barriers ends with a demonstration of a memory bit cell consisting of domain confined between two irradiation barriers. The ferromagnetic material used for domain motion experiments is a Ta/CoFeB/MgO/Ta thin-film stack.

The second part of this thesis involves the characterization of the skyrmion size and skyrmion dynamics, as a function of different Focus Ion Beam irradiation conditions. The study on W/CoFeB/MgO/Ta stack, which is a ferromagnetic material hosting magnetic skyrmions, is divided into two experiments: i) the characterization of the skyrmion size as a function of ion dose and the applied magnetic field and ii) the evaluation of the current-induced skyrmion velocity on pristine and irradiated regions of a patterned microwire.

In the skyrmion size experiment, it has been shown that the skyrmion diameter depends on the irradiation dose. In particular, the study shows that for ion doses higher than 1.35×10^{12} ions/cm² the skyrmion size is decreased down to ≈ 525 nm, and it saturates at this value for higher irradiation doses. In order to explain this behavior, micromagnetic simulations have been performed, in which the skyrmion diameter is analyzed under different values of K_u and M_S . The simulation results show that the skyrmion size increases for a decrease of K_u , while it decreases for a reduction of M_S . Considering that the FIB irradiation induces a degradation of the material parameters [24][19], the experimental trend matches the variation trend of the skyrmion size when a reduction of M_S . This leads to the assumption that, during ion irradiation, the degradation rate of the saturation magnetization is higher with respect to the anisotropy one.

The study on W/CoFeB/MgO/Ta stack continues by the characterization of the dynamics of the skyrmion motion. The study shows that the FIB irradiation influences the skyrmion velocity. For the experiment two patterned microwires have been used, in which a region, corresponding to half of the wire, is irradiated, in order to understand the effect of the FIB irradiation. The results of the current-driven motion of skyrmion in such wire is shown in Figure 3.16, where the different colors are associated to different ion doses. It can be noticed that the FIB irradiation lowers the skyrmion velocity values, and this effect is proportional to the ion dose. As done for the skyrmion size experiment, micromagnetic simulations have been performed in order to support the characterization of the skyrmion dynamics with respect to variation in the material properties. In particular, the simulation results show that the skyrmion velocity is increased for a reduction of K_u , while it is increased when M_S is enhanced. As shown in the skyrmion size experiment, also in this case the experimental trend matches the skyrmion velocity trend when a reduction of the saturation magnetization is considered. This supports the idea that, upon FIB irradiation, the degradation rate of the saturation magnetization is higher with respect to the anisotropy one.

Concluding, this work shows how the variation of the material parameters, by means of FIB irradiation, influences both domain and skyrmions static and dynamic properties, both in simulations and experimental work. In particular, in the latter, differences in the amount of current density needed to move such magnetic textures are found. In case of skyrmions the mentioned current density

results to be lower, which is desirable for future applications, leading to lower power consumption. The basics of potential applications have been demonstrated at research level, meaning that industrial resources could improve the domain and skyrmion motion performances, enabling the implementation of a domain or skyrmion-based devices.

Bibliography

- [1] A. Fert C. Chappert and N. Dau. «The emergence of spin electronics in data storage». In: *Nat. Mater* vol 6 (Nov. 2007), pp. 813–823.
- [2] Wang Kang et al. «Magnetic skyrmions for future potential memory and logic applications: Alternative information carriers». In: *2018 Design, Automation & Test in Europe Conference & Exhibition (DATE)*. IEEE. 2018, pp. 119–124.
- [3] S. Blundell. *Magnetism in Condensed Matter*. Oxford Master Series in Condensed Matter Physics. OUP Oxford, 2001. ISBN: 9780198505914. URL: <https://books.google.it/books?id=OGhGmgEACAAJ>.
- [4] A. P. Guimarães. *Principles of Nanomagnetism*. NanoScience and Technology. Springer, Berlin, Heidelberg, 2009. ISBN: 978-3-642-26111-4. URL: <https://link.springer.com/book/10.1007/978-3-642-01482-6>.
- [5] Albert Fert, Vincent Cros, and Joao Sampaio. «Skyrmions on the track». In: *Nature nanotechnology* 8.3 (2013), pp. 152–156.
- [6] A Hrabec et al. «Measuring and tailoring the Dzyaloshinskii-Moriya interaction in perpendicularly magnetized thin films». In: *Physical Review B* 90.2 (2014), p. 020402.
- [7] Wang Kang et al. «Skyrmion-electronics: An overview and outlook». In: *Proceedings of the IEEE* 104.10 (2016), pp. 2040–2061.
- [8] Soon-Wook Jung et al. «Current-induced domain wall motion in a nanowire with perpendicular magnetic anisotropy». In: *Applied Physics Letters* 92.20 (2008), p. 202508.
- [9] GSD Beach, M Tsoi, and JL Erskine. «Current-induced domain wall motion». In: *Journal of magnetism and magnetic materials* 320.7 (2008), pp. 1272–1281.
- [10] Alexandra Mougin et al. «Domain wall mobility, stability and Walker breakdown in magnetic nanowires». In: *EPL (Europhysics Letters)* 78.5 (2007), p. 57007.

- [11] Jairo Sinova et al. «Spin hall effects». In: *Reviews of modern physics* 87.4 (2015), p. 1213.
- [12] Axel Hoffmann. «Spin Hall effects in metals». In: *IEEE transactions on magnetics* 49.10 (2013), pp. 5172–5193.
- [13] Felix Büttner et al. «Field-free deterministic ultrafast creation of magnetic skyrmions by spin–orbit torques». In: *nature nanotechnology* 12.11 (2017), pp. 1040–1044.
- [14] B. Dieny and M. Chshiev. «Perpendicular magnetic anisotropy at transition metal/oxide interfaces and applications». In: *Rev. Mod. Phys.* 89 (2 June 2017), p. 025008. DOI: [10.1103/RevModPhys.89.025008](https://doi.org/10.1103/RevModPhys.89.025008). URL: <https://link.aps.org/doi/10.1103/RevModPhys.89.025008>.
- [15] S. S. P Parkin, M. Hayashi, and L. Thomas. «Domain wall pinning for race-track memory using exchange bias». In: *Science* 320 (2008), pp. 190–194. DOI: [10.1126/science.1145799](https://doi.org/10.1126/science.1145799).
- [16] I. Polenciuc et al. «Domain wall pinning for racetrack memory using exchange bias». In: *Applied Physics Letters* 105.16 (2014), p. 162406. DOI: [10.1063/1.4899134](https://doi.org/10.1063/1.4899134). eprint: <https://doi.org/10.1063/1.4899134>. URL: <https://doi.org/10.1063/1.4899134>.
- [17] F. Riente et al. «Ta/CoFeB/MgO analysis for low power nanomagnetic devices». In: *AIP Advances* 10.12 (2020), p. 125229. DOI: [10.1063/9.0000013](https://doi.org/10.1063/9.0000013). eprint: <https://doi.org/10.1063/9.0000013>. URL: <https://doi.org/10.1063/9.0000013>.
- [18] PJ Metaxas et al. «Creep and flow regimes of magnetic domain-wall motion in ultrathin Pt/Co/Pt films with perpendicular anisotropy». In: *Physical review letters* 99.21 (2007), p. 217208.
- [19] Simon Mendisch et al. «Controlling Domain-Wall Nucleation in Ta/CoFeB/MgO Nanomagnets via Local Ga+ Ion Irradiation». In: *Physical Review Applied* 16.1 (July 2021). ISSN: 2331-7019. DOI: [10.1103/physrevapplied.16.014039](https://doi.org/10.1103/physrevapplied.16.014039). URL: <http://dx.doi.org/10.1103/PhysRevApplied.16.014039>.
- [20] André Thiaville et al. «Dynamics of Dzyaloshinskii domain walls in ultrathin magnetic films». In: *EPL (Europhysics Letters)* 100.5 (2012), p. 57002.
- [21] Markus Laufenberg et al. «Temperature dependence of the spin torque effect in current-induced domain wall motion». In: *Physical review letters* 97.4 (2006), p. 046602.
- [22] L Herrera Diez et al. «Controlling magnetic domain wall motion in the creep regime in He+-irradiated CoFeB/MgO films with perpendicular anisotropy». In: *Applied Physics Letters* 107.3 (2015), p. 032401.

- [23] Sankha S Mukherjee et al. «Crystallization and grain growth behavior of CoFeB and MgO layers in multilayer magnetic tunnel junctions». In: *Journal of Applied Physics* 106.3 (2009), p. 033906.
- [24] T. Devolder et al. «Irradiation-induced tailoring of the magnetism of CoFeB/MgO ultrathin films». In: *Journal of Applied Physics* 113.20 (2013), p. 203912. DOI: [10.1063/1.4808102](https://doi.org/10.1063/1.4808102). eprint: <https://doi.org/10.1063/1.4808102>. URL: <https://doi.org/10.1063/1.4808102>.
- [25] L Herrera Diez et al. «Enhancement of the Dzyaloshinskii-Moriya interaction and domain wall velocity through interface intermixing in Ta/CoFeB/MgO». In: *Physical Review B* 99.5 (2019), p. 054431.
- [26] Yutaro Takeuchi et al. «Spin-orbit torques in high-resistivity-W/CoFeB/MgO». In: *Applied Physics Letters* 112.19 (2018), p. 192408.
- [27] Xichao Zhang et al. «Skyrmion-electronics: writing, deleting, reading and processing magnetic skyrmions toward spintronic applications». In: *Journal of Physics: Condensed Matter* 32.14 (2020), p. 143001.
- [28] Xichao Zhang et al. «Skyrmion-skyrmion and skyrmion-edge repulsions in skyrmion-based racetrack memory». In: *Scientific reports* 5.1 (2015), pp. 1–6.
- [29] Felix Büttner, Ivan Lemesch, and Geoffrey SD Beach. «Theory of isolated magnetic skyrmions: From fundamentals to room temperature applications». In: *Scientific reports* 8.1 (2018), pp. 1–12.
- [30] Xiaoxuan Zhao et al. «Enhancing domain wall velocity through interface intermixing in W-CoFeB-MgO films with perpendicular anisotropy». In: *Applied Physics Letters* 115.12 (2019), p. 122404.
- [31] Masaya Uchida et al. «Real-space observation of helical spin order». In: *Science* 311.5759 (2006), pp. 359–361.
- [32] XS Wang, HY Yuan, and XR Wang. «A theory on skyrmion size». In: *Communications Physics* 1.1 (2018), pp. 1–7.
- [33] Hiu Tung Fook et al. «Mitigation of magnus force in current-induced skyrmion dynamics». In: *IEEE Transactions on Magnetism* 51.11 (2015), pp. 1–4.